

NOTE TO USERS

This reproduction is the best copy available.

UMI[®]



BOSTON UNIVERSITY
COLLEGE OF ENGINEERING

Dissertation

**MECHANICAL AND MATERIAL CHARACTERIZATION
OF BILAYER MICROCANTILEVERS
FOR MEMS-BASED IR DETECTOR APPLICATIONS**

by

I-KUAN LIN

B.S., Da-Yeh University, Taiwan, 2002
M.S., National Cheng Kung University, Taiwan, 2004

Submitted in partial fulfillment of the
requirements for the degree of
Doctor of Philosophy

2011

UMI Number: 3430435

All rights reserved

INFORMATION TO ALL USERS

The quality of this reproduction is dependent upon the quality of the copy submitted.

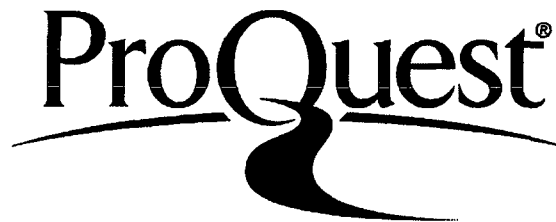
In the unlikely event that the author did not send a complete manuscript and there are missing pages, these will be noted. Also, if material had to be removed, a note will indicate the deletion.



UMI 3430435

Copyright 2010 by ProQuest LLC.

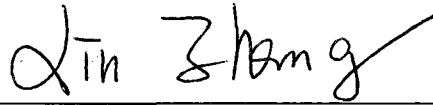
All rights reserved. This edition of the work is protected against unauthorized copying under Title 17, United States Code.



ProQuest LLC
789 East Eisenhower Parkway
P.O. Box 1346
Ann Arbor, MI 48106-1346

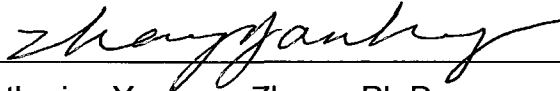
Approved by

First Reader



Xin Zhang, Ph.D.
Associate Professor of Mechanical Engineering

Second Reader



Katherine Yanhang Zhang, Ph.D.
Clare Boothe Luce Assistant Professor of Mechanical
Engineering and Biomedical Engineering

Third Reader



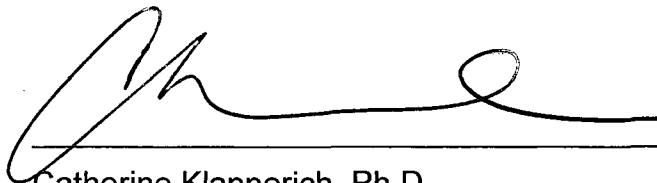
Thomas Bifano, Ph.D.
Professor of Mechanical Engineering
Director, Photonics Center

Fourth Reader



Andre Sharon, Ph.D.
Professor of Mechanical Engineering
Director of Fraunhofer Center for Manufacturing Innovation

Fifth Reader



Catherine Klapperich, Ph.D.
Assistant Professor of Mechanical Engineering and Biomedical
Engineering

ACKNOWLEDGEMENTS

First and foremost, I would like to thank the guidance and support of my advisors, Prof. Xin Zhang and Prof. Katherine Yanhang Zhang. I would note where I am today without the opportunity that they have given me. I am also eternally grateful to other members of my committee for their important roles in my Ph.D. study. Prof. Thomas Bifano, Prof. Andre Sharon, and Prof. Catherine Klapperich have provided me with valuable advice and insightful comments on my research.

Second, all facilities and equipments support are acknowledged. Prof. Bifano, for kindly sharing his entire lab with us; Prof. Sharon, and Fraunhofer CMI, for everything from lab facilities to office support; Prof. Klapperich, for her generous help in nanoindentation. The microfabrication and most of the characterization experiments are conducted at Boston University Photonics Center. I would like to thank the Photonics Center for all the technical support provided throughout the course of my dissertation.

Numerous people have helped me in my experiments and research throughout the years. Special thanks are given to Prof. Kuo-Shen Chen and Dr. Kuang-Shun Ou from National Cheng Kung University, for their contributions to the related topics. You have been my friends, my mentors, my confidants and a never-ending fountain of moral supports. I appreciate the help and friendship of

all my previous and current labmates: Dr. Yan Liu, Dr. Shusen Huang, Dr. Zhiqiang Cao, Dr. Yiling Qiu, Dr. Hu Tao, Xiaoyu Zheng, Ping Du, Kebin Fan, Bradley Kaanta, Xiaoning Wang, Alket Mertiri, Mehmet Ozturk, Else Frohlich, Benjamin Hansen, Axel Gonzalez, Richmond Chow, Wen Xiao, George Fraley and George Seamans. I am equally grateful to many others who have been of assistance in my experiments in various ways, particularly: Anlee Krupp, Paul Mak, Dr. Helen Fawcett, and Dr. Jessica Kaufman.

Last but not least, I'd like to dedicate this thesis to my dad Siou-Mao Lin, my mom Chou-Fong Wang and my brother I-Hung Lin. Mom and dad, I hope I have made you proud. Wen-chen, thanks for everything!

This project has been supported in part by the Young Faculty Award from DARPA/MTO to Prof. Y. Zhang (W911NF-07-1-0181), the National Science Foundation through grant CMMI 0700688 and the Air Force Office of Scientific Research through grant FA 9550-06-1-0145 to Prof. X. Zhang. The funding agency is gratefully acknowledged.

**MECHANICAL AND MATERIAL CHARACTERIZATION
OF BILAYER MICROCANTILEVERS
FOR MEMS-BASED IR DETECTOR APPLICATIONS**

(Order No.)

I-KUAN LIN

Boston University, College of Engineering, 2011

Major Professors: Xin Zhang, Ph.D., Associate Professor of Mechanical Engineering; Katherine Yanhang Zhang, Ph.D., Clare Boothe Luce Assistant Professor of Mechanical Engineering and Biomedical Engineering

ABSTRACT

Uncooled micro-electro-mechanical systems (MEMS)-based infrared radiation (IR) detectors have received extensive attention for wide use in military and civilian applications such as for night vision, environmental monitoring, biomedical diagnostics, remote sensing, and thermal probing of active microelectronic devices. These detectors utilize the bending of bilayer microcantilevers upon absorption of IR to form thermal images. While these MEMS-based IR detectors have many benefits over photon detectors, the residual stress-induced curvature after fabrication and inelastic deformation greatly compromise their performance. Recently, a composite material, silicon oxynitride (SiON), which has a unique tunability in IR absorption spectrum, has been proposed to replace the conventional IR absorption material such as silicon nitride (Si_3N_4) in IR detectors. This composite material enhances the sensitivity to selective targets, which emit IR at particular wavelength. However, the

mechanical properties of the composite material have seldom been studied. Accurate mechanical and material characterization is crucial to ensure performance and reliability.

This dissertation addresses three important fundamental technical issues for the next-generation of high-sensitivity and tunable MEMS-based IR detectors: 1) planarization; 2) long-term behavior prediction of $\text{Si}_3\text{N}_4/\text{Al}$ bilayer microcantilevers; and 3) mechanical and material properties characterization of silicon oxynitride thin films. This research provides a comprehensive mechanical and material characterization of the temperature- and time-dependent thermomechanical responses of the $\text{Si}_3\text{N}_4/\text{Al}$ bilayer microcantilever beams under different thermal loading. Experimental methodologies, theoretical models and finite element analysis (FEA) models are developed to achieve flattened bilayer microcantilevers, and to predict the temperature- and time-dependent deformation of MEMS-based IR detectors in short- and long-term operation. In addition, the mechanical and material properties of the silicon oxynitride thin films are systematically studied using nanoindentation for mechanical characterization, energy dispersive X-ray analysis (EDX) for material composition, and Fourier transform infrared spectrometry (FT-IR) for optical characterization.

The experimental methodologies and theoretical framework developed in this research can be readily applied to study the thermomechanical behavior of

various bilayer microcantilever structures, and to improve the fundamental understanding required to design high-sensitivity and tunable MEMS-based IR detectors.

TABLE OF CONTENTS

ACKNOWLEDGEMENTS	iii
ABSTRACT	v
CONTENTS	viii
LIST OF TABLES	xiii
LIST OF FIGURES	xiv
CHAPTER 1: INTRODUCTION	1
1.1 Introduction	1
1.2 Motivation and Significance	6
<i>1.2.1 Bilayer Microcantilevers: A Thermomechanical Perspective</i>	6
<i>1.2.2 Composite Thin Film Materials: A Mechanical Perspective</i>	9
<i>1.2.3 Example of Application: Tunable MEMS-based IR Detectors</i>	11
1.3 Statement of Scopes	12
1.4 Dissertation Outline	13
CHAPTER 2: EXPERIMENTAL METHODS	21
2.1 Fabrication Process of Bilayer Microcantilevers	21
<i>2.1.1 Substrate Preparation</i>	21
<i>2.1.2 Sacrificial Layer</i>	22
<i>2.1.3 Structure Layer Deposition and Patterning</i>	24
<i>2.1.4 Cantilever Release</i>	25
2.2 Fabrication Process of Silicon Oxynitride Films	25

2.3 Thermomechanical Characterization	26
2.3.1 <i>Interferometer</i>	27
2.3.2 <i>Heating/colling Stage</i>	27
2.3.3 <i>Data Analysis</i>	27
2.4 Material and Mechanical Characterization	28
2.4.1 <i>Energy Dispersive X-ray Analysis (EDX)</i>	28
2.4.2 <i>Fourier Transform Infrared Spectrometry (FT-IR)</i>	29
2.4.3 <i>Nanoindentation</i>	30
 CHAPTER 3: TEMPERATURE-DEPENDENT DEFORMATION OF BILAYER	
 MICROCANTILEVER BEAMS	
	45
3.1 Introduction	45
3.2 Theoretical Background	46
3.2.1 <i>Thermal Induced Bending Model</i>	46
3.2.2 <i>Residual Stress Induced Bending Model</i>	50
3.3 Experimental Procedure	53
3.4 Results	54
3.5 Discussion	56
3.5.1 <i>Thermal Elasticity</i>	56
3.5.2 <i>Thermal Inelasticity</i>	57
3.5.3 <i>Intrinsic Stress Development</i>	58
3.5.4 <i>Curvature Control</i>	61
3.6 Conclusions	62

CHAPTER 4: TIME-DEPENDENT DEFORMATION OF BILAYER

MICROCANTILEVER BEAMS	74
4.1 Introduction	74
4.2 Theoretical Background	76
4.3 Thermo-mechanical Characterization	77
4.3.1 <i>Pre-cycling</i>	78
4.3.2 <i>Isothermal Holding</i>	78
4.4 FEA Model Development	80
4.5 Discussion	83
4.5.1 <i>Creep Behavior</i>	83
4.5.2 <i>Stress Evolution</i>	84
4.6 Conclusions	85

CHAPTER 5: THERMOMECHANICAL BEHAVIOR OF MEMS-BASED IR

DETECTORS	99
5.1 Introduction	99
5.2 Experimental Procedure	102
5.2.1 <i>Thermal Cycling</i>	102
5.2.2 <i>Isothermal Holding</i>	102
5.3 Finite Element Model	103
5.4 Results and Discussion	104
5.4.1 <i>Planarization</i>	104
5.4.2 <i>Thermo-mechanical Response</i>	107

5.4.3 <i>Parameter Study on the Thermo-mechanical Response</i>	108
5.4.4 <i>Inelastic Deformation in Long-term Operation</i>	110
5.5 Conclusions	112
CHAPTER 6: INELASTIC DEFORMATION OF BILAYER MICROCANTILEVER	
BEAMS WITH NANOSCALE COATING	124
6.1 Introduction	124
6.2 Specimens Preparation	126
6.3 Finite Element Model	127
6.4 Results and Discussion	129
6.4.1 <i>Thermal Cycling</i>	129
6.4.2 <i>Isothermal Holding</i>	130
6.4.3 <i>Finite Element Analysis</i>	132
6.4.4 <i>Microstructural Evolution</i>	134
6.5 Conclusions	137
CHAPTER 7: COMPOSITE MATERIAL FOR IR ABSORBER	152
7.1 Introduction	152
7.2 Theoretical Background	156
7.2.1 <i>Oliver-Pharr Method</i>	156
7.2.2 <i>Nanoindentation Creep</i>	157
7.3 Experimental Procedure	159
7.3.1 <i>Constant Rate of Loading (CRL)</i>	160
7.3.2 <i>Indentation Load Relaxation (ILR)</i>	160

7.4 Results and Discussion	161
7.4.1 <i>Material and Optical Properties of SiON Films</i>	161
7.4.2 <i>Young's Modulus and Indentation-hardness of SiON Films</i>	164
7.4.3 <i>Nanoindentation Creep Analysis of SiON Films</i>	166
7.4.4 <i>Shear Transformation Zone (STZ) Theory</i>	167
 CHAPTER 8: CONCLUSIONS AND RECOMMENDATIONS FOR FUTURE	
 WORK	185
8.1 Summary	185
8.2 Contributions	188
8.3 Recommendations for future work	189
 APPENDIX	191
 BIBLIOGRAPHY	198
 VITA	210

LIST OF TABLES

Table 1.1: MEMS vs. Microelectronic applications: differences in behavior	16
Table 2.1: PECVD deposition parameters of SiO ₂ and Si ₃ N ₄ films	31
Table 2.2: RIE etching recipes of SiO ₂ , Si ₃ N ₄ and polyimide films	32
Table 2.3: Sputtering deposition recipes of Silicon oxynitride films.....	33
Table 2.4: Technical specification of HCP 302.....	34
Table 3.1: Material parameters used in the finite element model.....	64
Table 4.1: Material constants, <i>A</i> and <i>n</i> , of Power-law creep at different holding temperatures	87
Table 5.1: Dimension input data of FEM model for MEMS-base IR detectors .	113
Table 6.1: Surface roughness of uncoated microcantilever beams after isothermal holding at various temperatures	139
Table 7.1: Sputtering RF power applied in SiON film deposition, and corresponding atomic concentration of Si, O and N in film composition	172
Table 7.2: Young's modulus and indentation-hardness of the SiON films	173

LIST OF FIGURES

Fig.1.1:	A scanning electron microscope (SEM) image of MEMS-based IR focal plan array (FPAs) (Jones <i>et al.</i> , 2009).....	17
Fig.1.2:	Organizational chart for the proposed research effort.	18
Fig.1.3:	(a) A portion of a 5×5 IR FPAs of pixels (Amantea <i>et al.</i> , 1998) and (b) double-cantilever IR FPAs (Huang <i>et al.</i> , 2008) have undesired initial bending due to the imbalanced residual stresses in the bimaterial cantilever structures.....	19
Fig.1.4:	(a) The schematic view of the bending of a pixel of MEMS-based IR FPAs during sensing operation and (b) read-out circuit diagram at each pixel (Hunter <i>et al.</i> , 2006).	20
Fig.2.1:	The general fabrication process of bilayer microcantilevers.	35
Fig.2.2:	Fabrication process of polyimide sacrificial layer.....	36
Fig.2.3:	The thickness of polyimide sacrificial layer before and after curing	37
Fig.2.4:	SEM images of (a) bilayer microcantilever beams and (b) MEMS-based IR detectors.	38
Fig.2.5:	(a) a schematic view and (b) image of setup for <i>in situ</i> deformation measurement of microcantilevers during thermal loading.....	39
Fig.2.6:	The schematic view of setup of Interferometer.....	40
Fig.2.7:	Microheating stage (HCP302) from INSTEC Inc in the experiment setup.....	41

Fig.2.8: (a) Image from the WYKO interferometric microscope showing the topology of the top surface of the microcantilever beams and (b) surface profiles of the bilayer beam at different temperatures along the arrow line in (a)..... 42

Fig.2.9: (a) Image from the WYKO interferometric microscope showing the topology of the top surface of the MEMS-based IR detectors and (b) surface profiles of detectors at different temperatures along the arrow line in (a)..... 43

Fig.2.10: (a) Hysitron TriboIndenter™ nanoindentation system and (b) a typical load-displacement curve..... 44

Fig.3.1: Multilayer structure, where h_i is the thickness of i th layer, $z_i = \sum_{j=1}^{i-1} h_j$ is the bottom position of i th layer ($Z_1=0$ is the first layer)..... 65

Fig.3.2: The reference plane is chosen at $z=0$. The neutral plane is defined as the plane where the bending strain ε_b is zero. 66

Fig.3.3: Schematic illustrating the general curvature versus temperature response of a $\text{Si}_3\text{N}_4/\text{Al}$ bilayer microcantilever beam in a thermal cycle 67

Fig.3.4: Curvature versus temperature for bilayer Si_3N_4 (200 nm)/Al (200 nm) microcantilever beams during the five thermal cycles with different peak temperatures. The diamond and circle symbols are measured

	curvatures during the heating and cooling processes in each cycle, respectively.....	68
Fig.3.5:	Residual stress evolution of Al film after various annealing temperature	69
Fig.3.6:	SEM & AFM image of Al grains (a) before and (b) after 225 °C annealing.....	70
Fig.3.7:	Residual stress evolution of Si ₃ N ₄ film after various annealing temperatures.	71
Fig.3.8:	Measured room temperature curvature after each thermal cycle from Fig. 3.5. The peak temperatures of the 1 st , 2 nd , 3 rd , 4 th , and 5 th cycle are 150 °C, 175 °C, 200 °C, 225 °C, and 250 °C, respectively.....	72
Fig.3.9:	Uniform residual strain mismatch after each thermal cycle from Fig. 3.9. The peak temperatures of the 1 st , 2 nd , 3 rd , 4 th , and 5 th cycle are 150 °C, 175 °C, 200 °C, 225 °C, and 250 °C, respectively	73
Fig.4.1:	Overall research structure and process of Chapter 4.....	88
Fig.4.2:	Schematic of thermal loading profile within the heating/cooling stage for thermomechanical characterization.	89
Fig.4.3:	Curvature evolution during the heating, isothermal holding and subsequent cooling to room temperature.	90
Fig.4.4:	Measured curvature evolution during the 45 hour isothermal holding periods at temperatures of 100 °C, 125 °C and 150°C for Si ₃ N ₄ /Al	

	bilayer microcantilever beams. The symbols represent experimental data, while the solid lines represent simulation results.	91
Fig.4.5:	Normalized curvature evolution during the 45 hour isothermal holding at temperature of 100 °C, 125 °C and 150°C for Si ₃ N ₄ /Al bilayer microcantilever beams. The symbols represent experimental data while the solid lines represent simulation results.	92
Fig.4.6:	The bilayer microcantilever beam is meshed by S4R elements. The finite element model constitutes 1800 elements.	93
Fig.4.7:	Convergence study of thermomechanical behavior simulation.....	94
Fig.4.8:	Creep data reduction. Material constant (A) of Power-law creep as a function of 1/T, where T is the test temperature.	95
Fig.4.9:	The comparison between the additional experimental data and the Power-law creep prediction	96
Fig.4.10:	Stress distributions in both the Al and the Si ₃ N ₄ layers of bilayer microcantilever beams at time of 0, 5, 10, 25, and 45 hours of isothermal holding at temperature of (a) 100 °C, (b) 125 °C and (c) 150 °C.....	98
Fig.5.1:	An SEM image of a MEMS-based IR detector on bottom electrodes of Pt/Ti. Both the Si ₃ N ₄ layer and the Al layer have a thickness of 200 nm.....	114
Fig.5.2:	Finite element mesh of a MEMS-based IR detector which is formed with two actuation legs and a sensing plate.....	115

Fig.5.3:	Convergence study of thermomechanical behavior simulation for MEMS-based IR detectors.....	116
Fig.5.4:	Curvature vs. temperature during the four thermal cycles with different peak temperatures. (Temp. increase: blue symbols; Temp. decrease: pink symbols).....	117
Fig.5.5:	SEM image of as-released MEMS-based IR detectors which have residual strain mismatch induced curvature.....	118
Fig.5.6:	SEM image of flattened IR detectors after thermal cycling with a peak temperature of 295 °C.	119
Fig.5.7:	Measured room temperature (RT) curvature and calculated residual strain mismatch after each thermal cycle from Fig. 5.4.....	120
Fig.5.8:	Correction factor and the percentage curvature difference varies as the parameters such as (a) Young's modulus ratio (m), (b) thickness ratio (h) and (c) mismatch of CTE ($\Delta\alpha$) changes.	122
Fig.5.9:	Experimental and simulation result of isothermal holding test on MEMS-based IR detectors.....	123
Fig.6.1:	Fabrication process of the Au/ Si ₃ N ₄ bilayer microcantilever beams with nanocoating: (a) deposition of 1.5 μm thick SiO ₂ and etching of SiO ₂ by RIE with SF ₆ , (b) deposition of a 1.15 μm thick PECVD Si ₃ N ₄ layer and a 0.5 μm thick e-beam evaporated Au layer, and patterning of Au and Si ₃ N ₄ layers using KI and RIE with SF ₆ and He, respectively, (c) releasing of the microcantilever beams by isotropic etching of SiO ₂ with	

	BOE and then drying by supercritical CO ₂ release system, (d) nanocoating of alumina by ALD.....	140
Fig.6.2:	SEM image of an array of Au (0.5 μm thick)/ Si ₃ N ₄ (1.15 μm thick) microcantilever beams suspended over a silicon substrate.....	141
Fig.6.3:	Curvature of (a) Au/ Si ₃ N ₄ microcantilever beams and (b) ALD alumina coated microcantilever beams as a function of temperature during four thermal cycles with peak temperatures of 125 °C, 150 °C, 175 °C, and 200 °C. The triangle and circle symbols are measured curvatures during the heating and cooling process in each cycle, respectively..	143
Fig.6.4:	Curvature evolution during the 60 hours isothermal holding at 100 °C, 150 °C and 200°C for Au/ Si ₃ N ₄ microcantilever beams. The symbols represent experimental data while the solid lines represent simulation results.	144
Fig.6.5:	Curvature evolution during the 60 hours isothermal holding at 150 °C for 5nm, 10 nm, 20nm and 40 nm ALD alumina coated microcantilever beams. The symbols represent experimental data while the solid lines represent simulation results.....	145
Fig.6.6:	The stress distribution in both Au and Si ₃ N ₄ layers of microcantilever beams for 0, 10, 20, 40 and 60 hour duration in isothermal holding at (a) 100 °C (b) 150 °C and (c) 200 °C.	147

Fig.6.7:	The stress distribution in 10 nm ALD alumina, Au and Si ₃ N ₄ layers of ALD coated microcantilever beams for 0, 10, 20, 40 and 60 hour duration in isothermal holding at 150 °C	148
Fig.6.8:	SEM images of surface profiles on microcantilever beams (a) before and after 60 hours isothermal holding at (b) 100 °C, (c) 150 °C and (d) 200°C.....	149
Fig.6.9:	SEM images of surface profile on (a) 5 nm, (b) 10 nm, (c) 20 nm and (d) 40 nm ALD alumina coated microcantilever beams after 60 hours of isothermal holding at 150 °C.....	150
Fig.6.10:	The tensile stress decrease in Au layer after 150 °C isothermal holding in microcantilever beams with different ALD alumina thicknesses...	151
Fig.7.1:	Load scheme of the constant rate of loading (CRL) experiment for the SiON films.....	174
Fig.7.2:	Load scheme of the indentation load relaxation (ILR) experiment for the SiON films.....	175
Fig.7.3:	EDX spectra of the SiON films.....	176
Fig.7.4:	MIR FT-IR absorbance spectra of the SiON films.....	177
Fig.7.5:	Load –displacement (P-h) curves of the SiON films in the constant rate of loading nanoindentation experiments.	178
Fig.7.6:	Young’s modulus and indentation-hardness of the SiON films as a function of the nitrogen content (N/(O+N)).....	179

Fig.7.7: Load–displacement (P-h) curves of nanoindentation creep on the SiON films 180

Fig.7.8: Creep displacement h_c ($h-h_0$) versus creep time t_c ($t-t_0$) curves (solid scatters) with corresponding fittings (solid lines) of nanoindentation creep on the SiON films..... 181

Fig.7.9: Logarithm relations of strain rate and applied stress in nanoindentation creep for the SiON films: (a) SiO_x ; (b) SiO_xNy_1 ; (c) SiO_xNy_2 ; (d) SiO_xNy_3 and (e) $SiNy$ 184

CHAPTER 1: INTRODUCTION

1.1. Introduction

The twentieth century has been witness to the development of infrared radiation (IR) detectors and cameras as complex multi-color cameras with amazing features. Development has further pushed the technology into small, lightweight, incredibly portable and user-friendly uncooled IR cameras. Over the past few decades, IR cameras have been used for a wide range of both commercial and military applications based on the ability to detect the thermal radiation emitted by warm objects, both animate and inanimate, irrespective of the lighting conditions.

The first infrared detection system is a photon detector that is first developed in the early 1950s. This IR detector is composed of materials with small energy band gaps, which are excited by infrared radiation of 8 μm to 12 μm . However, the small band gap makes this type of detector highly sensitive to thermal noise. In order to reduce the thermal noise to acceptable levels, a cryogenic pump is required to cool the detector to approximately 80 K. The addition of the pump makes such devices bulky and expensive (Rogalski, 2003; Dereniak and Boreman, 1996; Kruse and Skatrud, 1997). These circumstances have driven research towards uncooled IR detectors, which rely on photothermal heating generated from IR absorption.

Throughout the past twenty years, various uncooled IR detectors have been proposed and studied. Two types of uncooled IR detectors especially have been proven especially useful for uncooled thermal imaging arrays. The first type consists of ferroelectric-pyroelectric arrays, which record a spontaneous electric polarization change with temperature. The second type uses a resistive bolometric array, whose electrical resistance changes with temperature. These two detectors can provide imaging scenes at room temperature and currently dominate the rapidly growing market of uncooled IR cameras (Dereniak and Boreman, 1996; Kruse and Skatrud, 1997; Rogalski, 2003).

Uncooled infrared radiation (IR) detectors have received considerable attention for wide use in military and civilian applications, ranging from night vision, environmental monitoring, security surveillance biomedical diagnostics, remote sensing and thermal probing of active microelectronic devices. With the development of microelectromechanical system (MEMS) technology, uncooled MEMS-based IR detectors (Fig 1.1) have been the focus of attention. These detectors generally consist of silicon nitride (Si_3N_4) and aluminum (Al) bimaterial cantilevers. The Si_3N_4 layer absorbs infrared energy, resulting in a curvature in the structure that can be measured by using piezoresistive, optical, or capacitive methods. This detector can achieve a theoretical noise-equivalent temperature difference (NETD) of below 5 mk (Amantea *et al.*, 1998; Amantea *et al.*, 1997; Li,

2004; Zhao *et al.*, 2002).

Recently, a composite material (SiON), which has unique tunability in IR absorption spectrum (Lin *et al.*, 2010; Modreanu *et al.*, 1999; Yan *et al.*, 2008), has been proposed to replace the conventional IR absorption material (Si_3N_4) in IR detectors. This new material would allow for an enhancement in the sensitivity to the selective targets, which emit specific IR radiation. The use of the composite material in the bilayer microcantilevers would make it possible to develop chip-based, low-cost, low-NETD, and high-sensitivity MEMS-based IR detectors. *However, many deleterious effects in the MEMS-based detectors are related to the mechanical properties of the materials.* One of these effects is that the released detectors always bend up (or down) due to the imbalance in residual stresses in the multilayer MEMS thin films (Fig. 1.2) (Huang *et al.*, 2008; Huang *et al.*, 2006; Huang and Zhang, 2006; Lin *et al.*, 2008b). The undesirable initial curvatures of the microcantilevers render arrays of the structures and devices useless. In addition, important factor to address is the reliability issue. It is important to understand the deformation of microcantilevers that occurs over a significant period of time, in order to meet performance and reliability requirements. This is especially important for structures subjected to thermal loading and/or operated at elevated temperatures (Gall *et al.*, 2004; Zhang and Dunn, 2004; Zhang *et al.*, 2004). Another issue is that the mechanical properties of this composite material (SiON) have not been reported in literature.

Neglecting these inherent mechanical properties and behaviors can result in design mistakes and misinterpretations of the sensing data and can compromise the performance of the IR detectors. *Hence, it is of vital importance to perform accurate mechanical characterizations on bilayer microcantilevers and the composite material for the development of planar, reliable and high sensitivity MEMS-based IR detectors.*

This dissertation addresses three critical technical issues for next-generation high-sensitivity and tunable MEMS-based IR detectors: 1) Planarization, 2) Long-term behavior prediction of $\text{Si}_3\text{N}_4/\text{Al}$ bilayer microcantilevers and 3) Mechanical and material properties characterization of silicon oxynitride thin films. A basic flow chart of the proposed plan of research is shown in Fig. 1.3. The research effort includes mechanical characterization of the bilayer microcantilever beams ($\text{Si}_3\text{N}_4/\text{Al}$ in this dissertation), which is probed at temperature and time domains using an interferometer with heating/cooling stages. A finite element analysis (FEA) model is developed, using the data obtained from a set of isothermal holding tests. The validated FEA model is ultimately utilized to determine the temperature- and time-dependent deformation of MEMS-based IR detectors. Furthermore, the mechanical and optical properties of the composite material (SiON) are systemically studied by using an indentation technique and Fourier transform infrared radiation (FT-IR) spectroscopy, respectively. The proposed research effort entails a balance

between the experimental characterization of the mechanical behavior and the development of a theoretical or numerical model of MEMS-based IR detectors application. To this end, this dissertation has the following objectives:

- 1) Understand the thermomechanical evolution during cyclic thermal loading.** The general behavior of the bilayer microcantilever beams when subjected to cyclic thermal loading is characterized with both linear thermoelastic and inelastic regions during cyclic thermal loading.
- 2) Understand and characterize the creep and stress relaxation behaviors in bilayer microcantilever beams.** Time-dependent deformation and creep parameters during isothermal holding at various temperatures are fully characterized by Power-law model.
- 3) Develop the finite element analysis (FEA) model to simulate and predict the thermomechanical behavior of bilayer microcantilevers.** The temperature- and time-dependent deformations are analyzed using the finite element method (FEM) with characterized material properties from topic 1 and topic 2.
- 4) Improve the planarity and reliability of MEMS-based IR detectors.** The thermal cycling technique developed in topic 1 and the FEA

model developed in topic 3 are employed to flatten IR detectors and simulate the deformation during long-term operation, respectively.

5) Understand the isothermal creep and stress relaxation behaviors in multilayer microcantilevers with nano-coatings.

Inelastic deformation during isothermal holding at various temperatures will be fully characterized via an *in-situ* full field deformation measurement. The effects of nano-coatings on the thermomechanical responses will be investigated.

6) Systematically study the mechanical behaviors, including time-dependent/independent plasticity of composite thin film materials, for the IR absorber using indentation testing.

Particularly the SiON films that are tunable in the IR absorption spectrum, and thus have potential applications in IR detectors, are tested.

1.2. Motivation and Significance

1.2.1 Bilayer Microcantilevers: A Thermomechanical Perspective

The physical movement of bilayer microcantilevers is widely employed in microelectromechanical systems (MEMS) for a variety of sensor and actuator applications. The bilayer microcantilever sensors, including infrared (IR) detectors (Wang *et al.*, 2007), thermal detectors (Datskos *et al.*, 2005) and calorimetric high frequency detectors (Lee *et al.*, 2007), rely on the thermal

expansion mismatch-induced deformation upon energy absorption. Subsequently, the deformation can be readily determined by means of piezoresistive, optical or capacitive methods (Amantea *et al.*, 1998; Gao *et al.*, 2009; Grbovic *et al.*, 2006). Also, the movement of the bilayer microcantilever-based actuators can be controlled by applying a temperature change. Such actuators are commonly used in direct current (DC) electrical relays and contacts (Miller *et al.*, 2001), radio frequency (RF) switches (Chang and Chang, 2000), and tunable split ring resonators (SRR) (Tao *et al.*, 2009).

The bilayer microcantilever-based sensors and actuators must exhibit large deformation in order to meet sensitivity and movement requirements, as well as maintaining MEMS and integrated circuit (IC) process compatibility. More specifically, these bilayer microcantilevers must: 1) have a larger thermal expansion mismatch between two layers; 2) be able to operate in wide temperature ranges; and 3) have good MEMS and IC process compatibility, so that the bilayer microcantilever-based sensors and actuators have commercial potential. To satisfy these requirements, one layer is typically made of metal (Au, Ni, Al ... etc.); the other layer is made of ceramic (Si_3N_4 , SiO_2 , poly Si ...etc.), which has a much lower thermal expansion coefficient than metal (Shackelford and Alexander 2001).

There are two critical problems that can greatly compromise the performance

and functionality of the bilayer microcantilevers-based devices. First, the as-fabricated microcantilevers curve because of the imbalanced residual stresses, which develop during fabrication for various reasons, such as the presence of impurities or voids, grain growth, etc. (Doerner and Nix, 1988). Therefore, residual stress measurement (Lu, 1996; Chen *et al.*, 2004) and curvature modification (Lin *et al.*, 2008a; Bifano *et al.*, 2002; Huang *et al.*, 2006) are important topics in the post-process assessment of microcantilever-based devices. Second, from the design viewpoint, the ideal bilayer microcantilevers deform linearly at a rate proportional to temperature change and do not exhibit inelastic deformation over the operation period. However, the metal layers are typically not stable after deposition (Dunn *et al.*, 2001, 2002; Zhang and Dunn, 2003, 2009). When the metals are subjected to thermal loading, especially thermal cycling and isothermal holding, the microstructural evolution, such as extinction of excess vacancies, subgrain coalescence and grain boundary diffusion, in the metal layers can be triggered. The microstructural evolution results in inelastic strain behavior in metal layers and, thus, highly inelastic deformation in bilayer microcantilevers. Neglecting the inelastic deformation can result in misinterpretations of the measurement data from bilayer microcantilever-based sensors and can compromise control precision of actuators. Therefore, it is of vital importance to perform accurate thermomechanical behavioral characterization on bilayer microcantilevers and to develop an appropriate model to represent their temperature- and time-dependent deformation.

Numerous studies have illustrated the basic thermomechanical response of layered beams when subjected to temperature changes or other sources of misfit strains between the layers (Sehr *et al.*, 2001; Go *et al.*, 1996). These misfit strains have come in the context of many technological applications, the most common being structural composite materials and thin film and thick substrate systems for microelectronics applications (Finot and Suresh, 1996; Freund, 1993). In thin film-thick substrate systems, one layer (the thin film) is much smaller than the other (the thick substrate). If subjected to a 100 °C temperature change, the maximum deflection would be about two percent of the thickness of the system. However, in MEMS applications, the layer thicknesses are not only small relative to in-plane dimensions, but they are also often comparable to each other. If subjected to a 100 °C temperature change, the maximum deflection would be about six times the thickness. While much of the understanding regarding the thermomechanical behavior of layered systems derives from experience in microelectronics, significant differences exist for many MEMS applications (Table 1.1). These differences must be well understood to optimize the design of reliable MEMS.

1.2.2. Composite Thin Film Materials: A Mechanical Perspective

Over the past decade, increasing attention has been paid to silicon oxynitride (SiON) as a promising material system for the development of optical, photonic and microelectronic applications. These application include waveguide devices

(Fadel *et al.*, 2009), anti-reflection coatings (Serenyi *et al.*, 2001), nonvolatile semiconductor memories (NVSMs) (Jung *et al.*, 2008), gate dielectrics (Desbiens *et al.*, 2002) , and low power gas sensors (Astie *et al.*, 2000). SiON has been distinguished because its optical and electronic properties can be readily manipulated by altering the chemical composition ratio of oxygen and nitrogen (Gunning *et al.*, 1989; Modreanu *et al.*, 2002). This unique tunability allows for high flexibility and optimization in design and can also benefit the MEMS community. One of the potential applications of SiON films is MEMS-based IR detectors. The wavelength of strongest absorbance peak of Si_3N_4 in the IR spectrum is at 12 μm , which means that Si_3N_4 can easily detect the targets that emit the blackbody radiation with a peak at this wavelength.

In this dissertation, SiON is proposed to replace Si_3N_4 as a leading candidate of IR absorber in MEMS-based IR detectors. The wavelength of absorbance peaks of SiON can be tuned to match the blackbody radiation peaks of targets, in order to improve the sensitivity of IR detectors. In addition, SiON provides not only the tunability in wavelength of absorbance peak, but also a large degree of freedom for the design of a mechanical cantilever system. Although extensive research has been undertaken to sputter SiON films for microelectronic and optical applications, the mechanical properties of SiON films have seldom been reported. This research project aims to study and document these mechanical and material properties, so that SiON may be used in future applications.

1.2.3. Example of Application: Tunable MEMS-based IR Detectors

The importance of successful development of MEMS is clear to the community, which recognizes the need for leading researchers in the field to identify promising new materials and structures for MEMS and to master and characterize technologies that will qualify these materials and structures for robust and reliable system applications. This study is initially motivated by applications in high-sensitivity and tunable MEMS-based IR detector. These detectors utilize the bending of bilayer microcantilevers upon absorption of infrared radiation by the absorber (SiON), as shown in Fig. 1.4(a). When the sensing bimaterial plate transfers IR to heat, the plate deforms because of the mismatch of the coefficients of thermal expansion (CTE) of the SiON and Al layers. Subsequently, the deformation can be readily determined by using piezoresistive, optical or capacitive methods (Fig. 1.4(b)) (Huang *et al.*, 2008; Hunter *et al.*, 2006; Li *et al.*, 2006; Lin *et al.*, 2008b; Zhao *et al.*, 2002). To obtain the necessary thermal expansion mismatch in bilayer actuators, one film layer is typically a metal, and the other is a material with a much lower thermal expansion coefficient, such as a glass or ceramic. An inherent characteristic of such bilayer material structures is that misfit strains lead to stresses in the layers and deformation of the structures. However, the MEMS-based IR detector has residual stress-induced curvature after release and exhibits inelastic deformation over a significant period of time. The deformation can compromise the performance and reliability of the detectors. Moreover, the mechanical properties

of the composite material (SiO_xN_y) have seldom been studied. Consequently, it is important to perform accurate mechanical characterization on bilayer microcantilevers and the composite material for the development of planar, reliable and high-sensitivity MEMS-based IR detectors.

1.3. Statement of Scopes

The overall objective of this work is to contribute to the scientific understanding of micro- and nano-mechanics of MEMS/NEMS thin film material systems, in order to develop a revolutionary approach to the design and fabrication of robust bilayer microcantilever structures and systems for next-generation sensing and imaging applications. The outcome of this thesis will provide a comprehensive characterization of the mechanical responses of the bimaterial microcantilevers under different thermal loading conditions, in both temperature- and time-dependent domains. In addition, both theoretical models and experimental methodologies are presented. From an engineering mechanics viewpoint, through working on this research, a fundamental understanding on the deformation mechanisms of a multilayer, thin film material system is achieved. These behaviors can then be related to the design and analysis of MEMS, and the principles may be applied to improve the performance of the devices in the sub-micron scale. The interpretations in this dissertation will also provide valuable insights to the understanding of similar responses of other ceramic/metal bilayer microcantilevers (such as Au/ Si_3N_4 , SiON/Al, etc.)

commonly used in the microelectronics and MEMS industries. The experimental methods developed in this research can also be readily applied to a wide variety of microcantilevers for various applications.

1.4. Dissertation Outline

This chapter briefly summarizes the motivation and objectives of the dissertation. The subjects of study, background and significance, as well as examples of applications, are introduced. Major contributions of each of the following chapters are outlined below.

Chapter 2 details the specimen fabrication process of the bilayer microcantilevers ($\text{Si}_3\text{N}_4/\text{Al}$) beams, MEMS-based IR detectors, and composite materials (SiON). The bilayer microcantilever beams and MEMS-based IR detectors are constructed using a surface micromachining technique. Subsequently, the interferometer microscope and a heating/cooling stage are set up to *in situ* measure the thermomechanical response of bilayer microcantilevers. The SiON thin films are fabricated by using sputter and then the mechanical and material properties of SiON thin films are characterized by using Energy dispersive X-ray analysis (EDX), Fourier transform infrared spectrometry (FT-IR), and nanoindenter.

Chapter 3 is devoted to the temperature-dependent characterization of the bilayer microcantilevers using a thermal cycling test. The general behavior of the bilayer microcantilever beams when subjected to cyclic thermal loading is characterized with both linear thermoelastic and inelastic regions during cyclic thermal loading. The experimental results are interpreted by using analytical models. The results presented by this chapter are useful for the planarization in MEMS-based IR detectors in Chapter 5.

Chapter 4 is devoted to the time-dependent thermomechanical characterization of bilayer microcantilevers using isothermal holding tests. A set of isothermal holding test is performed to fit the Power-law creep model, by obtaining the corresponding creep parameters. The validated viscoelastic finite element analysis (FEA) model is applied to analyze the thermomechanical behavior of MEMS-based IR detector and is compared to experimental results in Chapter 5.

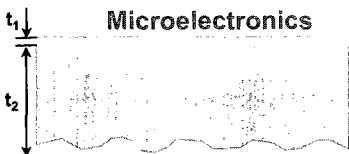

Chapter 5 employs 1) the thermal cycling technique to flatten MEMS-based IR detectors and 2) FEM with Power-law creep to predict the thermomechanical behavior of the bilayer microcantilevers over a significant period of operation time, in order to meet expected performance and reliability requirements.

Chapter 6 demonstrates that the time-dependent inelastic deformation can be suppressed by the use of nano-coatings realized by atomic layer deposition (ALD). The thermomechanical behavior of alumina-coated/uncoated bilayer microcantilevers was characterized by using thermal cycling and isothermal holding tests.

Chapter 7 investigates the material, optical and mechanical properties of the composite material (SiON) by using various techniques, to achieve a fundamental understanding required to design MEMS-based IR detectors. Time-dependent plastic deformation (creep) of SiON films are investigated by depth-sensing nanoindentation at room temperature. Young's modulus and indentation hardness are found to correlate with the nitrogen/oxygen ratio in SiON thin films.

Finally, Chapter 8 concludes the thesis by summarizing the major contributions of the thesis and pointing out potential future research directions.

Table 1.1: MEMS vs. Microelectronic applications: differences in behavior.

Applications	Microelectronics	MEMS
Aspects		
Film thickness	$t_1 \ll t_2$ $t_1 = 0.5 \mu\text{m}, t_2 = 500 \mu\text{m}$	comparable $t_1 = 0.5 \mu\text{m}, t_2 = 1.5 \mu\text{m}$
Temperature change	- 100°C	- 100°C
Deflection (of total thickness)	2%	6 times
Stresses across the thickness	Uniform (150 MPa)	Stress gradient (~70MPa)
Stresses over the in-plane	Uniform	Nonuniform
Curvature	Uniform (0.9 m⁻¹)	Nonuniform (~550 m⁻¹)
Stress vs. curvature	Stoney formula	Complicated
Geometric nonlinearity Bifurcation	No	Yes

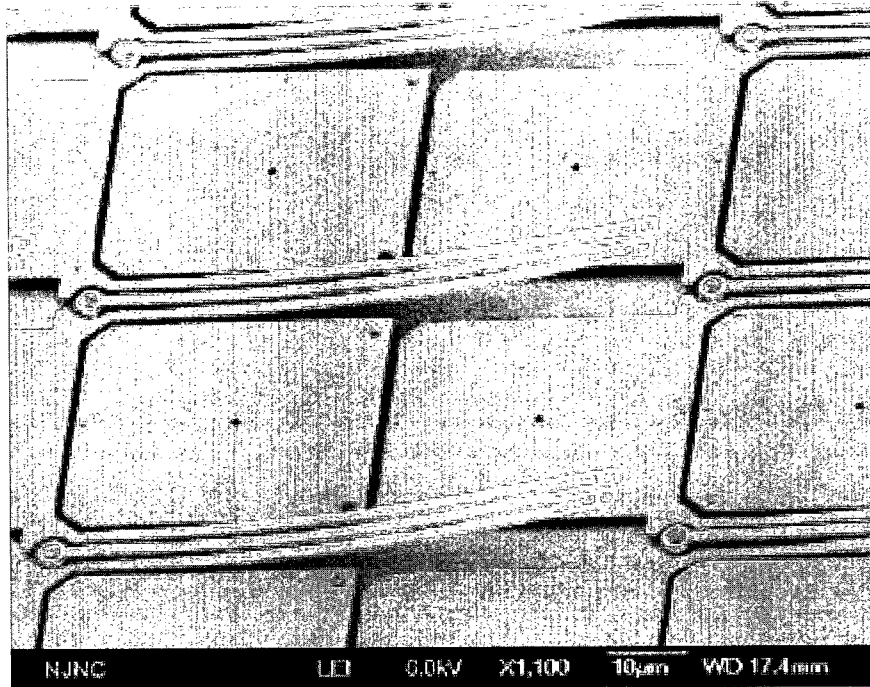


Fig. 1.1: A scanning electron microscope (SEM) image of MEMS-based IR focal plan array (FPA) (Jones *et al.*, 2009).

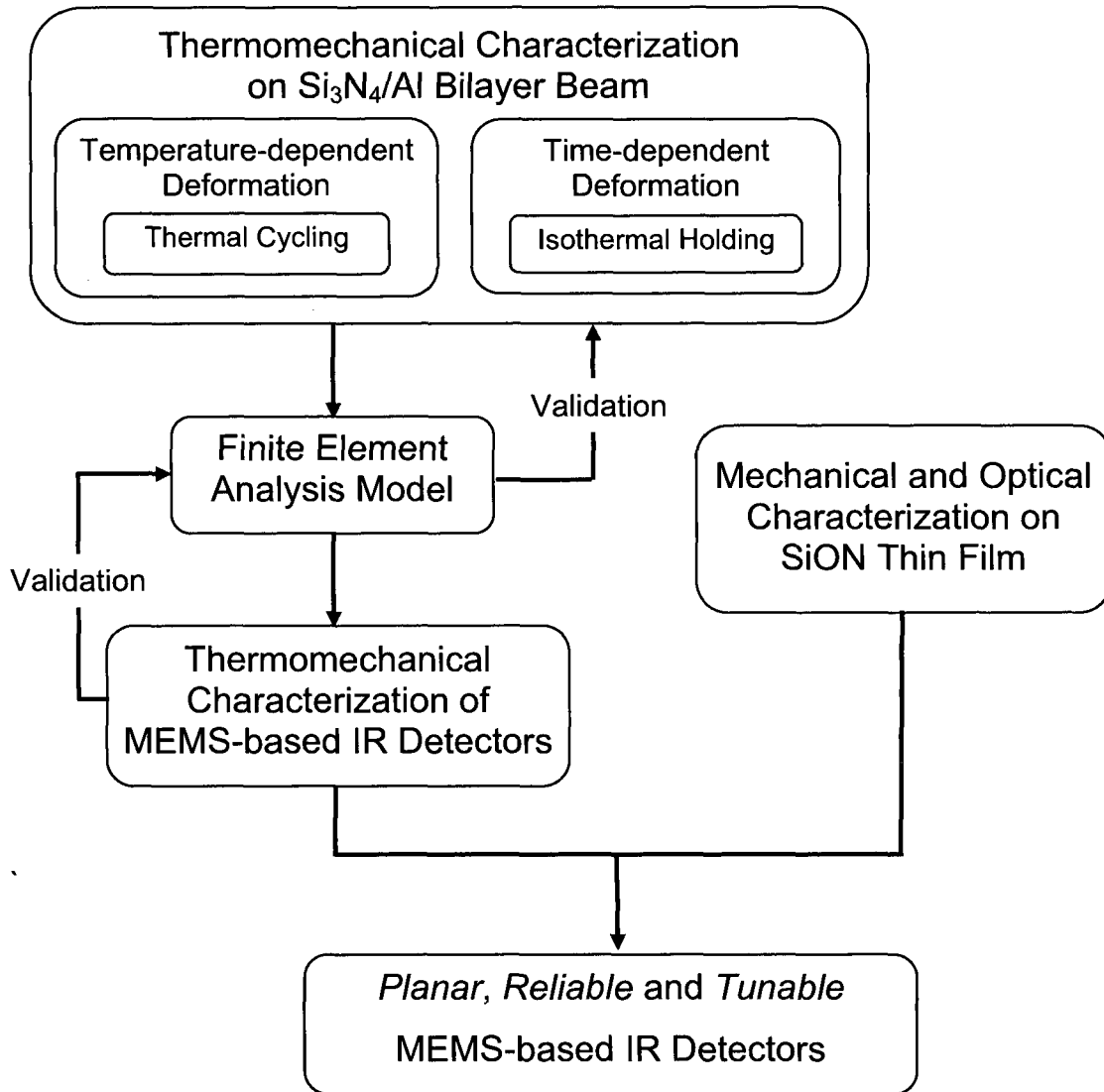
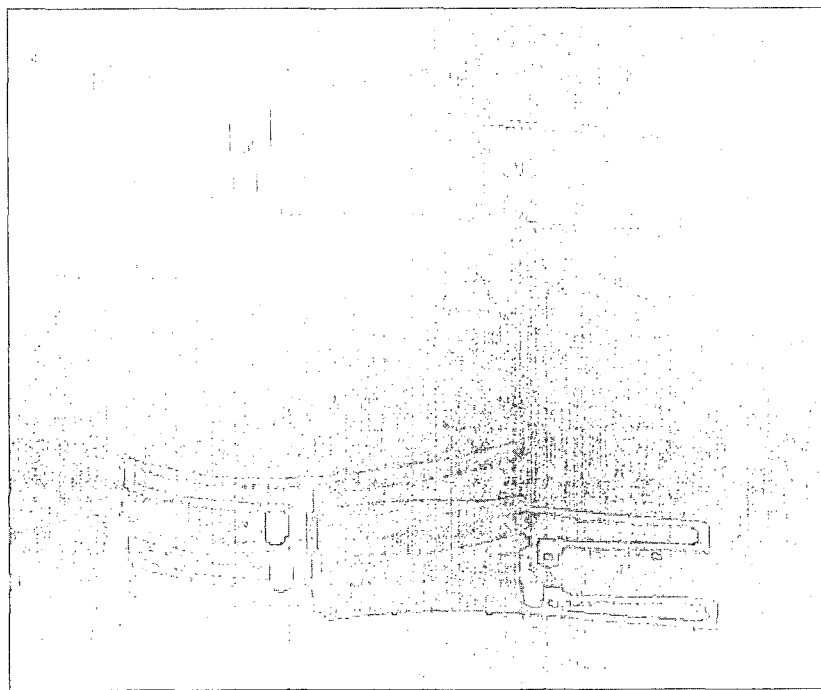


Fig. 1.2: Organizational chart for the dissertation research.



(a)



(b)

Fig. 1.3: (a) A portion of a 5x5 IR FPAs of pixels (Amantea *et al.*, 1998) and (b) double-cantilever IR FPAs (Hunag *et al.*, 2008) have undesired initial bending due to the imbalanced residual stresses in the bimaterial cantilever structures.

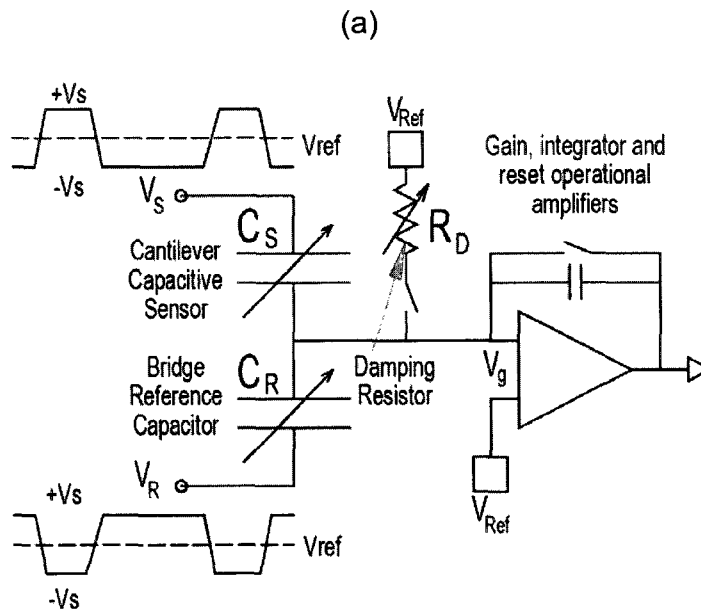
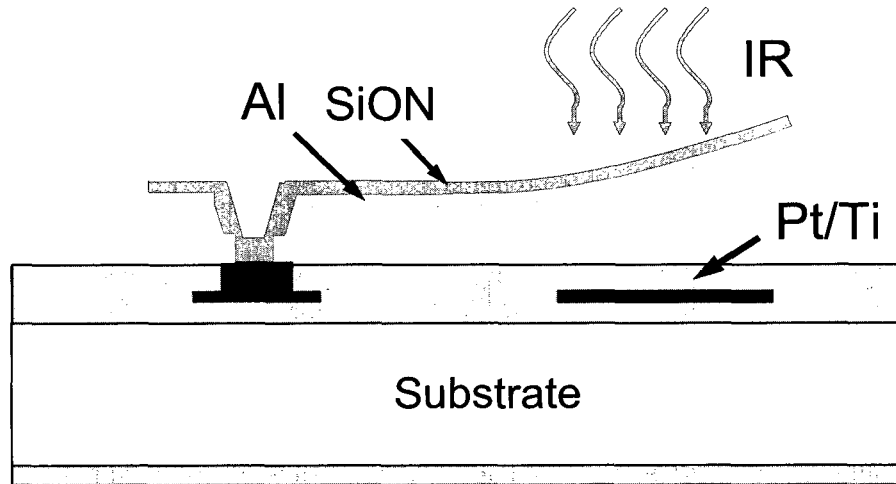


Fig. 1.4: (a) The schematic view of the bending of a pixel of MEMS-based IR FPAs during sensing operation and (b) read-out circuit diagram at each pixel (Hunter *et al.*, 2006).

CHAPTER 2: EXPERIMENTAL METHODS

This chapter describes the specimen preparation and experiment setup. In order to characterize the temperature- and time-dependent behavior, mechanical and material properties of bilayer microcantilevers and composite materials, two types of specimen ($\text{Si}_3\text{N}_4/\text{Al}$ microcantilevers and SiON films) are fabricated in Section 2.1 and Section 2.2, respectively. Subsequently, Section 2.3 and Section 2.4 describe the methods of thermomechanical and mechanical/material characterization on bilayer cantilevers and SiON films, respectively.

2.1. Fabrication Process of Bilayer Microcantilevers

The fabrication process of bilayer microcantilevers, including beams and MEMS-based IR detectors, are described in Fig. 2.1.

2.1.1. Substrate Preparation

The bilayer microcantilever structures are fabricated on a <100> silicon wafer. First, the wafer is cleaned using the RCA cleaning technique, in order to obtain high performance and reliable structures and to prevent contamination of the process equipment (Fig. 2.1(a)).

The RCA cleaning procedure is comprised of three sequential steps used sequentially (Madou, 1997):

1. Organic clean: removal of insoluble organic contaminants with a water (H_2O), hydrogen peroxide (H_2O_2) and ammonium hydroxide (NH_4OH) solution in a 5 to 1 to 1 ratio.
2. Oxide strip: removal of a thin silicon dioxide layer where metallic contaminants may accumulate as a result of step 1, using a diluted hydrofluoric acid (HF) solution in a 50 to 1 ratio.
3. Ionic clean: removal of ionic and heavy metal atomic contaminants using a solution of water, hydrogen peroxide and hydrochloric acid in a 6 to 1 to 1 ratio.

2.1.2. Sacrificial Layer

The second step in the fabrication process is to deposit a 2.5 μm thick polyimide layer, which acts as a sacrificial layer (Fig. 2.1(b)). The use of commercial PI-2610 polyimide (HD Microelectronics) not only allows for an all-dry final structure release step that overcomes stiction problems, but also process compatibility with deposition and patterning of bilayer structural layers, i.e. plasma-enhanced chemical vapor deposited (PECVD) Si_3N_4 and e-beam evaporated Al (Bagolini *et al.*, 2002; Huang *et al.*, 2008; Lin *et al.*, 2008). PI-2610 is a spin-on microelectronic material specifically conceived for dry etching, and it has a transition-to-glass (TG) temperature above the post-processing limit temperature of 400 °C (HD Microsystems, 2000). Since the PI-2620 polyimide is not a photon-sensitive material, it cannot be patterned directly by photolithography and

photoengraving. Therefore, the hard mask process is adopted for patterning. The detailed process flow, shown in Fig. 2.2, for the sacrificial polyimide layer is described as follows.

1. First, an adhesion promoter VM-652 is coated on silicon wafers at 3000 rpm for 30 s to enhance adhesion between the polyimide and the wafer, and then baked at 90 °C for 10 min in an oven. After pouring the commercial PI 2610 polyimide on the wafer, a 6 s delay is allowed prior to spinning. Subsequently, the polyimide is spun on wafers at a speed of 2000 rpm for 30 s. Then a two-step bake on a hotplate, at 90 °C and 180 °C, both for 90 s, is conducted to evaporate part of the solvent, so as to stabilize the film (HD Microsystems, 2000 and Bagolini *et al.*, 2002). The polyimide is then further cured in an N₂ atmosphere at 350 °C for one hour (Fig. 2.2(a)). Although the polymerization of PI 2610 occurs at about 200 °C, higher baking temperatures of up to 350 °C are preferred as they allow for complete solvent evaporation and yield a higher TG temperature of the cured polymer. Fig. 2.3 shows the polyimide thickness before and after the curing process (HD Microsystems, 2000). In this study, the thickness of the cured sacrificial polyimide layer is about 2.5 μm.
2. To create the anchors of the microcantilever beams, an etching process is performed on the polyimide sacrificial layer. A 500 nm thick silicon oxide (SiO₂) layer is deposited as a hard mask layer using STSTM PECVD unit, due to the

good adhesion between SiO₂ and the polyimide (Bagolini *et al.*, 2002) (Fig. 2.2(b)). Deposition parameters of the SiO₂ layer are listed in Table 2.1. The Shipley S1818 positive photoresist from MICROPOSIT™ is used to pattern SiO₂. The 1 μm thick S1818 is coated on the SiO₂ layer at 1000 rpm followed by a 115 °C prebake for 60 s. Subsequently, the photoresist-coated wafer is exposed using a mask aligner (MA6, Karl Suss) for 8 s, with a light intensity of 10 mW/cm². The exposed S1818 is removed from the wafer in the MF-321 developer, as shown in Fig. 2.2(c).

3. In this work, the SiO₂ is patterned by reactive ion etching (RIE) (790, Plasma-Therm) with gases sulfur hexafluoride (SF₆) and helium (He), as shown in Fig. 2.2(d). The etching recipe is listed in Table 2.2.
4. The anchor holes with vertical sidewalls on the polyimide layer are fabricated using RIE with O₂ plasma, which is a good controllable anisotropic dry etching process (Fig. 2.2(e)). The etching recipe is listed in Table 2.2.
5. The SiO₂ layer is easily removed using Buffered oxide etch (BOE), which does not etch the polyimide, as shown in Fig. 2.2(f). The etching rate is approximately 300 nm/min.

2.1.3. Structure Layer Deposition and Patterning

A 200 nm thick Al layer is deposited using an electron beam thermal evaporator (Auto 306, BOC Edwards), followed by the deposition of a 200 nm thick of Si₃N₄ layer using STS™ PECVD on the Al layer. The operational parameters for the

Si₃N₄ deposition are given in Table 2.1. Again, a standard photolithography with S1818 is employed to pattern these structural layers (Si₃N₄/Al). Next, these two layers are etched using phosphoric acid (H₃PO₄) and RIE with SF₆ and He, respectively Fig. 2.1 (c). The Al layer is etched by Aluminum Etchant Type A from Transense (Williams *et al.*, 2003; Williams and Muller, 1996). This solution is a mixture of 80 %H₃PO₄, 5 % nitric acid (HNO₃), 5 % acetic acid (CH₃COOH) and 10 % H₂O. The etching is performed at 50 °C. Similar to the masking of SiO₂, the Si₃N₄ is also patterned by RIE using a mixture of SF₆ and He at a rate of 109 nm/min.

2.1.4. Cantilever Release

The cantilevers are released once the sacrificial polyimide layer is removed, by isotropic dry etching in O₂ plasma with a Plasma Asher (Plasmod, March Instruments), as shown in Fig. 2.1(d). At the power level of 150 W, a lateral etch rate of 2 nm/min for the polyimide has been measured. Fig. 2.4 shows the released microcantilevers beams and MEMS-based IR detectors.

2.2. Fabrication of Silicon Oxynitride Films

All silicon substrates are pre-cleaned using a modified RCA process and treated with a 40 % buffered hydrofluoride (HF) solution before the sputter deposition. Five different types of silicon oxynitride films with a thickness of approximately 1 μm are deposited on n-type (100) silicon wafer substrates at room temperature

by a Discovery 18 RF magnetron sputtering system (from Denton Inc., Moorestown, NJ). Among the five sputtered SiON specimens, two specimens, silicon oxide and silicon nitride films, are directly sputtered from pure (> 99.9 % purity) silicon oxide and silicon nitride targets (from Kurt J. Lesker Inc., Clairton, PA) in the presence of argon plasma, respectively. The other three SiON thin films with different nitrogen/oxygen ratios are deposited by co-sputtering the silicon oxide and silicon nitride targets. The compositional variation of oxygen and nitrogen in the three SiON films is achieved by arbitrarily adjusting the radio frequency (RF) powers (listed in Table 2.3) applied to the silicon oxide and silicon nitride targets. The flow rate of argon is 25 SCCM (standard cubic centimeters per minute at STP) to maintain a sputtering pressure at 2 mTorr during the deposition. Subsequently, these SiON films are subjected to RTA at 400 °C for 60 s in a nitrogen ambient environment, using a RTP-600S rapid thermal processing (RTP) system (Modular Process Technology Corp., San Jose, CA) to examine the influence of thermal processing. In this study, SiO_x , SiN_y and SiO_xN_y are adopted to represent the sputtered silicon oxide, silicon nitride, and co-sputtered silicon oxynitride films, respectively.

2.3. Thermomechanical Response Measurement

To measure the *in situ* deformation of the microcantilevers as a function of temperature and/or time change, a system containing a heating/cooling stage and an interferometer microscope are constructed as depicted in Fig. 2.5.

2.3.1. Interferometer

A visual representation of the full-field out-of-plane deformation of microcantilevers with 100 nm resolution is achieved (Fig. 2.6) when a beam of white light passes through a 10× microscope objective to the surface of the microcantilever. Subsequently, an interferometer beam splitter reflects half of the incidence beam to the reference surface inside the microscope. These two beams are recombined and projected onto the camera to generate a signal that is proportional to the resultant beam intensity produced by the interference effect. These signals are then transferred into the spatial frequency domain, and the surface height for each point is obtained from the complex phase as a function of the frequency (Degroot and Deck, 1993).

2.3.2. Heating/Cooling Stage

To induce the different temperature regions applied throughout the test, a thermal system, with a closed-loop temperature controller, a micro-heating/cooling stage and a cooling system, is used (HCP302-STC200, INSTEC Inc.) (Fig. 2.7). The resolution of the thermal system is approximately 1 °C. complete details regarding the technical specification can be found in Table 3.4 (INSTEC Inc, 2006).

2.3.3. Data Analysis

Fig. 2.8(a) and Fig. 3.9(a) show the three-dimensional WYKO image of the

microcantilevers. The image serves as the determinant for the full-field out-of-plane displacements ($w(x,y)$) generated from the microcantilevers. From the image, the curvature along the length of the microcantilever beam (the x-direction) can be determined by fitting $w(x,y)$ with the following second-order polynomial and then differentiating as appropriate:

$$\kappa(x, y) \approx \partial^2 w(x, y) / \partial x^2 \quad (2.1)$$

where κ is the curvature and $w(x,y)$ are the plane displacements. Fig. 2.8(b) and Fig. 2.9(b) depict a series of surface profiles of the bimaterial I.) beam and II.) plate at five different temperatures. These profiles show that the deformation increases with increasing temperature. This measurement setup provides a suitable representation for the overall thermomechanical response using calculated curvatures at each temperature.

2.4. Material and Mechanical Characterization

2.4.1 Energy Dispersive X-ray Analysis (EDX)

After SiON film deposition, the Energy dispersive X-ray (EDX) spectroscopy is employed to characterize the stoichiometric composition. A JOEL 6100 (JOEL Ltd., Tokyo, Japan) scanning electron microscope (SEM) equipped with an energy dispersive x-ray (EDX) spectrometer (from Oxford Instruments plc, Oxfordshire, UK) is employed to quantitatively analyze the compositional content

of the sputtered SiON films. Based on the result from the Monte Carlo simulation, a low electron beam voltage of 5 kV is selected for the EDX analysis, to ensure that the interaction volume of the electron beam and specimen is confined within the 1 μm top layer of the SiON films. ISO-9000 compliance standards (from Geller Microanalytical Laboratory Inc., Topsfield, MA) including pure Si, SiO₂ and Si₃N₄ are used to calibrate the instrument and create standard element profiles prior to the EDX spectrum acquisition and quantitative analysis. A Phi-Rho-Z correction procedure is used for all SiON specimens in the EDX quantitative analysis.

2.4.2. Fourier Transform Infrared Spectrometry (FT-IR)

The chemical bonding and microstructure within the SiON films are identified by Fourier transform infrared spectroscopy (FT-IR) with an IFS 66/s FT-IR spectrometer (from Bruker Optics Inc., Billerica, MA). A K-Br light splitter and a DTGS detector are employed in the FT-IR analysis to obtain the mid-infrared (MIR) absorbance spectra (400 – 4000 cm^{-1}) of SiON films in a nitrogen ambient environment. A background spectrum of Si wafer substrate was also obtained to normalize the spectra of SiON films, eliminating the contributions from Si substrate, instrumentation and atmosphere. A total of 50 scans are conducted with a resolution of 10 cm^{-1} for each background and SiON specimen. The FT-IR spectra of SiON films are obtained and then further analyzed using the OPUS (from Bruker Optics Inc.) software package.

2.4.3 Nanoindentation

Depth-sensing instrumentation, or nanoindentation, is a popular technique for the estimation of mechanical properties of materials down to nanoscale. An image of the Hysitron TriboIndenter™ nanoindentation system is shown in Fig. 2.10(a), together with a schematic of a typical load-displacement curve obtained by the nanoindenter (Oliver and Pharr, 2004; Onishi *et al.*, 1999) (Fig. 2.10(b)). Nanoindentation can reveal a wealth of detailed information about the mechanisms and mechanics of the studied thin film materials, including the modulus of elasticity, hardness, surface adhesion, creep, stress relaxation behaviors, etc (Li and Ngan, 2004; Lucas and Oliver, 1999; Oliver and Pharr, 1992, 2004; Poisl *et al.*, 1995; Schuh and Nieh, 2003, 2004; Schwaiger *et al.*, 2003; Tymiak *et al.*, 2001). The indent load resolution of the Hysitron TriboIndenter™ is 1 nN with a noise floor of 100 nN; and the indent displacement resolution is 0.02 nm with a noise floor of 0.2 nm. A standard Berkovich tip (from Hysitron Inc.) with a tip radius of approximately 150 nm and a half-angle of 65.35° is chosen for the experiments. The machine compliance calibration for the transducer-tip configuration and tip area function calibration are performed with a standard fused silica sample before proceeding with all indentation experiments.

Table 2.1: PECVD deposition parameters of SiO₂ and Si₃N₄ films.

	SiO ₂	Si ₃ N ₄
RF power (W)	30	60 W
RF frequency (Hz)	13.56 M	380 k
Pressure (mTorr)	900	550
N ₂ flow rate (sccm)	392	1960
NH ₃ flow rate (sccm)	0	20
N ₂ O flow rate (sccm)	1420	~
SiH ₄ flow rate (sccm)	10	40
Deposition rate (Å/sec)	10.42	7.87

Table 2.2: RIE etching recipes of SiO₂, Si₃N₄ and polyimide films.

	SiO ₂	Si ₃ N ₄	Polyimide
Power (W)	110	110	300
Pressure (mTorr)	75	75	100
SiF ₆ flow rate (sccm)	20	20	0
He flow rate (sccm)	30	30	0
O ₂ flow rate (sccm)	0	0	40
Etching rate (nm/sec)	56	100	800

Table 2.3: Sputtering deposition recipes of Silicon oxynitride films.

	SiN_y	SiO_xN_y1	SiO_xN_y2	SiO_xN_y3	SiO_x
RF Power					
<i>SiO₂ Target (W)</i>	0	100	300	300	300
<i>Si₃N₄ Target (W)</i>	300	300	300	100	0
Pressure (mTorr)			2		
Ar flow rate (sccm)			25		

Table 2.4: Technical specification of HCP 302 (INSTECH Inc, 2006).

Temperature control sensor	100 Ω Platinum RTD
Control method	Switching PID
Temperature range	-150 °C* to 400 °C
Temperature accuracy	± 0.3 °C to 100 °C, ± 0.5 °C to 200 °C, ± 0.8 °C to 400 °C or below ambient
Temperature stability	± 0.1 °C at 100 °C
Minimum heating and cooling rate	+0.1 °C/hour
Maximum heating rate	+100 °C/min at 37 °C
Maximum cooling rate*	-50 °C/min at 37 °C
Sample area	50mm \times 60mm

*Requires use of the INSTECH liquid nitrogen pump accessory (LN2-P2A/U)

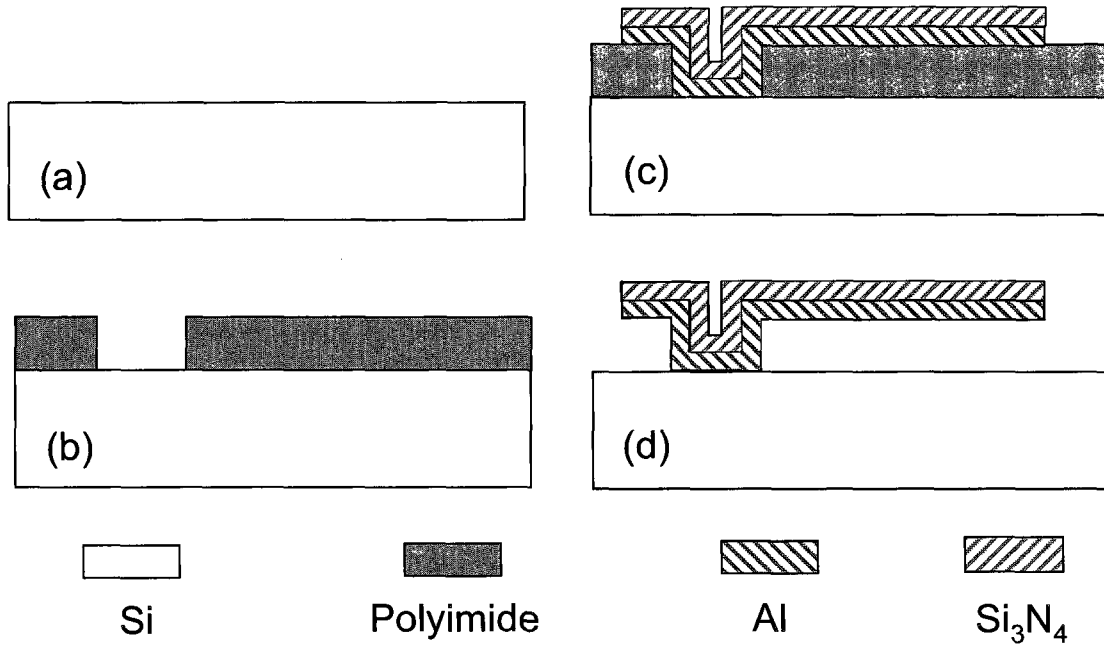


Fig. 2.1: The general fabrication process of bilayer microcantilevers.

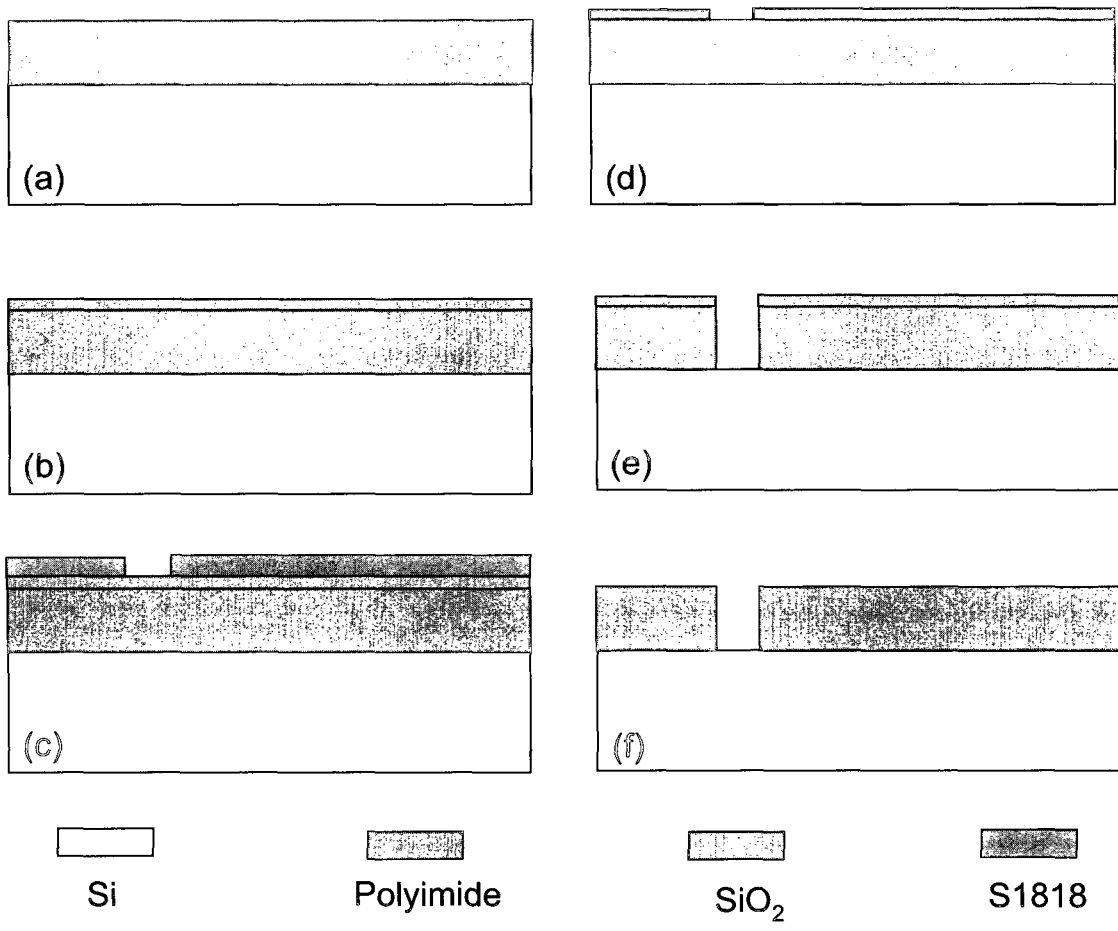


Fig 2.2: Fabrication process of polyimide sacrificial layer.

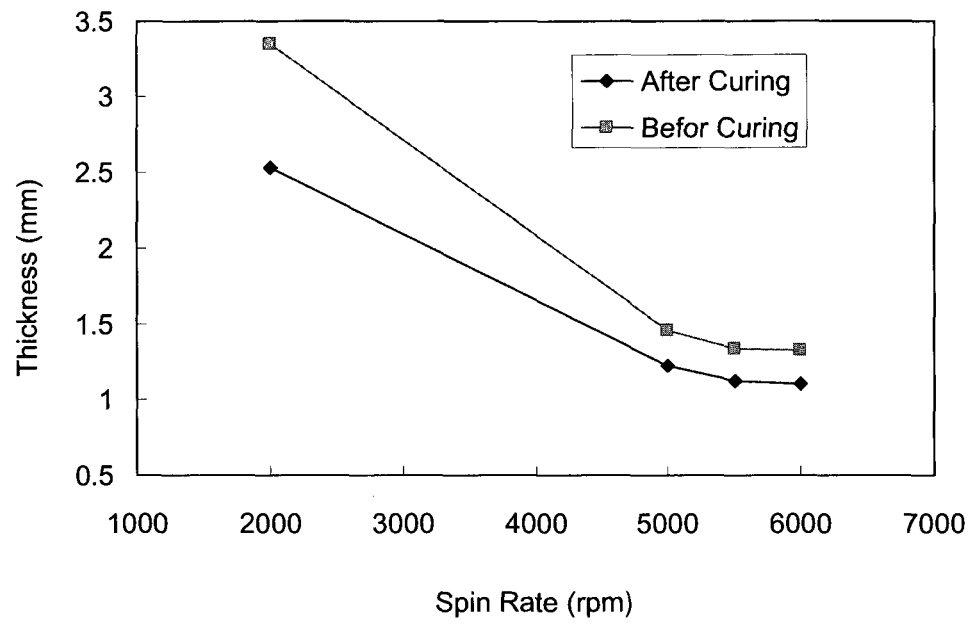
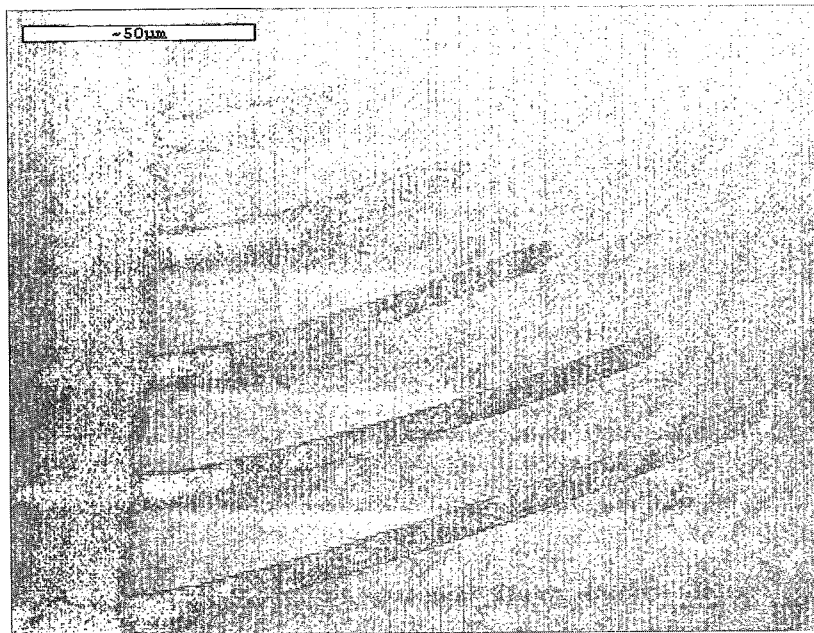
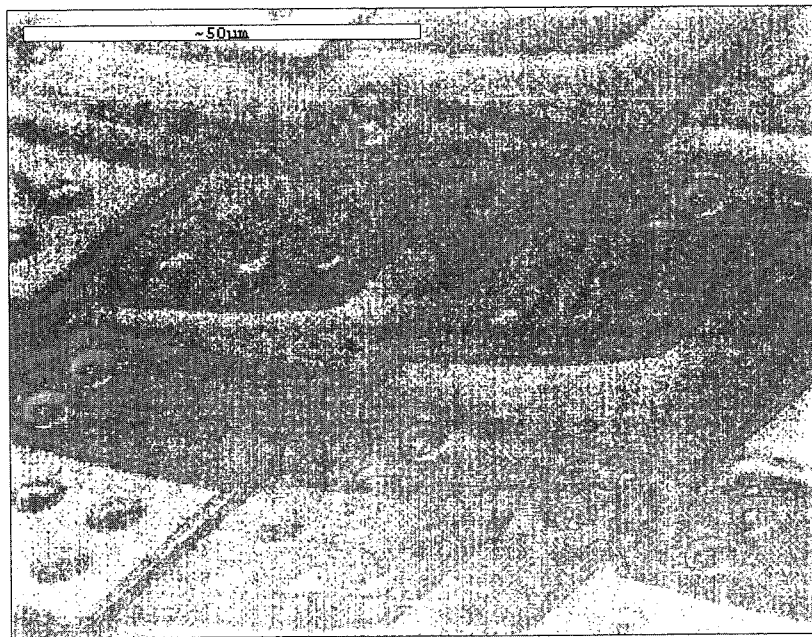


Fig. 2.3: The thickness of polyimide sacrificial layer before and after curing.

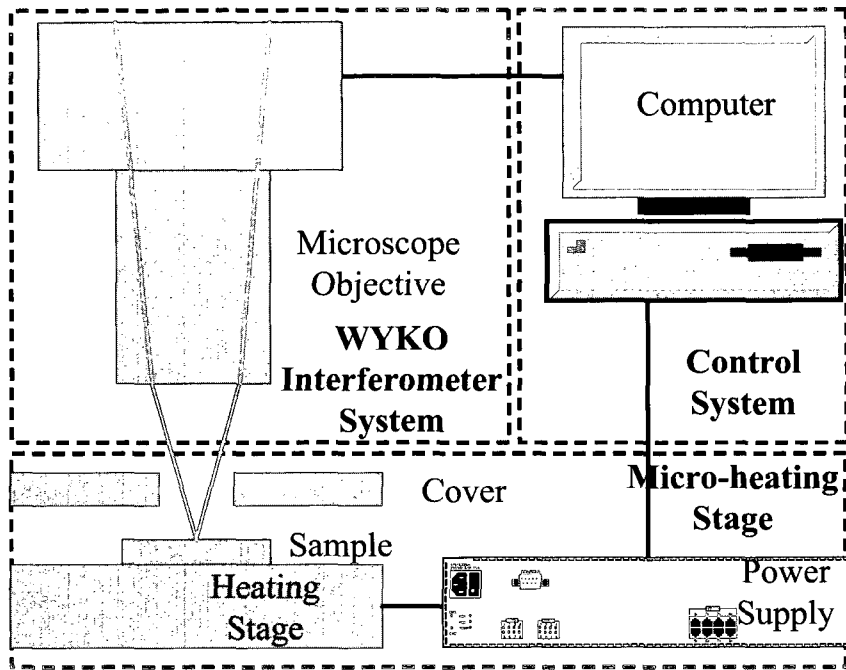


(a)

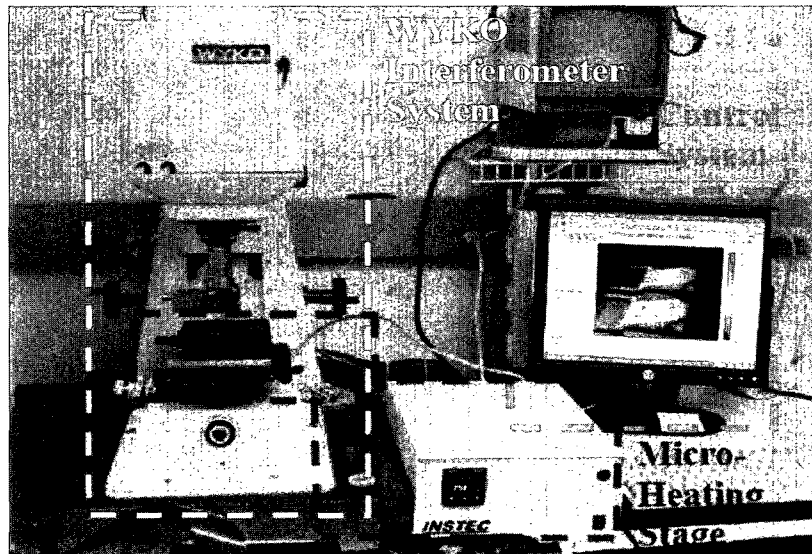


(b)

Fig. 2.4: SEM images of (a) bilayer microcantilever beams and (b) MEMS-based IR detectors.



(a)



(b)

Fig 2.5: (a) a schematic view and (b) image of setup for *in situ* deformation measurement of microcantilevers during thermal loading.

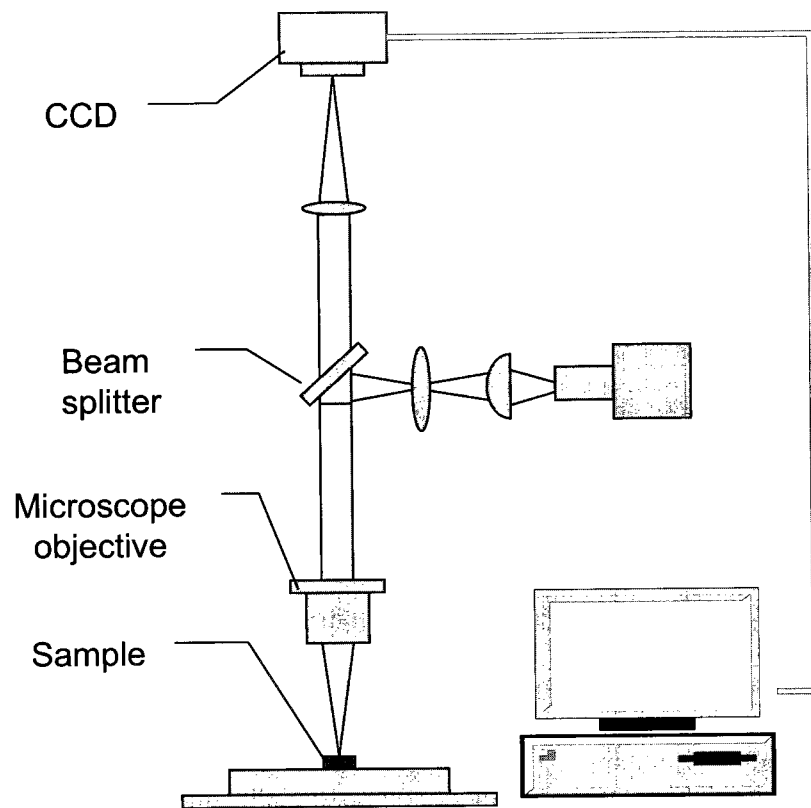


Fig. 2.6: The schematic view of setup of Interferometer.



Fig. 2.7: Microheating stage (HCP302) from INSTEC Inc in the experiment setup.

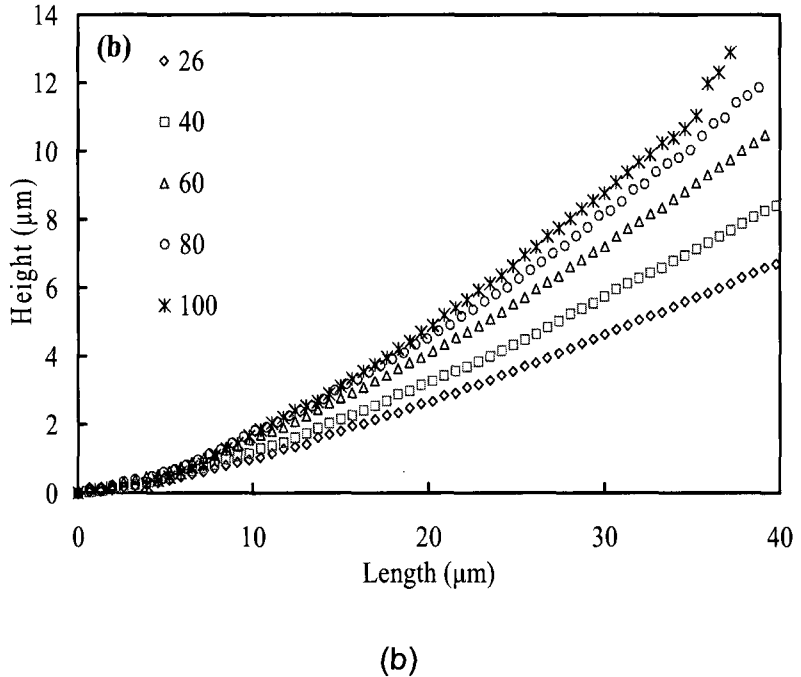
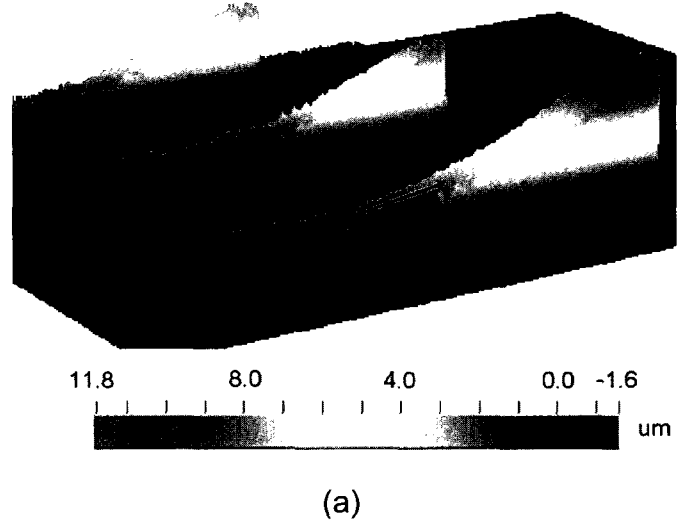
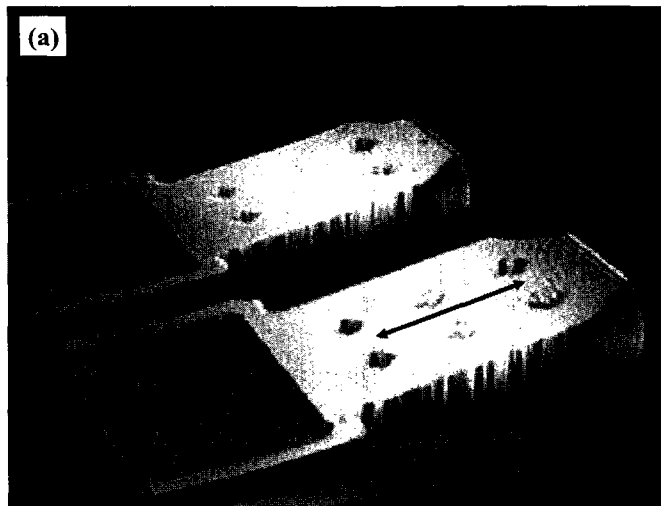
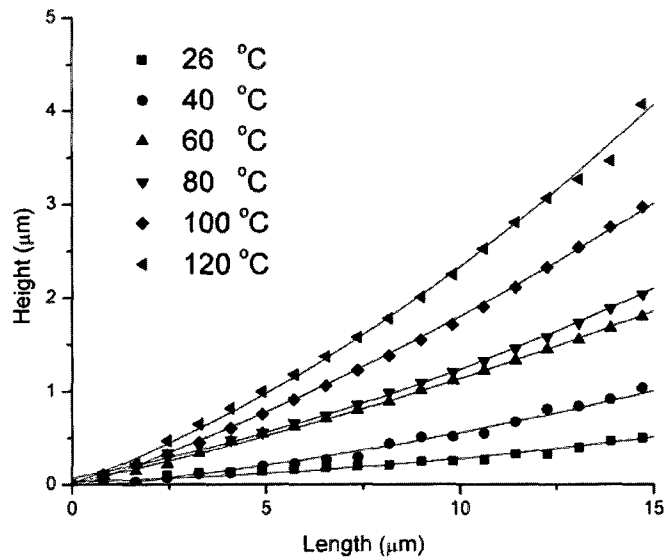


Fig. 2.8: (a) Image from the WYKO interferometric microscope showing the topology of the top surface of the microcantilever beams and (b) surface profiles of the bilayer beam at different temperatures along the arrow line in (a).

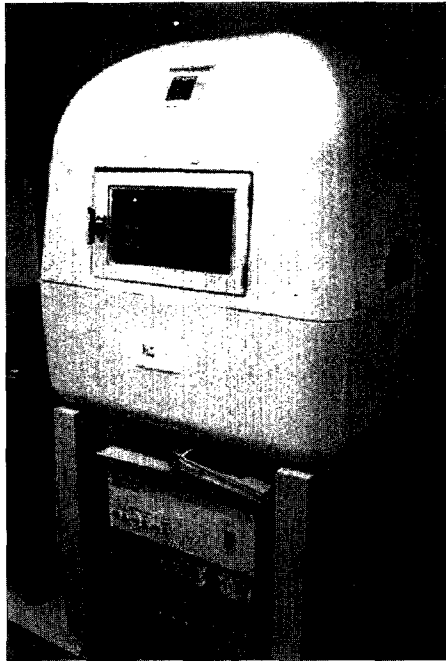


(a)

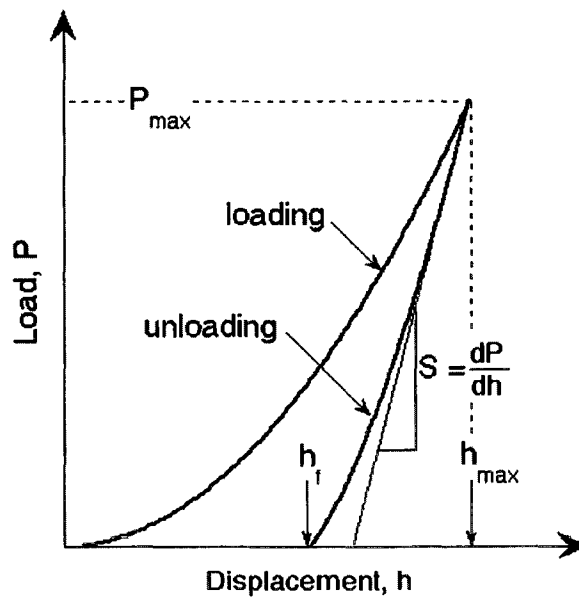


(b)

Fig. 2.9: (a) Image from the WYKO interferometric microscope showing the topology of the top surface of the MEMS-based IR detectors and (b) surface profiles of detectors at different temperatures along the arrow line in (a).



(a)



(b)

Fig. 2.10: (a) Hysitron TribolIndenter™ nanoindentation system (Courtesy Prof. Klapperich) and (b) a typical load-displacement curve.

CHAPTER 3: TEMPERATURE-DEPENDENT DEFORMATION OF BILAYER MICROCANTILEVER BEAMS

3.1. Introduction

With the ability to serve as both sensors and actuators, bilayer microcantilevers abound in MEMS applications, such as microelectromechanical variable blaze gratings (Burns and Bright, 1998), infrared detectors (Senesac *et al.*, 2003), DC electrical relays and contacts (Miller *et al.*, 2001), calorimetric high-frequency detectors (Lee *et al.*, 2007), radio frequency (RF) components including switches (Chang and Chang, 2000) or variable capacitors (Bell *et al.*, 2003), biological (Raiteri *et al.*, 2001) or chemical (Baselt *et al.*, 2003) sensors, and vertical (Riethmuller and Benecke, 1988) or lateral (Dai *et al.*, 2001) actuators. Unfortunately, the manufacturability, planarity and reliability for such bilayer microcantilevers have been inadequate. As mentioned in Chapter 1, after the bilayer microcantilevers are released, they invariably deflect, due to the residual strain/stress mismatch in the bilayer system, as shown in Fig. 1.3. The residual strain mismatch induces a curvature in the thin films. This curvature significantly compromises the performance of these bilayer microcantilever structures. Therefore, curvature modification is one of the important topics in the post-process assessment of microcantilever-based devices. In this chapter, the temperature-dependent deformation of bilayer microcantilever is characterized by using a thermal cycling technique, and the experimental results are interpreted

by analytical models. The results presented by this chapter provide a solution for planarization in MEMS-based IR detectors.

3.2 Theoretical Background

3.2.1 Thermal Induced Bending Model

Timoshenko's classical model for a bimetallic strip thermostat subjected to uniform heating (Timoshenko, 1925) provides a starting point for this analysis of the thermomechanical response of the bilayer microcantilevers. To find the general equation that depicts the relationship between bending curvature and temperature change, a multilayer bending model is derived Timoshenko's classic beam bending theory (Timoshenko, 1925). There are 4 assumptions in the model:

- 1) The layer thickness is much smaller than the radius of curvature; that is, $h \ll R$, where R is the radius of curvature measured by the interferometer, and h is the layer thickness.
- 2) The relationship between stress and strain is linear, given by Young's modulus of elasticity.
- 3) The strains and stresses are isotropic in both the x- and y-directions.
- 4) The strain throughout a bent bilayer microcantilever is determined only geometrically by the curvature.

The multilayer cantilever is shown in Fig. 3.1. For a single-layer cantilever without any external load, the pure bending strain (ε_b) can be obtained from the normalized difference in circumferences (c) at a distance (z) from the reference plane, as shown in Fig. 3.2. The equation for this relationship is:

$$\begin{aligned}\varepsilon_b &= \varepsilon_0 + \frac{c_z - c_0}{c_0} = \varepsilon_0 + \frac{(R - z)\theta - R\theta}{R\theta} \\ &= \varepsilon_0 - \frac{z}{R} = \varepsilon_0 - z\kappa\end{aligned}\quad (3.1)$$

where c_0 is the circumference at the reference plane ($z=0$), c_z is the circumference at position z , ε_0 is the reference strain at the reference plane, R is the radius of curvature, θ is the bending angle and κ is the bending curvature (where $\kappa = 1/R$).

When the microcantilever, which consist of multiple layers bonded together, is uniformly heated or cooled from T_1 °C to T_2 °C, and if the coefficients of thermal expansion (α_i) of these layers are different, the heating or cooling will produce a bending of the microcantilever. The thermal-induced expansion or contraction of these layers will produce a strain on each layer, given by $\varepsilon_{\Delta T,i} = \alpha_i(T_2 - T_1) = \alpha_i\Delta T$. In general, the difference between the geometry-imposed strain and the thermal-induced strain is given by:

$$\varepsilon_i = \varepsilon_b - \varepsilon_{\Delta T,i} = \varepsilon_0 - z\kappa - \alpha_i\Delta T \quad (3.2)$$

where the subscripts refer to the layer numbers. Using this relationship, the stress (σ_i) can be written as:

$$\sigma_i = E_i\varepsilon_i = E_i(\varepsilon_0 - z\kappa - \alpha_i\Delta T) \quad (3.3)$$

where E_i is Young's modulus. The bending force F and the moment M can also be obtained easily by integrating the stress along the cross section in the vertical direction.

$$F = \int_0^h \sigma_i dz = \int_0^h E_i(\varepsilon_0 - \kappa z - \alpha_i\Delta T) dz \quad (3.4a)$$

$$M = \int_0^h \sigma_i z dz = \int_0^h E_i(\varepsilon_0 - \kappa z - \alpha_i\Delta T) z dz \quad (3.4b)$$

When the microcantilever is subjected to an elevated temperature change (ΔT), the force and moment at equilibrium must be zero, resulting in the following equations:

$$A\varepsilon_0 - B\kappa = F \quad (3.5a)$$

$$B\varepsilon_0 - D\kappa = M \quad (3.5b)$$

These equations can be written in the matrix form, as shown below:

$$\begin{bmatrix} A & -B \\ B & -D \end{bmatrix} \begin{bmatrix} \varepsilon_0 \\ \kappa \end{bmatrix} = \begin{bmatrix} F \\ M \end{bmatrix} \quad (3.6)$$

where A is the extensional stiffness, B is the bending-extension coupling stiffness, D is the bending stiffness, and F and M are the force and moment induced by the temperature change. They can be expressed as:

$$A = \int E dz = E_1 h_1 \sum_{i=1}^N m_i n_i \quad (3.7a)$$

$$B = \int E z dz = \frac{E_1 h_1^2}{2} \sum_{i=1}^N (m_i^2 + 2m_i p_i) n_i \quad (3.7b)$$

$$D = \int E z^2 dz = \frac{E_1 h_1^3}{3} \sum_{i=1}^N (m_i^3 + 3m_i^2 p_i + 3m_i p_i^2) n_i \quad (3.7c)$$

$$F = \int E \alpha dz = E_1 h_1 \sum_{i=1}^N m_i n_i \alpha_i \Delta T \quad (3.7d)$$

$$M = \int E \alpha z dz = \frac{E_1 h_1^2}{2} \sum_{i=1}^N (m_i^2 + 2m_i p_i) n_i \alpha_i \Delta T \quad (3.7e)$$

where $m_i = \frac{h_i}{h_1}$, $n_i = \frac{E_i/(1-\nu_i)}{E_1/(1-\nu_1)}$, $p_i = \frac{z_i}{h_1} = \frac{1}{h_1} \sum_{j=1}^{i-1} h_j = \sum_{j=1}^{i-1} m_j$, and N is the total number of layers. Using the matrix from, the bending curvature κ can be obtained.

$$\kappa = \frac{AM - BF}{B^2 - AD} \quad (3.8)$$

Eq. 3.8 provides a general model for the bending curvature of multilayer microcantilevers. Eq. 3.8 can further be reduced for bilayer microcantilevers as:

$$\kappa = \frac{6m_2n_2(1+m_2)(\alpha_1 - \alpha_2)\Delta T}{h_2(1 + 4m_2n_2 + 6m_2^2n_2 + 4m_2^3n_2 + m_2^4n_2^2)} \quad (3.9)$$

Eq. 3.9 is Timoshenko's well-known bilayer bending equation. Therefore, the use of this model is validated. The thermomechanical response can also be obtained by rewriting Eq. 3.9 to:

$$\frac{\partial \kappa}{\partial T} = \frac{6m_2n_2(1+m_2)(\alpha_1 - \alpha_2)}{h_2(1 + 4m_2n_2 + 6m_2^2n_2 + 4m_2^3n_2 + m_2^4n_2^2)} \quad (3.10)$$

3.2.2 Residual Strain Induced Bending Model

For bilayer structures, the first equation contributed by Stoney provides an

expression for the curvature (R) of a film and substrate system in terms of the uniform film stress or strain (Stoney, 1909):

$$\sigma_r = \frac{E_s h_s^2}{6(1-\nu_s)h_f R} \quad (3.11)$$

where $E_s/(1-\nu_s)$ is the biaxial modulus of the silicon substrate, h_s and h_f are the thickness of the silicon substrate and the nitride film, respectively.

Eq. 3.11 follows from an analysis of a film-substrate system and is based on several assumptions (Finot *et al.*, 1997; Freund, 2000; Freund *et al.*, 1999). The main assumptions are:

- 1) Both the film thickness and substrate thickness are small compared to the lateral dimensions.
- 2) The film thickness is much smaller than the substrate thickness.
- 3) The substrate material is homogeneous, isotropic and linearly elastic; and the film material is isotropic.
- 4) Edge effects near the periphery of the substrate are inconsequential.
- 5) All physical quantities such as Young's modulus and Poisson's ratio are invariant under changes in positions parallel to the interface.
- 6) All stress gradients in the direction of the thickness vanish throughout

the material.

- 7) The strains and the rotations are infinitesimally small.

Continuous efforts have been made to explore the range of applicability of some of these assumptions (Finot *et al.*, 1997; Freund, 2000; Freund *et al.*, 1999). For example, both assumptions 2) and 3) have been challenged, where some film-substrate systems contain large, nonlinear deformations (Finot *et al.*, 1997; Freund, 2000; Freund *et al.*, 1999). Assumption 2) has been disputed in cases where most of MEMS structures are film-film systems (bilayer microcantilevers). The Stoney equation may also result in large errors, and more exact expressions are required. The complete formula, an extension on the Stoney equation is obtained by using different approaches (Klein, 2000; Hsueh, 2002; Freund *et al.*, 1999; Huang and Zhang, 2006). Using the same terms as in Eq. 3.9, the residual strain mismatch-induced bending curvature is

$$\kappa = \frac{6m_2n_2(1+m_2)(\varepsilon_{res,2} - \varepsilon_{res,1})}{h_1(1+4m_2n_2+6m_2^2n_2+4m_2^3n_2+m_2^4n_2^2)} \quad (3.12)$$

where $\varepsilon_{res,1}$ and $\varepsilon_{res,2}$ are the residual strains in layer 1 and layer 2. Note that both Eq. 3.11 and Eq. 3.12 share the assumption that the film strain is uniformly distributed throughout the thickness. Both concepts of Eq. 3.9 and Eq. 3.12 are based on the equilibrium of the net forces (which translate the entire beam) and

moments (which bend the beam). Using the assumption that the residual stress and the material properties are uniform through the thickness in each layer, Eq. 3.12 can be reduced to:

$$\kappa = \frac{6m_2n_2(1+m_2)\left(\frac{\sigma_{res,2}}{E_2} - \frac{\sigma_{res,1}}{E_1}\right)}{h_1(1+4m_2n_2+6m_2^2n_2+4m_2^3n_2+m_2^4n_2^2)} \quad (3.13)$$

Although the residual stress in thin films is not uniform (Huang *et al.*, 2006; Huang and Zhang, 2006), the average film (uniform) stresses can still be used to qualitatively determine the curvature of bilayer microcantilever beams using Eq. 3.13.

3.3 Experimental Procedure

The thermal cycling test protocol is designed to carefully study the deformation of the bilayer Si₃N₄/Al microcantilever beams upon release, and during subsequent uniform heating and cooling. The test proceeds as follows: in the first cycle, the microcantilever beams are heated from room temperature to 150 °C at a rate of approximately 200 °C/min. When the temperature of the microcantilever beams approaches the target temperature, the heating rate is decreased to about 10 °C/min, and the temperature slowly approaches the target temperature. The cooling rate from the peak temperature is about the same as the heating rate. During the heating and cooling processes, an interferometer measures the full-

field deformation at temperature intervals of 20 °C. The temperature is held constant for 3 min to maintain equilibrium at each increment. After the first thermal cycle, the microcantilevers are heated and subsequently cooled for four more cycles with 175 °C, 200 °C, 225 °C and 250 °C as the peak temperatures.

3.4 Results

The MEMS-based IR detectors function thermomechanically, and the initial curvature that is observed in the structures of the IR detectors is very similar to the curvature of microcantilever beams that is discussed in this study. Fig. 3.3 shows the schematic of general curvature versus temperature response of microcantilever beams in a thermal cycle. During heating, the curvature increases due to the larger thermal expansion rate in the Al layer relative to the Si₃N₄ layer. The increase in curvature follows a linear thermal elastic loading line, until a critical temperature ($T_{critical}$) is reached. At this critical temperature, the relationship between the curvature and the temperature becomes nonlinear thermal inelastic, and the rates of change in curvature as a function of temperature rapidly decrease. The relatively flat curvature-temperature relationship continues until a maximum temperature (T_{max}) is reached, and cooling of the microcantilever beam is initiated. The cooling response of the beam follows a linear thermal elastic loading line. After the beam reaches room temperature, the curvature of the microcantilever beam is found to be smaller than that prior to the cycle (Gall *et al.*, 2004).

Fig. 3.4 shows the *in situ* measurement of curvature versus temperature for the bilayer Si₃N₄/Al microcantilever beam, including both linear thermal elastic and inelastic regions. Results, measured with the interferometer microscope, show that the as-released microcantilever beams bend up due to the residual strain mismatch in the two layers (Vinci and Vlassak, 1996). In Fig. 3.4, the measured curvature evolution is linearly dependent on the temperature change, from room temperature to 160 °C. This linear dependence indicates a linear thermoelastic deformation of the microcantilever beams in this temperature region. However the full-field deformation measurement cannot be obtained at high temperatures, because the beams curve so much that the reflected light cannot be collected by the objective lens.

In the first cycle, while the temperature is increases towards the peak temperature of 150 °C, the curvature also increases with a constant rate of $d\kappa/dT$. Upon cooling, the sample exhibits a linear thermoelastic mechanical response with $d\kappa/dT$ being approximately equal to the heating response. During the second cycle, the curvature also increases as the temperature is increases. Upon cooling, as $d\kappa/dT$ remains about the same as heating, there is a shift of the linear thermoelastic mechanical behavior. After returning to room temperature, the curvature is reduced from 5.1 mm⁻¹ to 3.2 mm⁻¹, as shown in Fig. 3.4. The deformation behaviors during the following cycles are similar, exhibiting thermoelastic responses upon heating until an inelastic behavior begins. The

cooling process is again thermoelastic with the subsequent curvature at room temperature decreasing after each cycle. Furthermore, after the fourth cycle with a peak temperature of 225 °C, upon return to room temperature, the microcantilever beam bends down toward the substrate, and the curvature is about -0.05 mm^{-1} .

3.5 Discussion

The thermomechanical evolution, including thermal elastic and inelastic regions, and residual strain mismatch-induced curvature are discussed in the following sections.

3.5.1. Thermal Elasticity

When the temperature increases or decreases, the curvature of the beams also increases or decreases, respectively, since the coefficient of thermal expansion (CTE) of Al is higher than that of Si_3N_4 . It is an inherent characteristic of microcantilevers that the misfit strains in the film layers lead to stresses in the layers and deformation of the structure upon changes in temperature. In the thermal elastic region, the curvature slopes during both heating and cooling are approximately the same. The thermomechanical behavior in the thermal elastic region can be predicted by the bilayer bending model (Eq. 3.10). In Fig. 3.4, the average rate of change ($d\kappa/dT$) from 5 cycles is $0.079 \text{ mm}^{-1}/^\circ\text{C}$. This result agrees with the analytical solution of $0.074 \text{ mm}^{-1}/^\circ\text{C}$ obtained by using Eq. 3.10,

and the material properties listed in Table 3.1.

3.5.2. Thermal Inelasticity

The thermal elastic region between room temperature and 160 °C is shown in Fig.3.4. When the temperature continues to rise, a critical temperature is reached, where the curvature changes at a much smaller rate with respect to the change in temperature (dk/dT). This decrease in rate can be attributed to the onset of inelastic deformation (Zhang and Dunn, 2003). Note that this phenomenon is not shown in Fig. 3.4, because the beams curve so much that the reflected light cannot be collected by the objective lens of the interferometer. This inelastic deformation continues until the peak temperature is reached in each cycle. During the inelastic region, the temperature-induced microstructural change in Al occurs as grain growth and other defects are removed, resulting in tensile straining of the Al film (Zhang and Dunn, 2003, 2004; Gall *et al.*, 2004). Once the film reaches the maximum temperature in each cycle, cooling begins, and the curvature decreases linearly again throughout the cooling process. After returning to room temperature, the curvature of the microcantilever beam is found to be smaller than prior cycling. To better understand the deformation in the inelastic region, a previous study on the Au/Si₃N₄ microcantilever beam (Lin *et al.*, 2010) will be used as an example in Chapter 6. In general, the thermomechanical evolution of the Au/Si₃N₄ microcantilever beam during the thermal cycling is very similar to the Si₃N₄/Al microcantilever beam (Fig. 3.4), with

the exception that the inelastic region is apparent. The detail will be discussed in Section 6.4.1.

From a design perspective, the desired curvature of microcantilevers can be achieved by manipulating or adjusting the maximum temperature. Upon repeated cycling, the critical temperature increases so that the curvature maintains thermoelastic behavior for a greater amount of time. Although, once the temperature surpasses the new critical temperature, nonlinear behavior resumes. For repeated cycles that do not pass the critical temperature, thermoelastic behavior occurs throughout the entire cycle. This behavior allows for enhanced reliability during operation, because a predictable curvature is exhibited at expected operating temperatures by using the analytical solution (Eq. 3.10) of thermoelasticity of multilayer beam structures.

3.5.3 Intrinsic Stress Development

From the wafer level residual stress measurement (Section 2.4.3), the residual stress in the as-deposited Al film is -20 MPa. The tensile stress increases in Al film after annealing at different temperature, as shown in Fig 3.5. The residual stress increases to 100 %, 850 % and 1250 % after annealing at temperatures of 100 °C, 200 °C and 300 °C, respectively. The increase in residual stress implies that the annealing process induces additional tensile residual stresses in Al films and activates the microstructural evolution in Al. As shown in the Fig. 3.6, the

grains of the Al film coalesce and increase in overall size. The tensile stress development associated with grain coalescence is discussed in the next paragraph. In comparison however, the residual stress of Si_3N_4 remains approximately constant at 365 MPa after annealing, when temperatures are lower than 400 °C, as shown in the Fig 3.7. The Si_3N_4 film is relatively inactive during low temperature annealing. Similar results can also be found in literature (Yan *et al.*, 2008; Huang *et al.*, 2006; Lin *et al.*, 2009).

The most significant stress-producing process that occurs in thin films involves densification of the film associated with coalescence of isolated clusters. The maximum tensile stress occurs when the film becomes completely continuous (Abermann *et al.*, 1979; Abermann *et al.*, 1978; Janda and Stefan, 1984; Ohring, 2002; Freund and Suresh, 2003; Shackelford and Alexander, 2001). The atomic rearrangement can be responsible for generating tensile stress in grain growth. (Doerner and Nix, 1988). The first involves grain growth, as discussed by Dr. Chaudhari (Chaudhari, 1972). Since the atomic density (atom/volume) within the grain boundaries is less than that in the grain, elimination of grain boundary by grain growth produces a denser material.

We assume the grains in the thin film have an average radius (R) in the as-deposition condition. During the grain growth, the atoms in grain boundary were rearranged into a lattice. The atomic density in grain boundary is lower than that

in the lattice. Thus, the film would shrink in volume during grain growth if it were not attached to the substrate. I defined Δr as the decreased volume per unit area of grain. If the grain boundary were totally eliminated and form a single crystal, the total decreased volume can be express as:

$$\Delta V_{total} = \Delta r(4\pi R^2) \quad (3.14)$$

Transformation strain can be express as (Doerner and Nix, 1988):

$$e_{trans.} = \frac{\Delta V_{total}}{V_{as-deposited}} = \frac{\Delta r(4\pi R^2)}{\frac{4}{3}\pi R^3} = \frac{3\Delta r}{R} \quad (3.15)$$

If the as-deposited thin film has a grain size of R_0 , then the volumetric transformation strain ($e_{trans.}$) associated with the creation of grain boundaries can be expressed as (Doerner and Nix, 1988):

$$e_{trans.} = 3\Delta r\left(\frac{1}{R} - \frac{1}{R_0}\right) \quad (3.16)$$

Any change of grain size produces biaxial stress and strain in the film, because the film is attached to the substrate.

$$\varepsilon_{xx} = \varepsilon_{yy} = -\frac{e_{trans.}}{3} \quad (3.17)$$

Using Hooke's law, the intrinsic biaxial stress in the film associated with grain growth can be expressed as (Doerner and Nix, 1988):

$$\sigma = \sigma_{xx} = \sigma_{yy} = \frac{E}{1-\nu} \left(-\frac{e_{trans.}}{3} \right) = -\frac{E}{1-\nu} \Delta r \left(\frac{1}{R} - \frac{1}{R_0} \right) \quad (3.18)$$

Looking at Eq. 3.18, it is apparent that the tensile stress increases as the grain size increases.

3.5.4. Curvature Control

The as-released Si₃N₄/Al bilayer microcantilever beam bends up due to the residual strain mismatch from the two layers (Fig. 3.8). As mentioned previously, thermal cycling appears to be an effective method to modify the residual strain mismatch-induced curvature. The curvature of the microcantilever beam is found to be smaller after each successive thermal cycle. This technique can be utilized to control the curvature. As explained in Section 3.4.3, the curvature of the microcantilever beam decreases because of the volumetric shrinkage in the Al layer during the thermal inelastic region (Eq. 3.11). In Fig. 3.9, assuming the residual strains in both layers are uniform, the residual strain mismatch between

Si₃N₄ and Al layers is plotted $(\epsilon_{res, Si_3N_4} - \epsilon_{res, Al} = \frac{\sigma_{res, Si_3N_4}}{E_{Si_3N_4}} - \frac{\sigma_{res, Al}}{E_{Al}})$ at room temperature after each thermal cycle, using Eq. 3.11 with material parameters from Table 3.1. The strain mismatch decreases with curvature reduction, and the residual strain is zero when the microcantilever beam is flattened after the fourth thermal cycle. Thermal cycling treatment with optimized peak temperatures can be employed to fully flatten the microcantilevers beams.

3.6 Conclusions

Temperature-dependent deformations, including thermal elasticity and inelasticity, of the Si₃N₄/Al bilayer microcantilever beam are studied via thermal cycling. A thermal system and an interferometer are adopted to monitor the full-field *in situ* curvature change. The bilayer bending model is developed to analyze the thermomechanical response in the thermal elastic region. Thermal cycling reduces the residual strain mismatch by volumetric change in Al during thermal inelastic region. Thus, a flattened bilayer microcantilever beam can be obtained by utilizing the thermal cycling technique with optimized peak temperatures. Compared to other efficient flattening means for microcantilevers, such as ion machining (Bifano *et al.*, 2002) and rapid thermal annealing (Huang *et al.*, 2006), thermal cycling is a nondestructive method and can also provide in-depth understandings on the thermal mechanical evolution of the bilayer

microcantilevers. This technique will be applied to flatten the MEMS-base IR detectors in Chapter 5.

Table 3.1: Material parameters used in the finite element model

	Young's Modulus (GPa)	Poisson's Ratio	CTE (K^{-1})	Thickness (nm)
Si_3N_4	254	0.2	2.1×10^{-6}	200
Al	70	0.3	23×10^{-6}	200

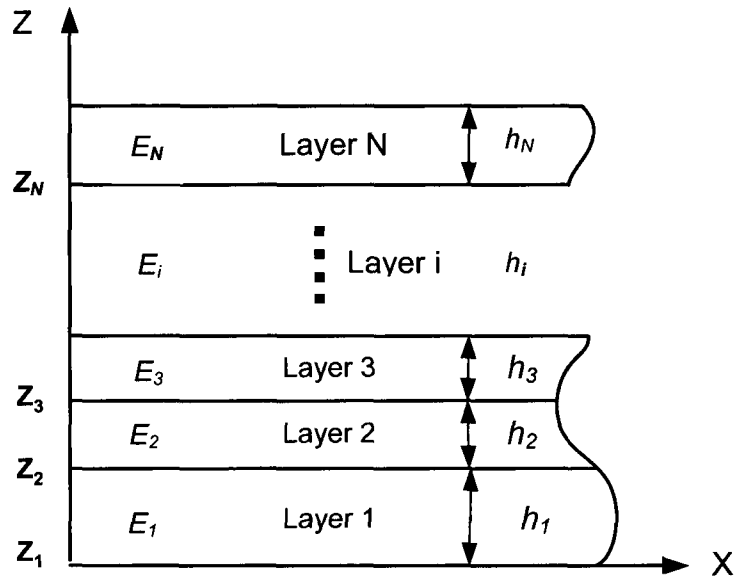


Fig. 3.1: Multilayer structure, where h_i is the thickness of i th layer, $z_i = \sum_{j=1}^{i-1} h_j$ is the bottom position of i th layer ($Z_1=0$ is the first layer).

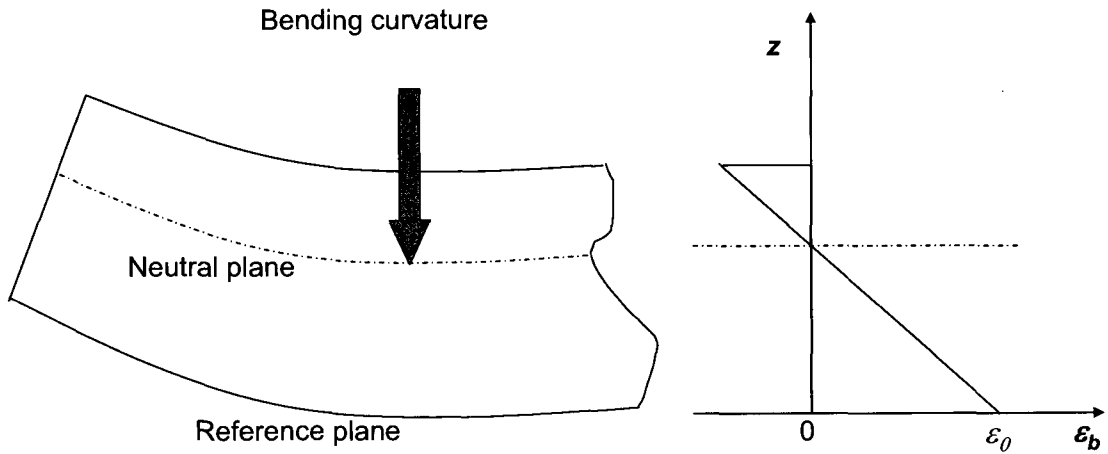


Fig. 3.2: The reference plane is chosen at $z=0$. The neutral plane is defined as the plane where the bending strain ϵ_b is zero.

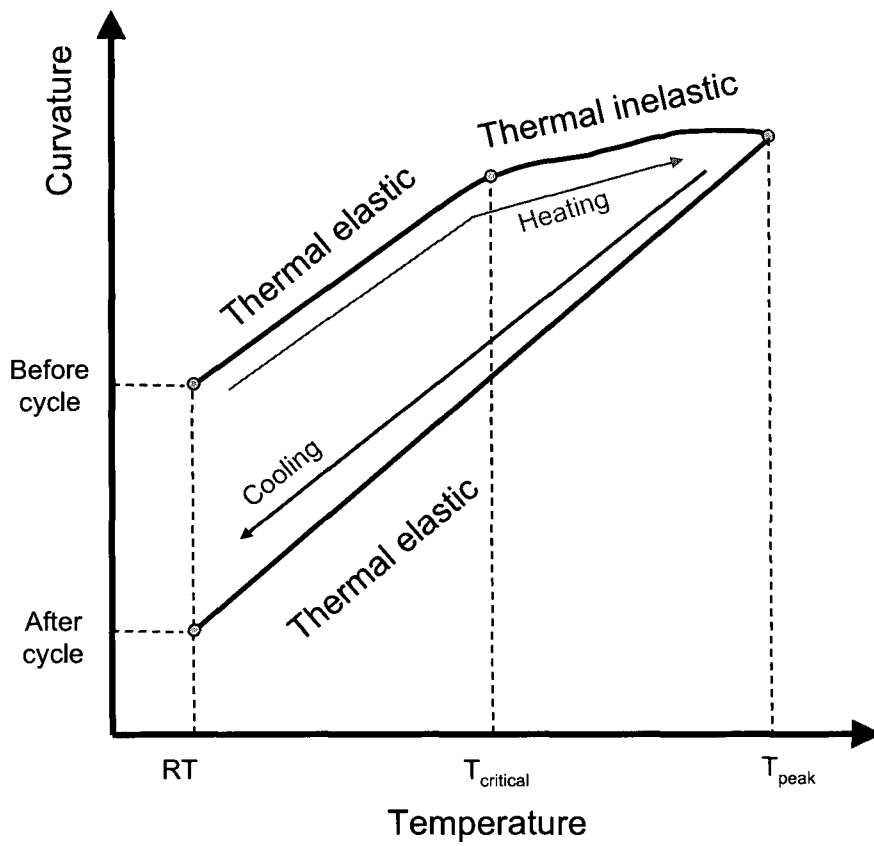


Fig. 3.3: Schematic illustrating the general curvature versus temperature response of a Si_3N_4/Al bilayer microcantilever beam in a thermal cycle.

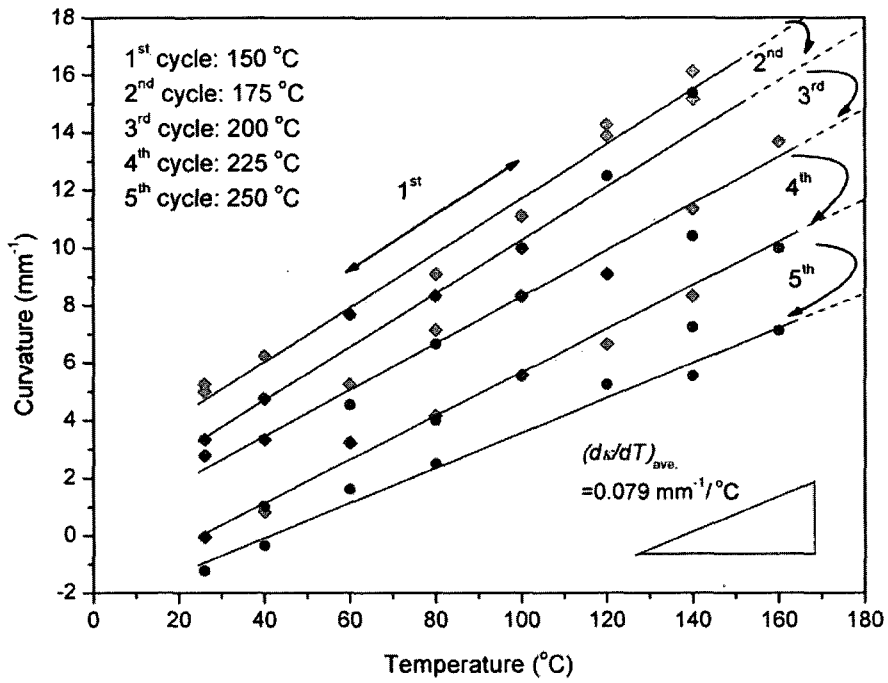


Fig. 3.4: Curvature versus temperature for bilayer Si_3N_4 (200 nm)/Al (200 nm) microcantilever beams during the five thermal cycles with different peak temperatures. The diamond and circle symbols are measured curvatures during the heating and cooling processes in each cycle, respectively.

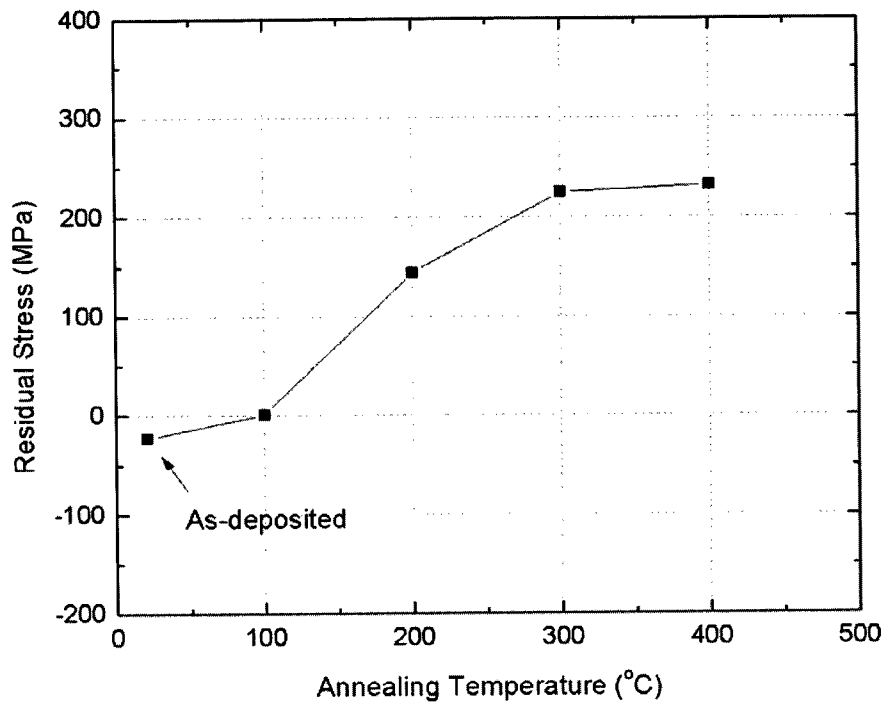


Fig. 3.5: Residual stress evolution of Al film after various annealing temperature.

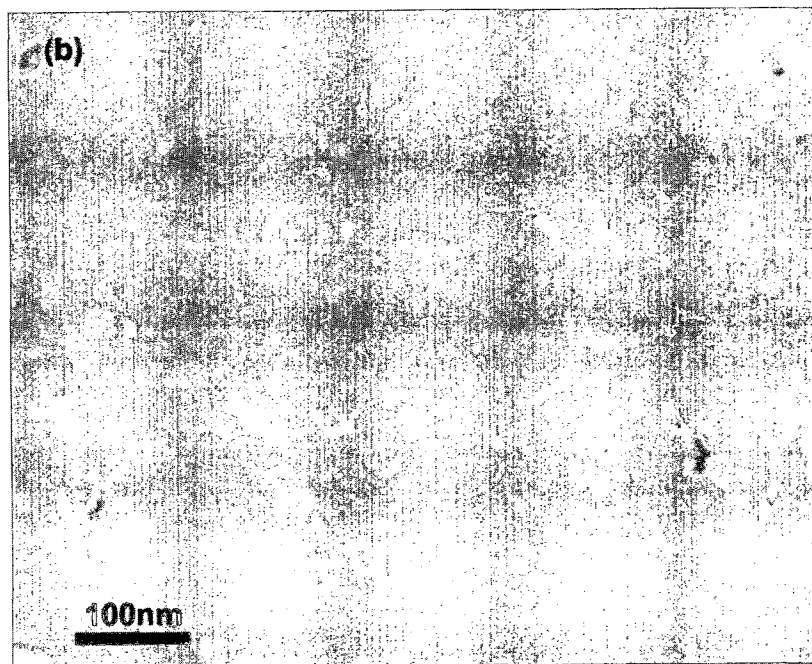
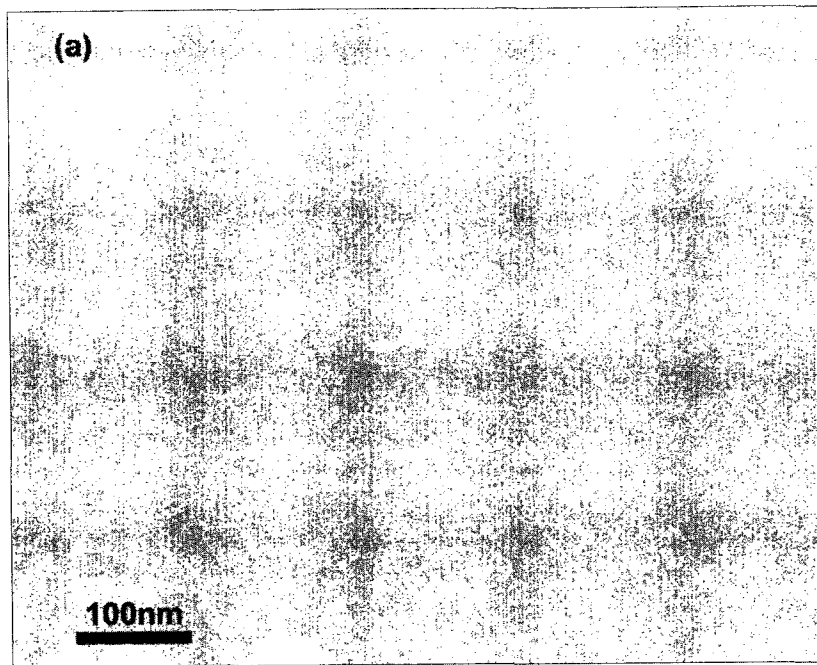


Fig. 3.6: SEM & AFM image of Al grains (a) before and (b) after 225 °C annealing.

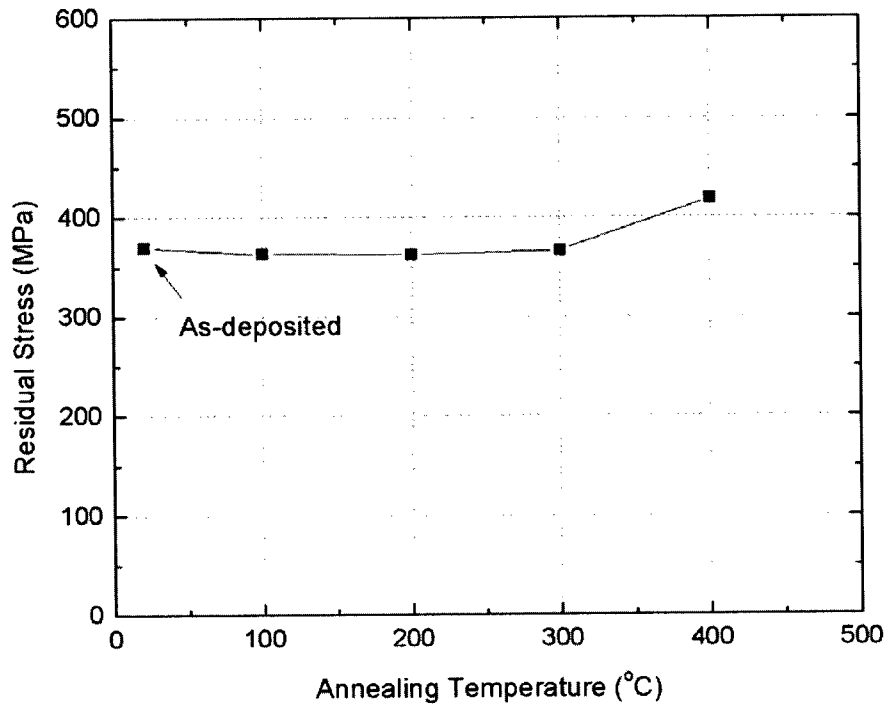


Fig. 3.7: Residual stress evolution of Si_3N_4 film after various annealing temperatures.

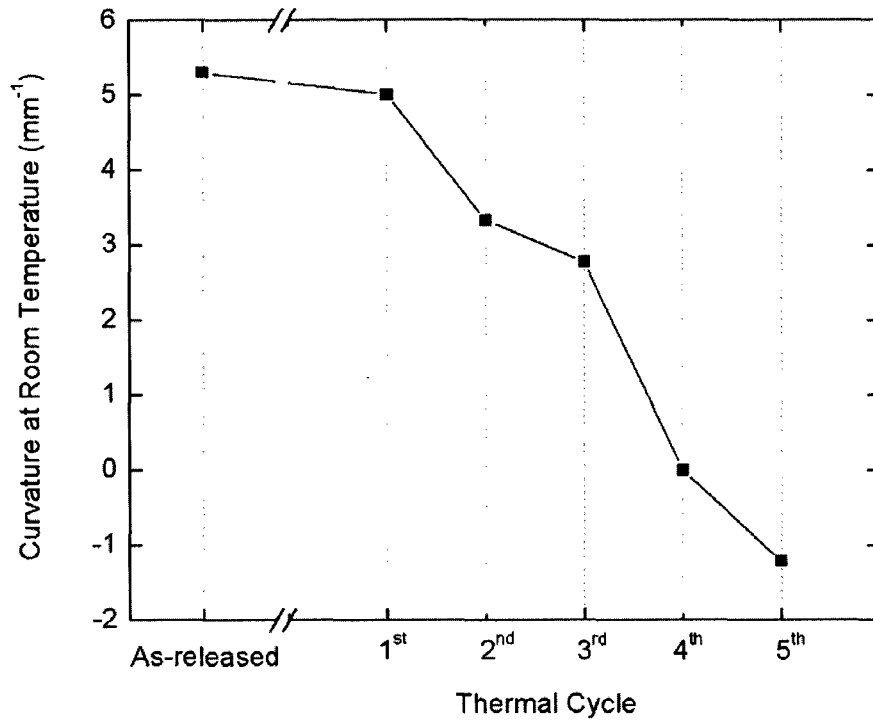


Fig. 3.8: Measured room temperature curvature after each thermal cycle from Fig. 3.5. The peak temperatures of the 1st, 2nd, 3rd, 4th, and 5th cycles are 150 °C, 175 °C, 200 °C, 225 °C, and 250 °C, respectively.

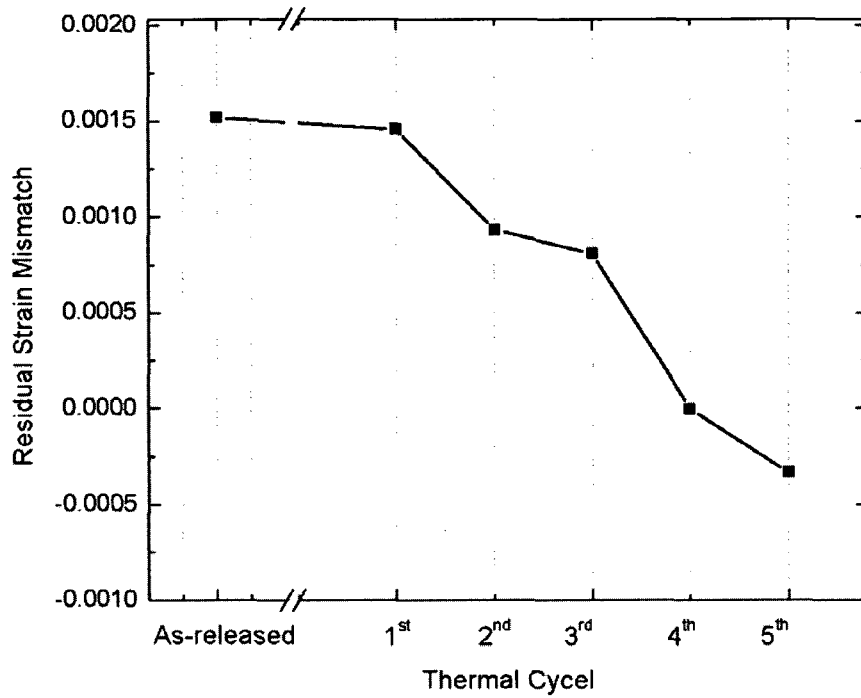


Fig. 3.9: Uniform residual strain mismatch after each thermal cycle from Fig. 3.9. The peak temperatures of 1st, 2nd, 3rd, 4th, and 5th cycles are 150 °C, 175 °C, 200 °C, 225 °C, and 250 °C, respectively.

CHAPTER 4: TIME-DEPENDENT DEFORMATION OF BILAYER MICROCANTILEVER BEAMS

4.1. Introduction

In MEMS devices, where many components are constantly in motion, it is crucial to accurately control the deformation over a significant period of time, in order to meet performance and reliability requirements (Miller *et al.*, 2001; Zhang *et al.*, 2004; Zhang and Dunn, 2004; Lee *et al.*, 2000; Vickers-Kirby *et al.*, 2000; Gall *et al.*, 2004). As materials used in MEMS devices move beyond conventional Si to include metals, this task becomes even more important. Creep, the tendency of a material to deform permanently, is of special concern. In bilayer microcantilever-based devices, a ceramic/metal bilayer acts as a sensor or actuator for various applications. However, the metal layers are generally unstable after deposition (Dunn *et al.*, 2002; Zhang and Dunn, 2003, 2009). When the metals are subjected to thermal loading, especially isothermal holding, the microstructural evolution in metal layers can be triggered, such as the extinction of excess vacancies, subgrain coalescence and grain boundary diffusion (Miller *et al.*, 2005, 2007a, b; Zhang and Dunn, 2004; Gall *et al.*, 2004). The microstructural evolution results in creep behavior in the metal layers, which result in highly time-dependent deformation in bilayer microcantilevers. Neglecting the inelastic deformation can result in misinterpretations of the measurement data from bilayer microcantilever-based sensors and can compromise control precision of

actuators. Hence, it is of vital importance to perform accurate thermomechanical behavioral characterization on bilayer microcantilevers and to develop an appropriate model for the description of its time-dependent inelastic deformation, in order to better design, characterize, and manufacture successful MEMS structures and devices for the next generation.

In order to address the aforementioned issues, $\text{Si}_3\text{N}_4/\text{Al}$ microcantilever beams are used to explore the combined effects of geometric and material nonlinearity. In this chapter, the time-dependent deformation of bilayer microcantilever beams is characterized by using an isothermal holding test, as well as finite element analysis (FEA). A generalized Power-law creep model with the use of one exponential term is used to emulate the thermomechanical behavior of bilayer microcantilever beams at different temperatures. After the appropriate Power-law creep model of bilayer microcantilever beams is determined, it is used to develop an FEA model for predicting and simulating creep behavior on bilayer microcantilevers during long-term operation.

A research flow chart of this work is shown in Fig. 4.1. Section 4.3 covers how the thermomechanical characterization of the bilayer microcantilever is probed using the isothermal holding test. The results are inputted into a developed FEA model and then validated on the $\text{Si}_3\text{N}_4/\text{Al}$ bilayer microcantilever beam with different holding temperatures, the process of which is explained in Section 4.4.

The validated viscoelastic FEA model is utilized to analyze the thermomechanical behavior of MEMS-based IR detectors and is compared with experimental results in Chapter 5. This chapter discusses a balance between experimental characterization of the bilayer microcantilevers and the development of an FEA model for predicting the time-dependent inelastic deformation of those microcantilevers.

4.2. Theoretical Background

Materials are often placed in service at elevated temperature and exposed to static mechanical stresses. Deformation under such circumstances is termed creep. Defined as the time-dependent and permanent deformation of materials when subjected to a constant loading, creep is normally an undesirable phenomenon and is often the limiting factor in the lifetime of a part (Callister and Rethwisch, 2010).

This empirical relationship, Power-law creep model, is applicable for any nonlinear deformation on solids as long as an appropriate number of terms are used. The Power-law can be expressed as (Zhang *et al.*, 2004; Zhang and Dunn, 2004; Keller *et al.*, 1999; Shen and Suresh, 1995; Chen *et al.*, 2008; Chen and Hsu, 2007; Callister and Rethwisch, 2010)

$$\dot{\varepsilon} = A\sigma^n \quad (4.1)$$

where A and n are material constants. When the influence of temperature is included,

$$\dot{\varepsilon} = Ce^{\frac{-Q}{kT}} \sigma^n \quad (4.2)$$

where $\dot{\varepsilon}$ is the strain rate, C is the creep constant dependent on the material and the particular creep mechanism, k is the Boltzmann constant ($8.314 \text{ Jmol}^{-1}\text{K}^{-1}$), n is the stress exponent, Q is the activation energy for creep and T is the absolute temperature. In order to predict the creep behavior, Q , n and C must be determined experimentally.

4.3. Thermomechanical Characterization

The thermomechanical behavior of the bilayer microcantilever is characterized by isothermal holding tests. The overall thermal loading profile within the heating and cooling stage for thermomechanical characterization is shown in the Fig. 4.2. The goal of these characterizations is to establish a Power-law creep model for Al. The standard procedures will generate more credible data, which is important for the subsequent FEA model development.

4.3.1. Pre-cycling

First, the microcantilever beams are thermal cycled three times between room temperature and 225 °C, to not only flatten the microcantilever beams, but also stabilize the Al microstructure. In the first cycle, the microcantilever beams are heated to 225 °C and then cooled back to room temperature. The curvature is about 0 mm^{-1} at room temperature after the first cycle. This phenomenon is similar to the experimental data of thermal cycling as shown in Fig. 3.4. In the second and third cycles, the microcantilever beams deform thermoelastically over nearly the entire cycles and do not show significant inelastic deformation.

4.3.2. Isothermal Holding

After the initial three thermal cycles, the microcantilever beams are held at the isothermal holding temperature for about 45 hours. In order to study the effects of creep and stress relaxation at different holding temperatures (100 °C, 125 °C and 150 °C), the deformation of the microcantilevers is measured as a function of time. Meanwhile, the full-field out of plane deformations (x,y) are measured by an interferometer (Section 2.3) during the initial three thermal cycles and the isothermal holding period. From the measured full-field out of plane deformation, the average curvatures are calculated over a region about 50 μm from anchor. Fig. 4.3 shows the curvature evolution as a function of temperature between room temperature and 125 °C for $\text{Si}_3\text{N}_4/\text{Al}$ bilayer microcantilever beams during the heating, holding and cooling process. The response shows the three regions

of deformation: (i) during the heating process, the temperature is increased with a constant rate of $d\kappa/dT$ from room temperature to 125 °C, and then held for about 45 hours; (ii) during the 45 hours of isothermal holding, the deformation is inelastic due to the combined effect of creep and stress relaxation; (iii) upon cooling from 125 °C, the deformation is again thermoelastic with the same $d\kappa/dT$ as the first deformation region. When the temperature reaches room temperature, the curvature is lower than the initial curvature at room temperature, due to the inelastic deformation during isothermal holding.

Fig. 4.4 shows the experimental data of curvature decreases as time elapses during isothermal holding at temperatures of 100 °C, 150 °C, 200 °C for bilayer Si₃N₄/Al microcantilever beams. The rate of decrease of the curvature is rapid over the first 25 hours, and the rate of curvature drop is higher for the microcantilever beams held at higher temperatures. Using Eq. 4.3, a graph of the normalized curvature ($k_{normalized}$) evolution is shown in Fig. 4.5.

$$k_{normalized} = \frac{k(t) - k_{initial}}{k_{initial}} \times 100\% \quad (4.3)$$

where $k_{initial}$ is the curvature at $t=0$. After the isothermal holding at temperatures of 100 °C, 125 °C and 150°C, the curvature decreases by 6 %, 22 % and 56 %, respectively. During isothermal holding, the Si₃N₄ is relatively stable with inelastic

deformation, due to its relatively higher melting temperature (1900 °C) and creep resistance when compared to metals (Zhang and Dunn, 2004; Gall *et al.*, 2004). Hence, the inelastic deformation of the microcantilever beams is most likely caused by the strains in the Al layer. An FEA model is also established, and in conjunction with the test data used extracts the Power-law creep of Al, which is discussed in the following section.

4.4. FEA Model Development

The thermomechanical behavior characterization during isothermal holding in Section 4.3 only provides information on the properties of inelastic deformation of Si₃N₄/Al microcantilevers, namely the reaction deformation and applied temperature. This information can only be treated as the response of the structure. During isothermal holding, the Si₃N₄ is assumed to be relatively stable due to its higher melting temperature (1900 °C) and creep resistance when compared to Al (Zhang and Dunn, 2004; Gall *et al.*, 2004). Hence, assuming that the Si₃N₄ deforms elastically and the inelastic deformation mechanism is described by Power-law creep in Al layer, the inelastic deformation during isothermal holding can be modeled and represented by using curvature evolution as a function of time. In order to find the Power-law creep of Al (Eq. 4.1), an FEA must be conducted (Keller *et al.*, 1999; Shen and Suresh, 1995; Chen *et al.*, 2008). In particular, the FEA is used to find the creep parameters (A and n) of the Power-law creep in an Al layer. By using the controlled inputs applied during the

experiments, the analysis aims to fit the experimental response data by tuning the parameters of the adapted Power-law creep in the associated FEA.

The commercial finite element package ABAQUS v.6.7 is used to perform the analysis (Hibbit, 1998). An FEA model with the same geometry as the specimens is constructed. The initial condition of this model does not consider any residual stress in the layers. The bilayer microcantilever beam is meshed with four-node composite shell elements (S4R), to approximate the thin-plate kinematics of the Kirchoff theory (Hibbit, 1998). The model consists of 1800 S4R composite shell elements. Each node has three displacement and three rotation degrees of freedom; each of the six degrees of freedom uses an independent bilinear interpolation function. The S4R elements allow transverse shear deformation. These elements use thick shell theory as the shell thickness increases and become discrete Kirchhoff thin shell elements as the thickness decreases; the transverse shear deformation becomes very small as the shell thickness decreases (Hibbit, 1998). Such a mesh is shown in Fig. 4.6. The input material properties of the finite element model are shown in Table 3.1. The boundary conditions fix all of the freedom at one of the two ends, and the parameters of the geometry conform to the real structures. When subjected to a uniform temperature change, mismatch strain is induced in the bilayer microcantilever beam due to the thermal expansion mismatch between Al and Si_3N_4 . This mismatch strain will then result in bending curvature of the bilayer microcantilever

beam. From the convergence study shown in Fig. 4.7, the percent error of the FEA results from different element numbers as compared with 20×90 elements can be expressed as:

$$Error(\%) = \frac{FEA_{a \times b} - FEA_{20 \times 90}}{FEA_{20 \times 90}} \times 100\% \quad (4.4)$$

When the mesh contains more than 1800 elements (i.e. 20×90) the error of FEA results between different mesh is smaller than 0.13 %. Hence, the FEA model with 1800 elements (i.e. 20×90) in the simulation provides a converged result. For the parameters used in this study, the number of elements is found to be adequate to obtain reasonably accurate results.

By applying uniform temperatures of 100 °C, 125 °C and 150°C for 45 hours and recording the deformation of microcantilever beams, the simulation data can be obtained. The fitting between the experimental data and the associated simulation can be achieved by varying the parameters incorporated into the model. By using the Power-law creep approach, the creep behavior of Al at various holding temperatures can be modeled, as listed in Table 4.1. The results indicate that the simulation results essentially agree with the test data as shown in Fig. 4.4 and Fig. 4.5.

4.5. Discussion

4.5.1. Creep Behavior

With a constant n of 5.3 and differing A values ($A=9\times 10^{-15} \text{ h}^{-1}\text{MPa}^{-5.3}$, $3\times 10^{-14} \text{ h}^{-1}\text{MPa}^{-5.3}$, and $1.5\times 10^{-12} \text{ h}^{-1}\text{MPa}^{-5.3}$ for 100 °C, 125 °C and 150 °C), the inelastic behavior during isothermal holding are well described by FEA model. However, these Power-law creeps can only be used to describe the inelastic behavior at particular temperatures. In order to obtain a more general Power-law creep of Al, the temperature influence has to be included using Eq. 4.2. From Eq. 4.2, the material constant A can be extended as $Ce^{\frac{-Q}{kT}}\sigma^n$. By taking the logarithm of A , this relationship can be rewritten as:

$$\ln(A) = \ln(C) + \frac{-Q}{k} \times \frac{1}{T} \quad (4.5)$$

Using Eq. 4.3 in conjunction with data from Table 4.1, the relationship between $\ln(A)$ and $1/T$ is calculated and shown in Fig. 4.8. The slope and the intercept, corresponding to $(-Q/k)$ and $\ln(C)$, are 16055.86 and 10.50. Note that k is the Boltzmann constant of $8.31 \text{ Jmol}^{-1}\text{K}^{-1}$. The activation energy (Q) and creep constant (C) are calculated as $1.3\times 10^2 \text{ kJmol}^{-1}$ and 3.6×10^4 . Therefore Power-law creep for Al for various temperatures can be expressed as:

$$\dot{\epsilon} = 3.6 \times 10^4 e^{\frac{-1.3 \times 10^2}{T}} \sigma^{5.3} \quad (4.6)$$

where the following units are used: strain rate ($\dot{\epsilon}$) is 1/h, stress (σ) is MPa, and temperature (T) is K. After obtaining the creep model, two additional tests (at 110 °C and 140 °C isothermal holding) are also performed using different holding temperatures in order to evaluate the reliability of the model. Fig. 4.9 shows the experimental data and the predicted results using Eq. 4.6; and it can be seen that the prediction agrees well.

4.5.2. Stress Evolution

To better understand the microstructure evolution during isothermal holding, the stress through the thickness of the bilayer microcantilever beams is shown in Fig. 4.10 for times of 0, 5, 10, 25 and 45 hours. The stress plotted is taken at the center of the beam from the FEM results. In Fig. 4.10, the thickness is from 0 μm to 0.2 μm in the Al layer, and is from 0.2 μm to 0.4 μm in the Si_3N_4 layer. At a time of 0 hours, the stress gradient exists across both the Al and the Si_3N_4 layers. During the first 5 hours of isothermal holding, the stresses in both the Al and the Si_3N_4 layers decrease and redistribute significantly. After 25 hours of isothermal holding, the stresses distribute almost evenly throughout the thickness of the Al layer and change slowly for the rest of the holding period. Fig. 4.10 demonstrates

that isothermal holding conducted at higher temperature results in more compressive stress relief. These results on the evolution of stress distribution help to better illustrate the combined effect of creep and stress relaxation during isothermal holding.

4.6. Conclusions

In this chapter, a thermal system and an interferometer are used to *in situ* measure the full-field out-of-plane deformation of Si₃N₄/Al bilayer microcantilever beams. The deformation mechanisms with isothermal holding are studied. The creep and stress relaxation combined behavior of microcantilever beams during isothermal holding are characterized. The characterized creep behavior of Al is inputted into an FEM model in order to predict the curvature evolution in long-term operation.

The contribution of this chapter includes integrating the results from recent research and using sophisticated mechanics to form a comprehensive methodology for the creep characterization, modeling, and analysis of bilayer microcantilevers during long-term operation. The results presented in this chapter are useful for the fundamental understanding of many similar bilayer microcantilever-based MEMS devices. The discussion in this chapter can also help to identify more effective means for engaging the materials science and engineering mechanics disciplines in various research areas to continue

advances in MEMS technology.

Table 4.1: Material constants, A and n , of Power law creep at different holding temperature.

Holding Temperature (°C)	n	A (h ⁻¹ MPa ^{-5.3})
100	5.3	9×10^{-15}
125	5.3	7×10^{-14}
150	5.3	1.5×10^{-12}

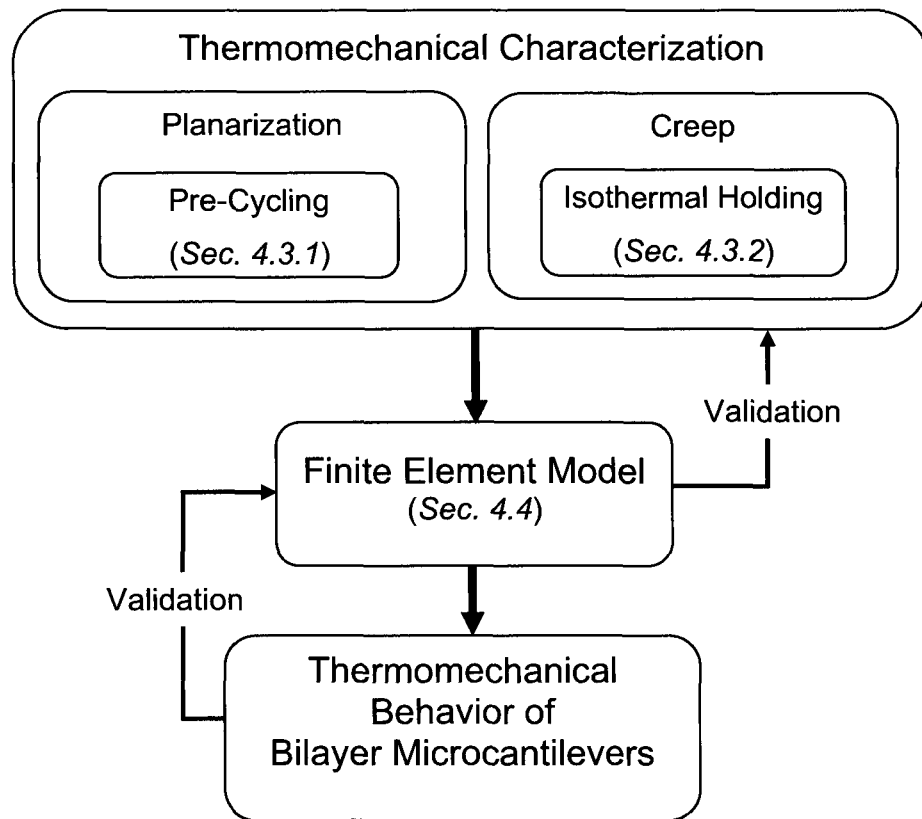


Fig. 4.1: Overall research structure and process of Chapter 4.

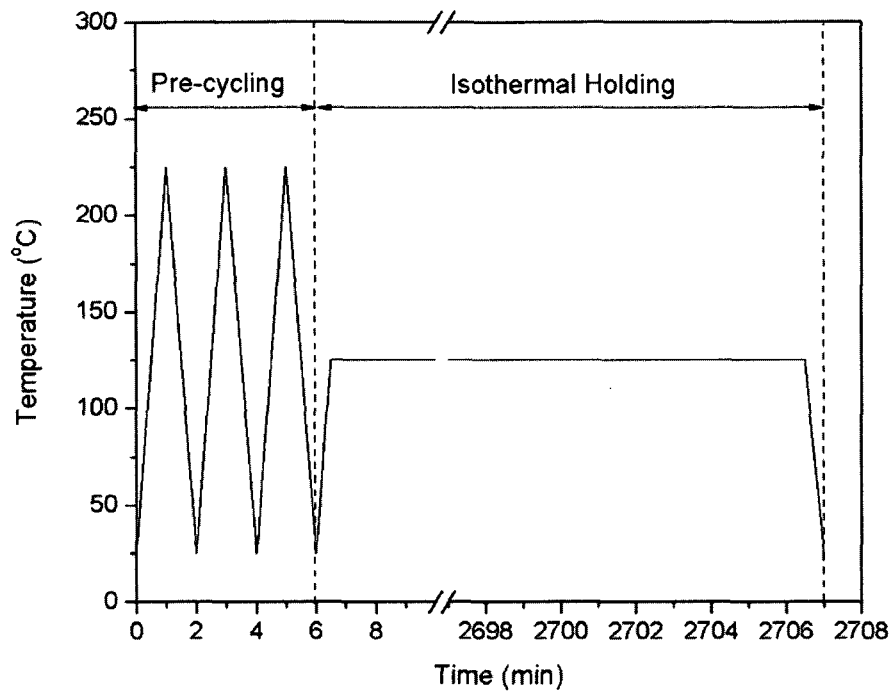


Fig. 4.2: Schematic of thermal loading profile within the heating/cooling stage for thermomechanical characterization.

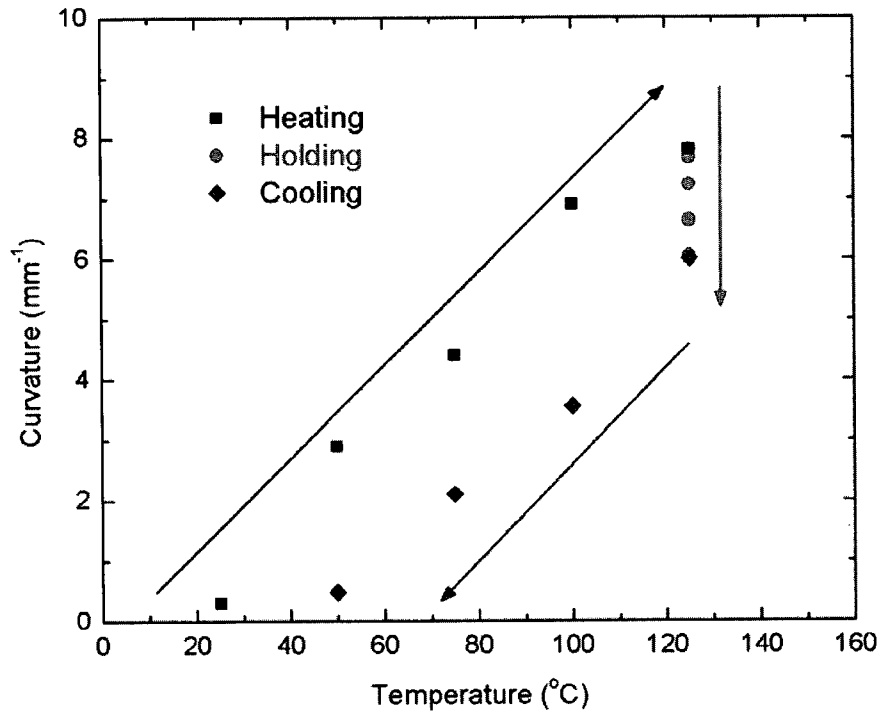


Fig. 4.3: Curvature evolution during the heating, isothermal holding and subsequent cooling to room temperature.

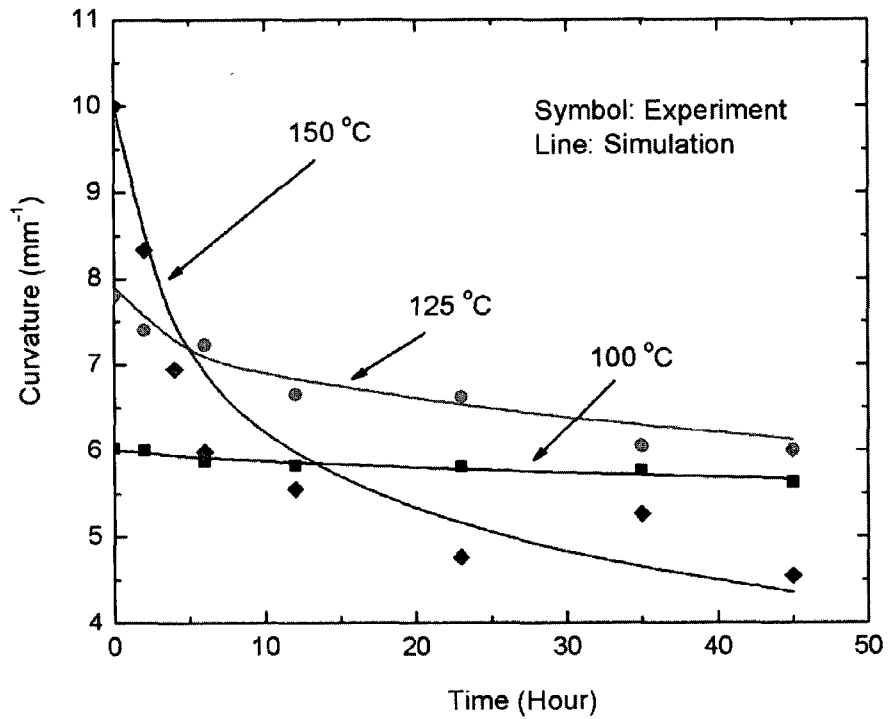


Fig. 4.4: Measured curvature evolution during the 45 hour isothermal holding periods at temperatures of 100 °C, 125 °C and 150°C for Si₃N₄/Al bilayer microcantilever beams. The symbols represent experimental data, while the solid lines represent simulation results.

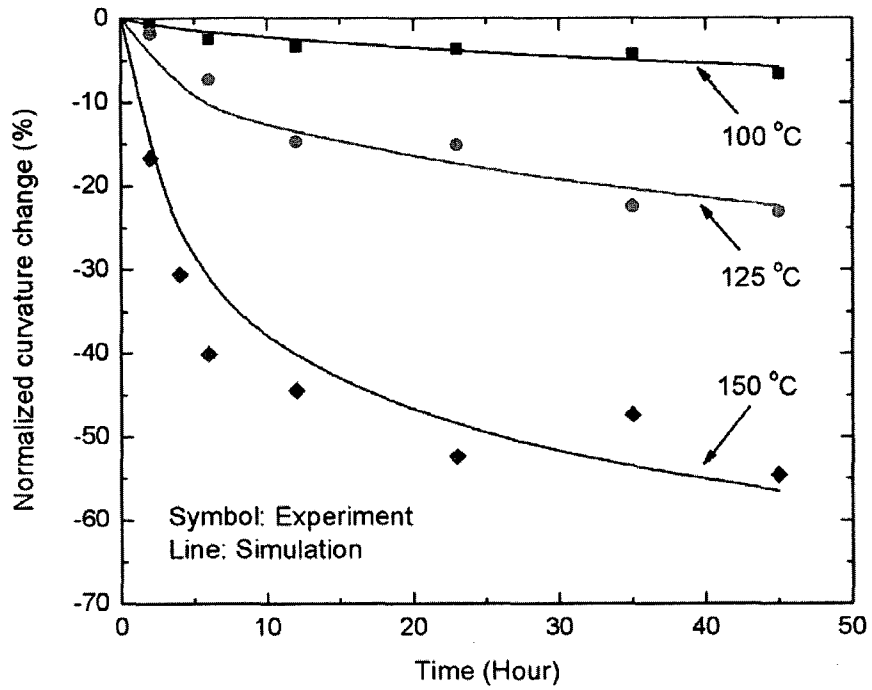


Fig. 4.5: Normalized curvature evolution during the 45 hour isothermal holding at temperatures of 100 °C, 125 °C and 150°C for Si₃N₄/Al bilayer microcantilever beams. The symbols represent experimental data, while the solid lines represent simulation results.

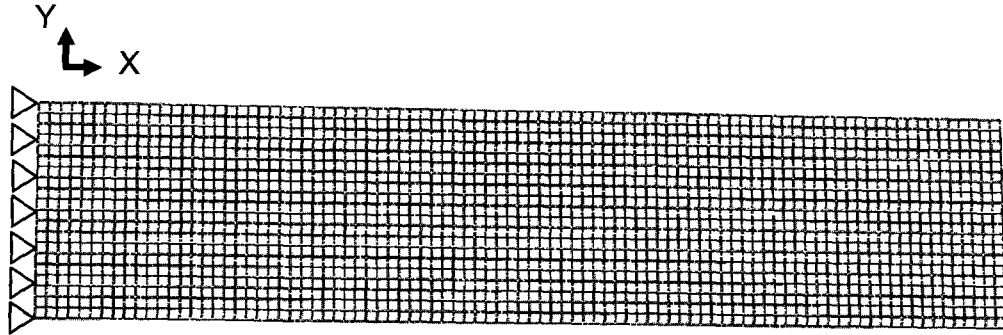


Fig. 4.6: The bilayer microcantilever beam is meshed by S4R elements. The finite element model contains 1800 elements.

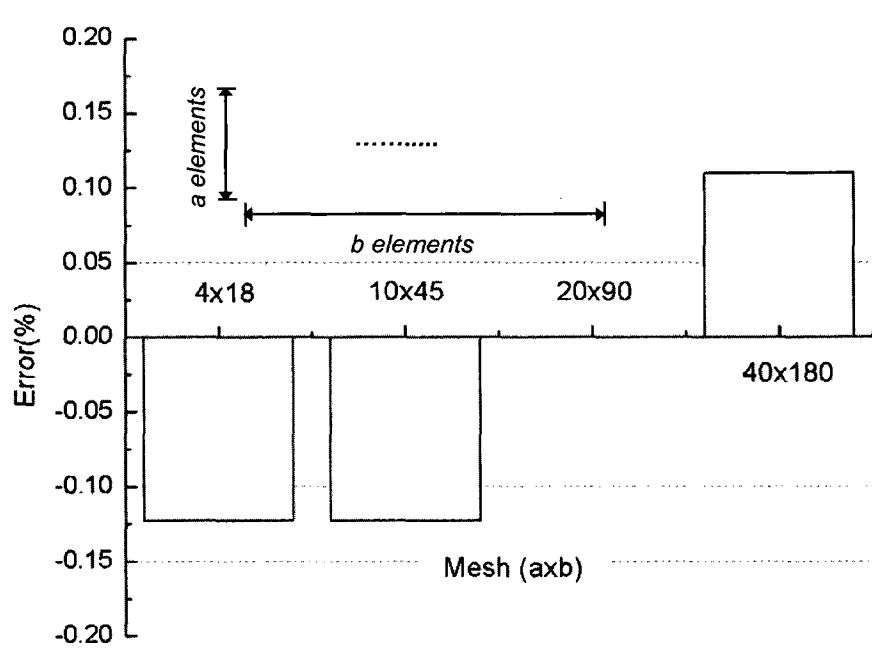


Fig. 4.7: Convergence study of thermomechanical behavior simulation

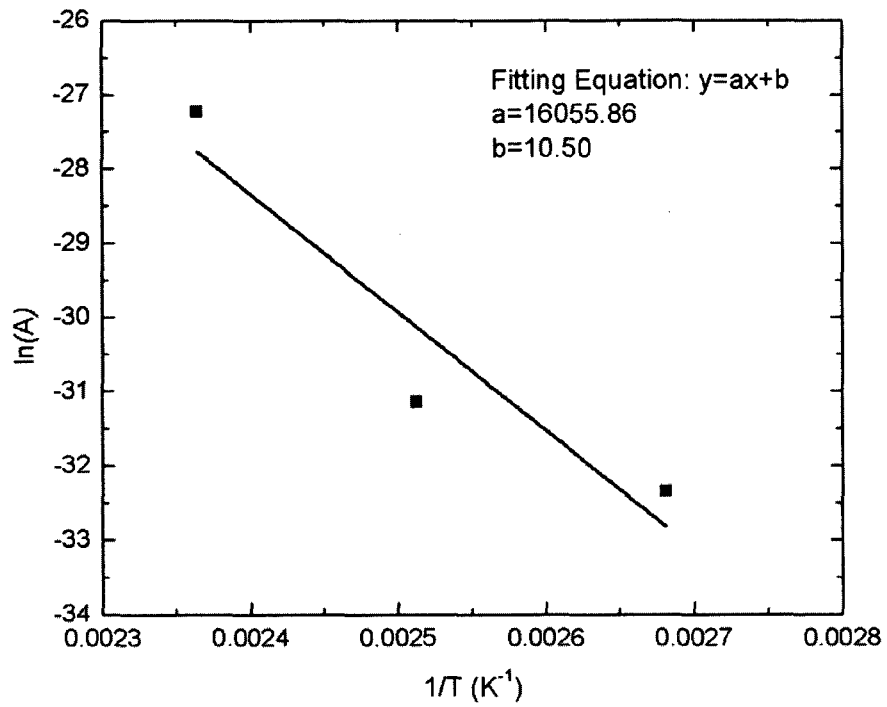


Fig. 4.8: Creep data reduction. Material constant (A) of Power-law creep as a function of $1/T$, where T is the test temperature.

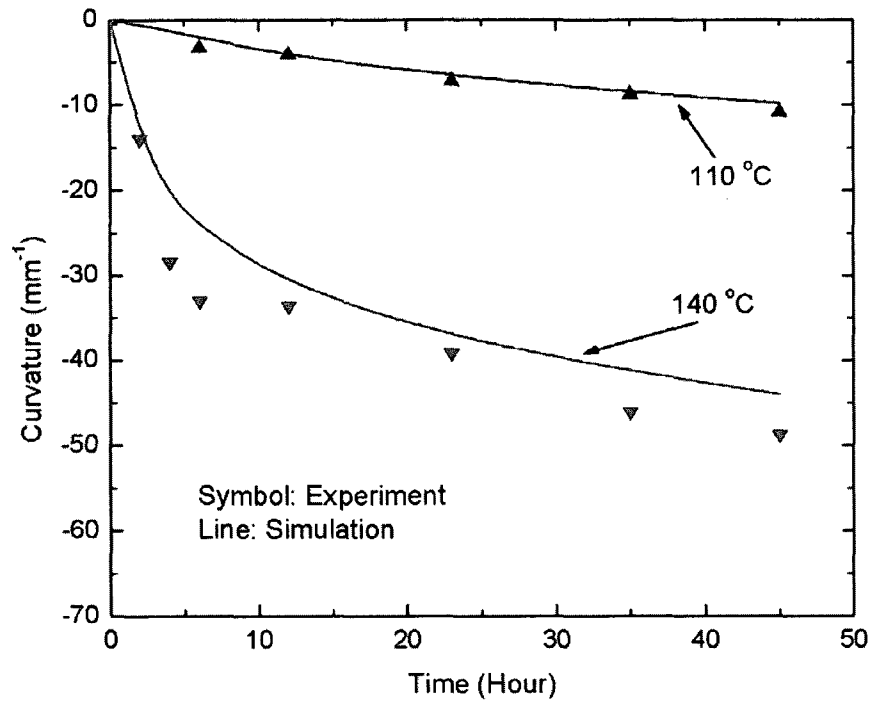
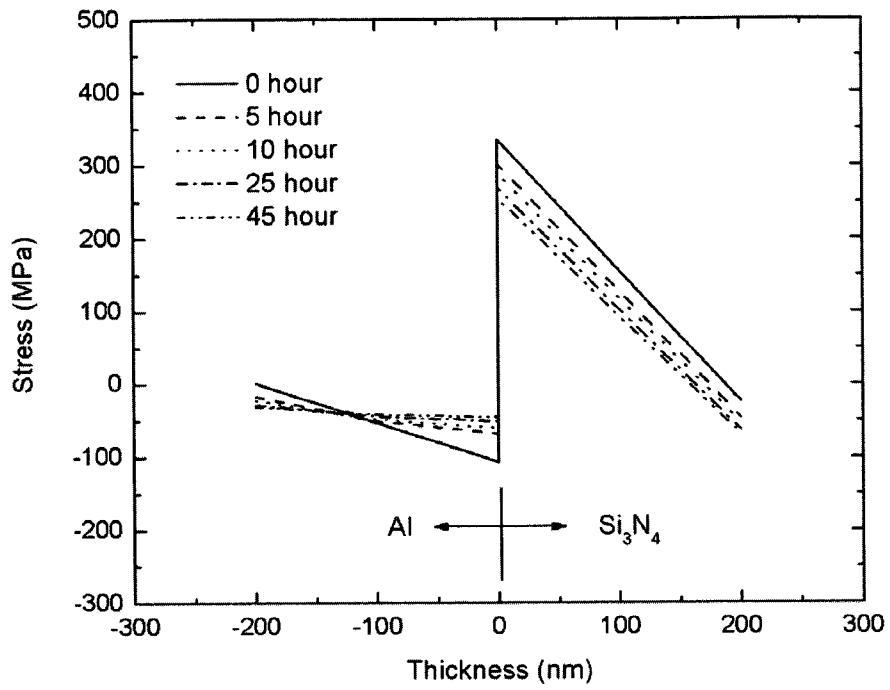
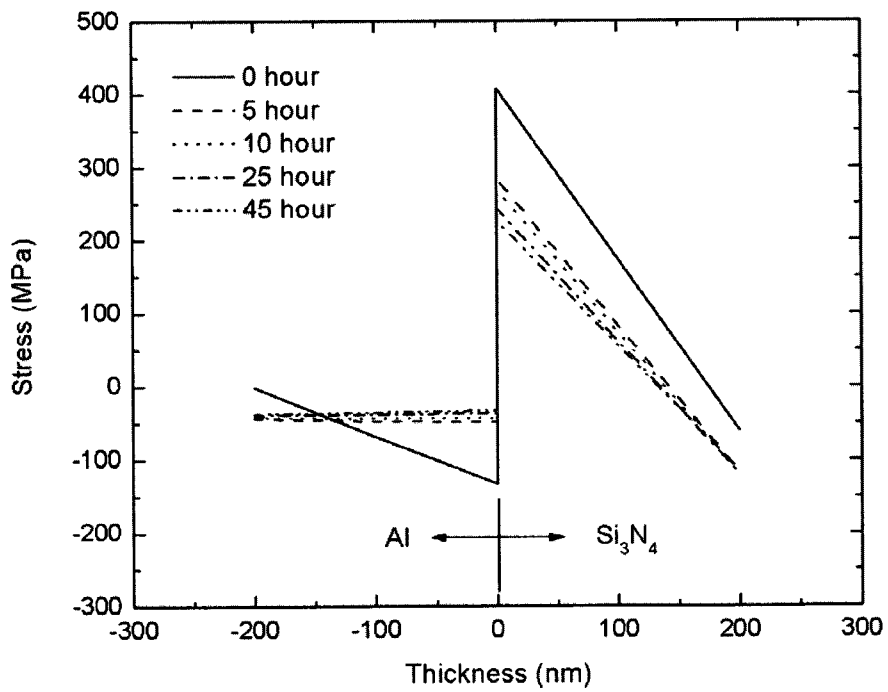


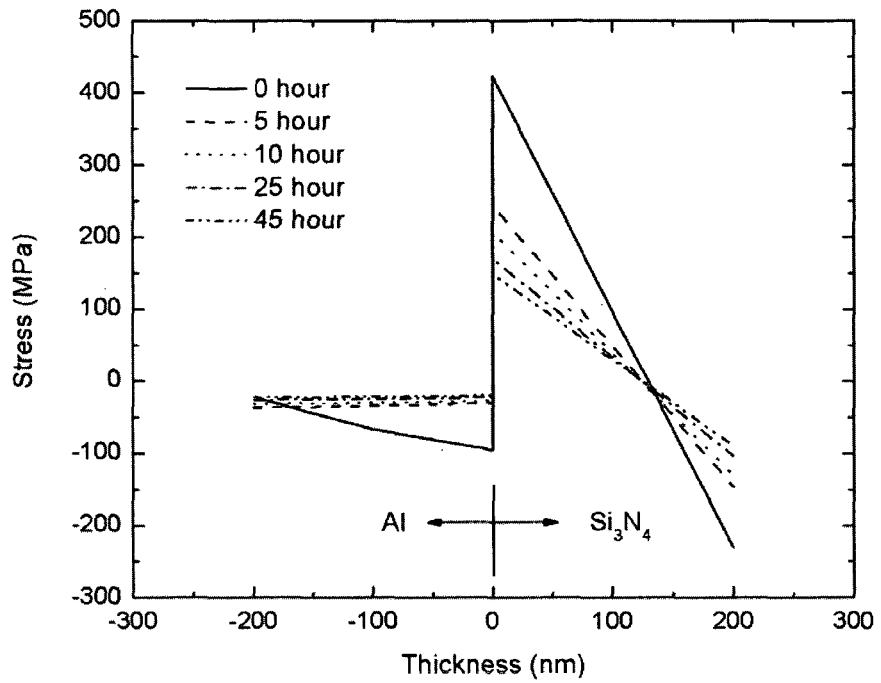
Fig. 4.9: The comparison between the additional experimental data and the Power-law creep prediction.



(a)



(b)



(c)

Fig. 4.10: Stress distributions in both the Al and the Si₃N₄ layers of bilayer microcantilever beams at times of 0, 5, 10, 25, and 45 hours of isothermal holding at temperatures of (a) 100 °C, (b) 125 °C and (c) 150 °C.

CHAPTER 5: THERMOMECHANICAL BEHAVIOR OF MEMS-BASED IR DETECTORS

5.1. Introduction

Over the past decade, MEMS technologies have given rise to bimaterial microcantilever-based IR detectors. These detectors can achieve a theoretical noise-equivalent temperature difference (NETD) of below 5 mk (Amantea *et al.*, 1998; Amantea *et al.*, 1997; Zhao *et al.*, 2002). This type of IR detector is based on the bending of bilayer microcantilevers upon absorption of infrared radiation. The subsequent deformation can be readily determined by using piezoresistive, optical, or capacitive methods (Amantea *et al.*, 1998; Amantea *et al.*, 1997; Zhao *et al.*, 2002). Four primary components make up the typical design of MEMS-based IR detectors (Fig. 5.1): 1) IR absorber and sensing plate, 2) actuation legs, 3) thermal isolator and 4) bottom electrode. One component is an IR absorber and sensing bimaterial plate. This bimaterial plate consists of a Si_3N_4 top layer that absorbs IR radiation and converts it to heat; an Al metal layer on the bottom serves as a sensing component for the capacitance read-out. In this design, an Al layer is used as a top electrode. Together, with a bottom titanium (Ti) electrode located underneath the plate, these two form a capacitor. The actuation legs convert heat from the absorber to mechanical deformation. Finally, a thermal isolator minimizes the amount of heat conducted to the substrate. This device is based on the conversion of absorbed IR energy to a measured change in

capacitance. When the sensing bimaterial plate transfers infrared radiation to heat as a change in temperature, the plate deforms due to the mismatch in their coefficient of thermal expansion (CTE) mismatch. As a result, the capacitance between the bilayer plate and the bottom electrode changes. The bilayer actuation legs also bend, since the heat from the sensing plate is conducted to the legs (Amantea *et al.*, 1998; Amantea *et al.*, 1997; Datskos *et al.*, 2004; Hunter *et al.*, 2006; Zhao *et al.*, 2002; Huang *et al.*, 2008; Li, 2004; Lin *et al.*, 2008).

As mentioned in Chapter 3, the bimaterial sensing plate and actuation legs curve significantly after release from a sacrificial layer, largely due to the mismatch of residual stress/strain in the two materials (Fig. 5.1) (Vinci and Vlassak, 1996). The curved structures greatly compromise the performance and functionality of the device. Therefore, curvature modification is one of the important topics in the post-process assessment of MEMS-based IR detectors (Bifano *et al.*, 2002; Huang *et al.*, 2006; Vinci and Vlassak, 1996). In Chapter 3, the analysis of the thermoelastic response of bilayer microcantilever beam has been presented. However, in the designs of MEMS-based IR detectors, the bimaterial sensing plate structure is supported by a deformable boundary. The deformation of the sensing plate greatly complicates the analysis and compromises the device performance (Chu *et al.*, 1993; Huang, 2007; Li, 2004; Zhao *et al.*, 2002). Therefore, it is crucial to fully understand and establish a model to predict the

thermoelastic response of the MEMS-based IR detector, thereby facilitating the design of a device that adequately estimates the performance.

As mentioned in Chapter 4, it is important to understand the deformation of bilayer microcantilever beams over a significant period of operation time, in order to meet performance and reliability requirements. Time-dependent deformation is especially important for MEMS-based IR detectors subjected to thermal loading and/or operated at elevated temperatures. The inelastic strain behavior (creep) in metal layers results in inelastic deformation in MEMS-based IR detectors. Neglecting the inelastic deformation can lead to misinterpretations of the measurement data from MEMS-based IR detectors and can compromise performance.

In this chapter, the principles that were studied in Chapter 3 and Chapter 4 are applied to MEMS-based IR detectors. First, the thermal cycling technique is employed to flatten as-released MEMS-based IR detectors and characterize the linear thermoelastic behavior. Second, the characterized Power-law creep from Chapter 4 is used to develop an FEA model for predicting and simulating the inelastic behavior in long-term operation.

5.2. Experimental Procedure

5.2.1. Thermal Cycling

The thermal cycling approach has been demonstrated as an effective means to understand the stress response of thin films (Chen *et al.*, 2003) and the thermal mechanical evolution of multilayer microcantilevers (Miller *et al.*, 2007a, b). In this study, the measurement procedure is designed to carefully explore the deformation of the MEMS-based IR detector due to uniform heating and cooling cycles. The heating and cooling cycles are performed over a range of temperatures, including room temperature to 265 °C - 310 °C. The MEMS-based IR detector has a heating rate of 200 °C/min. When the temperature approaches the target temperature, the heating rate is decreased from 200 °C/min to 10 °C/min, allowing the stage temperature to slowly approach the target temperature. The cooling rate is approximately the same as the heating rate for the MEMS-based IR detector. Following the cooling period, the MEMS-based IR detector is heated and subsequently cooled for four cycles, with the maximum temperature increase in each cycle set to 15 °C. During the heating and cooling cycles, WYKO captures the image of the full-field out-of-plane deformation at increments of 20 °C. At each increment, the temperature is held for about 3 min to maintain the measurements at thermal equilibrium.

5.2.2. Isothermal Holding

In order to study the effects of creep and stress relaxation at two different holding

temperatures (80 °C and 125 °C), the deformation of the microcantilevers is measured as a function of time. First, the MEMS-based IR detectors are thermal cycled three times between room temperature and 295 °C to partially stabilize the Al microstructure and diminish the initial curvature. After the initial pre-cycles, the MEMS-based IR detectors are held at the isothermal holding temperature (125 °C and 100 °C) for about 45 hours. The full-field out-of-plane deformation is measured during the initial three pre-cycles and the isothermal holding period.

5.3. Finite Element Model

Commercial finite element software ABAQUS is again used to simulate the thermomechanical behavior of the MEMS-based IR detector. The initial condition of this model does not consider any residual stress in the layers. The MEMS-based IR detector is meshed with four-node composite shell elements (S4R); such a mesh is shown in Fig. 5.2. The thermomechanical behavior is studied in FEM using material and dimension input data from Table 3.1 and Table 5.1, respectively. The boundary conditions fix all the freedom at the end of two legs, and the parameters of geometry conform to real structures. For the thermoelastic response simulation, the mismatch strain is induced in the MEMS-based IR detectors due to the thermal expansion mismatch between Al and Si₃N₄ and uniform temperature change. This mismatch strain will consequently result in a bending curvature of the MEMS-based IR detectors. For inelastic deformation simulation during isothermal holding, the curvature evolution is modeled as a

function of time by assuming that the inelastic deformation mechanism can be described by Power-law creep in Al, which was obtained from the previous chapter (i.e. Eq. 4.6), and that the Si₃N₄ layer deforms elastically.

From the convergence study shown in Fig. 5.3, the percent error of the FEA results from different element lengths (*EL*) as compared with elements length of 1 μm, which can be expressed as

$$Error(\%) = \frac{FEA_{EL} - FEA_{1\mu m}}{FEA_{1\mu m}} \times 100\% \quad (5.1)$$

When the element lengths of free mesh are smaller than 1.25 μm, then the error of FEA results between different mesh is smaller than 0.2 %. Hence, the FEA model with 2784 elements, each with a length of 1 μm, in the simulation provides a converged result.

5.4. Results and Discussion

5.4.1. Planarity

The *in situ* thermal-mechanical response for a MEMS-based IR detector top bimaterial sensing plate is depicted in Fig. 5.4. Upon return to room temperature, the curvatures after each thermal cycle are different. The difference is caused by the evolution of the residual stresses of the bilayer structures in the high

temperature region (the nonlinear region is not plotted in the Fig. 5.4). For instance, the curvature at room temperature decreases from 7.3 mm^{-1} to 5.8 mm^{-1} following the first cycle, indicating significant structure flattening. As shown in Fig. 5.4, the curvature at room temperature continues to decrease when the MEMS-based IR detectors are subjected to a thermal cycling with a peak temperature higher than the previous peak temperature. In this study, the sensing plate initially bent downward with a curvature of 7.3 mm^{-1} . After the third thermal cycling with a peak temperature of $295 \text{ }^\circ\text{C}$, upon return to room temperature, the curvature is found to be approximately to -0.1 mm^{-1} , a 97 % reduction from the initial value. Hence, the optimal annealing temperature should be between $280 \text{ }^\circ\text{C}$ and $295 \text{ }^\circ\text{C}$, and the MEMS-based IR detector can be flattened by using thermal cycling with optimized peak temperatures. The result of this engineering approach is shown in Fig. 5.5 and Fig. 5.6. Also, Fig. 5.4 shows that the linear elastic response (dk/dT) of the IR detector before and after annealing at 295°C are $0.053 \text{ mm}^{-1}/^\circ\text{C}$ and $0.055 \text{ mm}^{-1}/^\circ\text{C}$, respectively. Therefore annealing doesn't affect the thermoelastic responses.

The as-fabricated $\text{Si}_3\text{N}_4/\text{Al}$ MEMS-based IR detector bends up due to the residual strain mismatch from its two layers (Fig. 5.7). As mentioned in Chapter 3, thermal cycling appears to be an effective method to modify the residual strain mismatch induced curvature. Fig. 5.7 depicts the residual strain mismatch at room temperature after each thermal cycle from FEM. A uniform temperature loading is

applied to each node in the finite element model. The magnitude of the temperature change is adjusted so that the simulated curvature of the microcantilever-based IR detector matches the measurement. The average strain mismatch along the central area of the sensing plate of the IR detector is then extracted from the FEM. The strain mismatch decreases with curvature reduction and the residual strain mismatch is zero when the microcantilever-based IR detector becomes flat.

Compared with the other known efficient flattening means for microcantilevers, such as ion machining (Bifano *et al.*, 2002) and rapid thermal annealing (Huang *et al.*, 2006), thermal cycling is a nondestructive method and can also provide in-depth understandings on the thermal mechanical evolution of the device. When the top electrode has a particular curvature defined by the equation:

$$f(x) = \frac{1}{2}\kappa x^2 + bx + c \quad (5.2)$$

the capacitance (C_p) between two electrodes can be defined as

$$C_p = \varepsilon \int_0^{\ell} \frac{1}{d + f(x)} dx \quad (5.3)$$

where ℓ is the length of the top electrode, ε is the permittivity of the insulator and

d is the gap between the two electrodes. The flattened MEMS-based IR detectors increase the capacitance signal readout.

5.4.2. Thermomechanical Response

The MEMS-based IR detectors show linear thermoelastic responses when subjected to temperature changes, i.e. the curvature varies linearly with temperature changes, as shown in Fig. 5.4. As mentioned in Chapter 3, the thermoelastic response ($d\kappa/dT$) of bilayer microcantilever beams can be expressed using Eq. 3.10. However, Eq. 3.10 cannot be applied to model the thermoelastic response of MEMS-based IR detectors, mainly due to the relatively complex geometry and boundary conditions of the detector structures. For instance, the experiment and FEM results demonstrate that the linear thermoelastic mechanical response is approximately $0.055 \text{ mm}^{-1}/^{\circ}\text{C}$. However, Eq. 3.10 gives a thermoelastic mechanical response of $0.074 \text{ mm}^{-1}/^{\circ}\text{C}$ with the material parameters listed in Table 3.1. Therefore, a modification to the model is needed to apply the plate theory model to describe the linear thermoelastic mechanical response of MEMS-based IR detectors.

In this study, a modified analytical solution, to describe the linear thermoelastic response of the MEMS-based IR detector, is obtained by introducing a correction factor. The proposed modified analytical solution for the linear thermoelastic mechanical response of MEMS-based IR detector is:

$$\left(\frac{\partial k}{\partial T}\right)_m = c \times \frac{\partial k}{\partial T} \quad (5.4)$$

where $(d\kappa/dT)_m$ represents the curvature of the MEMS-based IR detector and c is the correction factor. The correction factor in Eq. 5.4 is obtained by comparing the results from FEA and the corresponding analytical results. The proposed modified analytical solution results in a $d\kappa/dT$ of $0.055 \text{ mm}^{-1}/^\circ\text{C}$, which is consistent with the experimental results. In summary, the thermoelastic response of the MEMS-based IR detector can be described by the modified analytical solution proposed in this work, with the employment of a correction factor.

5.4.3. Parameter Study of the Thermomechanical

Section 5.4.2 demonstrates the validity of the modified analytical solution. The thermoelastic mechanical response $d\kappa/dT$ is described by using the modified analytical solution in Eq. 5.4. The percentage difference between the analytical solution in Eq. 3.10 and the modified analytical solution in Eq. 5.4 can be expressed as:

$$\text{Difference} = \left| \frac{\left(\frac{\partial k}{\partial T}\right) - \left(\frac{\partial k}{\partial T}\right)_m}{\left(\frac{\partial k}{\partial T}\right)_m} \right| \times 100\% \quad (5.5)$$

with the structure parameters in the current MEMS-based IR detector design

being: $m=0.2756$, $h=1$ and $\Delta\alpha=20.9\times 10^{-6}/K$. The correction factor and percentage difference are found to be 0.37 and 29.74 %, respectively. The percentage difference is mainly due to the boundary conditions and the complex geometries. The analytical solution in Eq. 3.10 is based on the bending of a bilayer microcantilever beam; however, the sensing component of the MEMS-based IR detector is connected to two deformable legs. The two bilayer cantilever beams support the sensing component of the MEMS-based IR detector, and the boundary is also deformed during thermal loading. A previous study has suggested that the deformable boundary is an important factor that results in the difference. A complicated mechanism model to modify boundary conditions has been employed to circumvent this problem (Cao *et al.*, 2005). However, the mechanism model still requires FEM to obtain required parameters to solve the deformable boundary condition. Moreover, the complex geometry of the sensing plate also partially attributes to the percentage difference. Although not shown here, the simulation results show that the curvature along the center of the sensing part of the IR detector with etching holes differs by less than 5 % from the structures without etching holes. The modified analytical solution provides a quick way to achieve the thermoelastic mechanical response for design purposes.

The thermoelastic mechanical response of bilayer cantilever structures depends on Young's modulus ratio (m), the thickness ratio (h) and the CTE mismatch ($\Delta\alpha$). In order for designers to develop alternative MEMS-based IR detectors using

different materials and bimaterial layers of different thickness, the effect on the correction factor and percentage differences must be evaluated. In Fig. 5.8(a), h and $\Delta\alpha$ are fixed, and the effect of Young's modulus ratio between the two materials is studied. The percentage differences from the theoretical model were relatively stable, ranging between 28-35%. As Young's modulus ratio increases, the correction factors are also relatively stable, ranging between 0.7 and 0.8. The effect of increasing the thickness of the top layer material with constant m and $\Delta\alpha$ is shown in Fig. 5.8(b). The percentage difference is small, indicating that the plate theory describes the curvature more accurately at higher thickness ratios. The correction factor value decreases as the thickness ratio increases. Fig. 5.8(c) shows the effect of increasing the CTE mismatch between the two materials with constant m and h . In general, the range of $\Delta\alpha$ of the MEMS-based IR detector materials studied are between 5×10^{-6} to $30 \times 10^{-6}/K$. Consequently, this study concentrates on this region. The percentage difference increases as the CTE mismatch increases from a $\Delta\alpha$ of 5×10^{-6} to $15 \times 10^{-6}/K$, and then decreases as the CTE mismatch increases from $\Delta\alpha$ of 15×10^{-6} to $25 \times 10^{-6}/K$, while the correction factor displays an opposite trend.

5.4.4 Inelastic Deformation in Long-term Operation

The Power-law creep obtained in Chapter 4 is further examined by an isothermal holding testing procedure on MEMS-based IR detectors, described in Section 5.2.2. By utilizing such a test, it is possible to validate and modify the obtained

Power-law creep relations on a device level, because both the deformation and the applied temperature are obtainable and controllable. For validation purposes, in this work, the inelastic deformation of a MEMS-based IR detector is measured and compared with the FEA results before utilizing the model for prediction. In Fig. 5.9, the experimental results show that the curvature decreases as time elapses during isothermal holding at temperatures of 100 °C and 125 °C. After the isothermal holdings at 100 °C and 125°C, the curvature decreases by 1.6 % and 15.1 %, respectively. Fig. 5.9 also shows the comparison between the FEA prediction and the experimental results. It can be seen that the tendencies of both sets of data essentially agree with each other, further validating the accuracy of the FEA model with Power-law creep.

As shown in Fig. 5.9, the curvature decreases by less than 1 % after 45 hours of isothermal holding at 80 °C. Although the time dependent deformation does not significantly exist at low temperature, which is usually the operational temperature of MEMS-based IR detectors, this methodology and model provides a beneficial tool to characterize and predict short- and long-term thermomechanical behaviors of thermal actuators and RF switches which operate at high temperatures (more than 100 °C).

5.5 Conclusions

In this chapter, thermal mechanisms are studied via thermal cycling to reduce the residual strain mismatch-induced curvature of the MEMS-based IR detectors. A thermal system and an interferometer are adopted to monitor the full-field curvature change *in situ*. Thermal cycling reduces the residual strain mismatch within the bilayer device and thus flattens the MEMS-based IR detectors. The linear thermoelastic mechanical response of the MEMS-based IR detector is characterized by using a modified analytical solution that employed a correction factor to modify a present plate theory. The three critical parameters, Young's modulus ratio, the thickness ratio and the CTE mismatch are studied. Although bilayer ($\text{Si}_3\text{N}_4/\text{Al}$) MEMS-based IR detectors are used in this design, this study can be generalized to other MEMS-based IR detectors with different geometries and materials. Moreover, a comprehensive FEA model with Power-law creep is developed for MEMS-based IR detectors, to predict the curvature evolution in short- and long-term operation.

Table 5.1: Dimension input data of FEM model for MEMS-based IR detectors

L_{leg} (μm)	L_{plate} (μm)	W_{leg} (μm)	W_{plate} (μm)	R (μm)	Thickness of Al (nm)	Thickness of Si_3N_4 (nm)
50	50	3	40	5	200	200

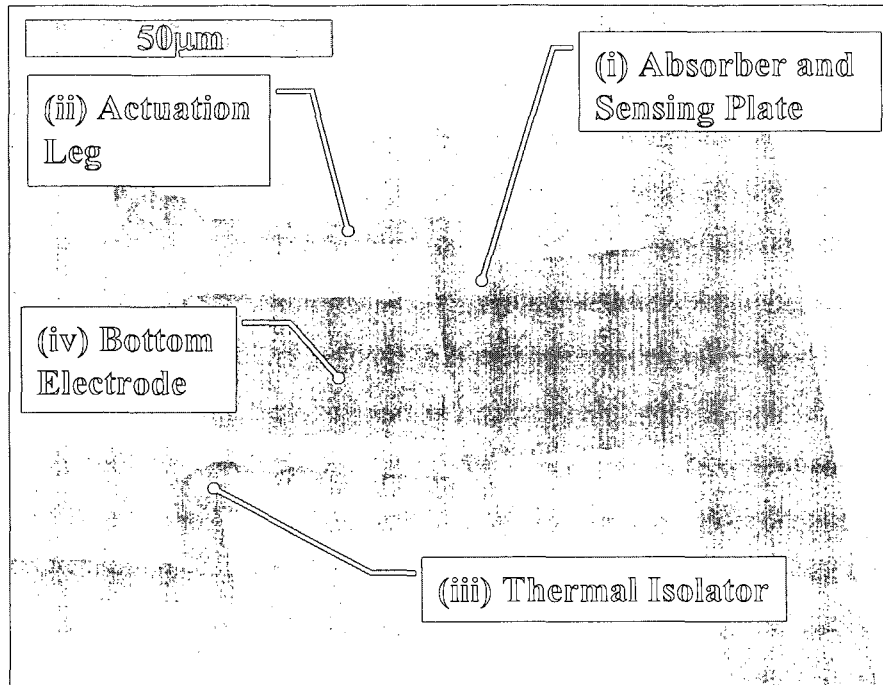


Fig. 5.1: An SEM image of a MEMS-based IR detector on bottom electrodes of Pt/Ti. Both the Si_3N_4 layer and the Al layer have a thickness of 200 nm.

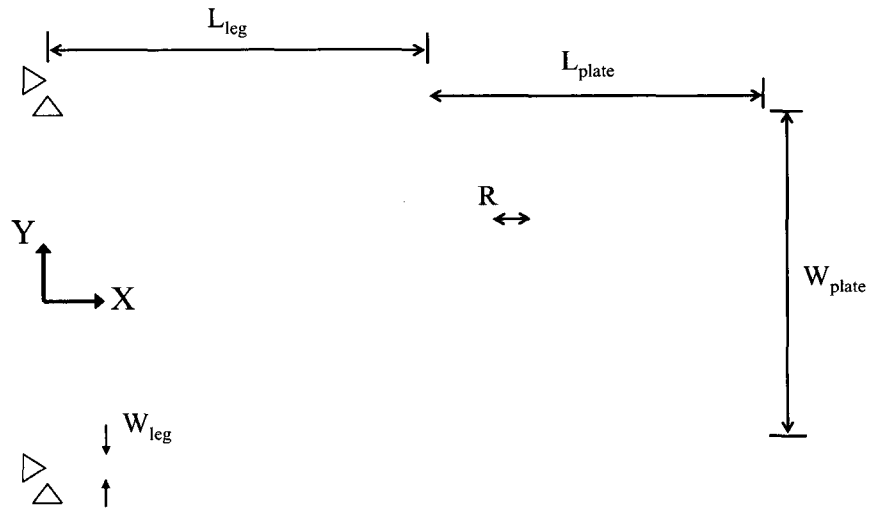


Fig. 5.2: Finite element mesh of a MEMS-based IR detector which is formed with two actuation legs and a sensing plate.

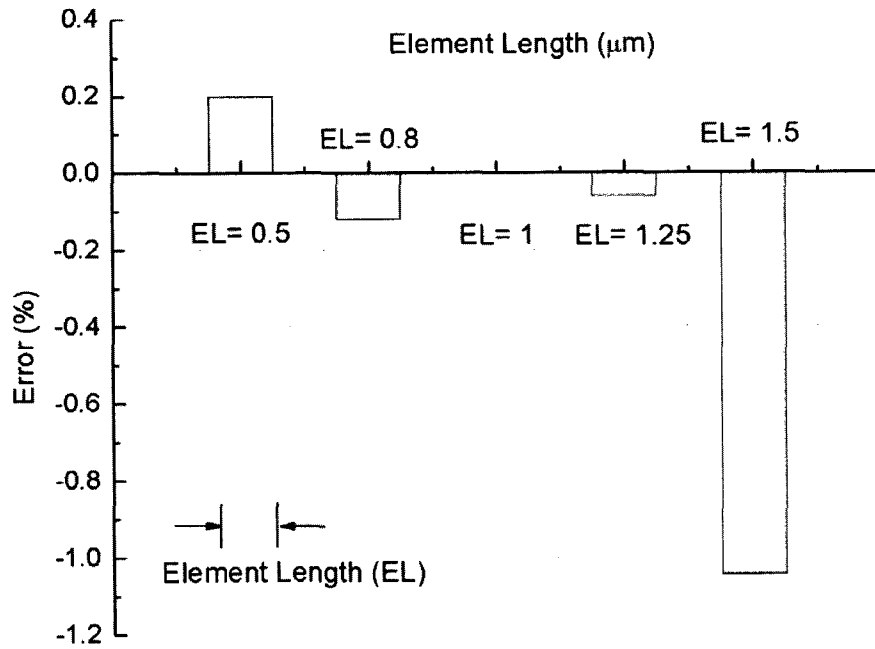


Fig. 5.3: Convergence study of thermomechanical behavior simulation for MEMS-based IR detectors.

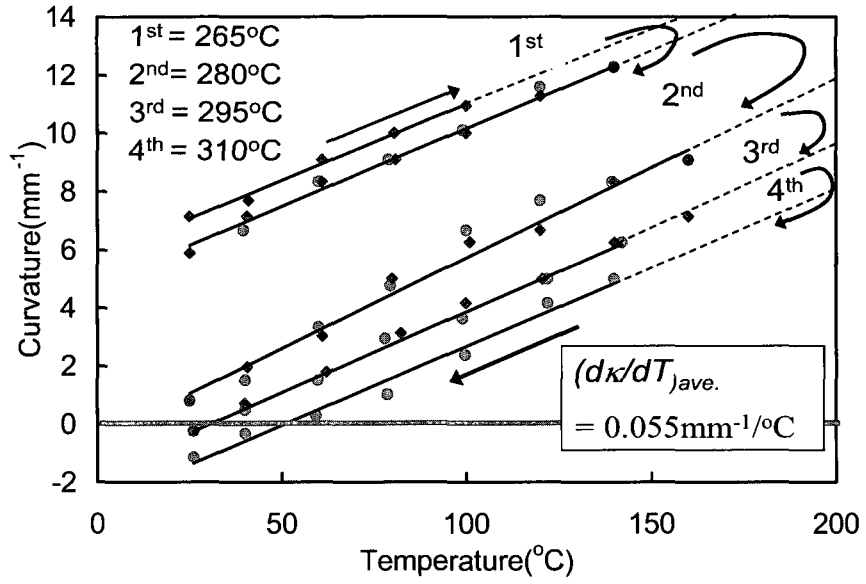
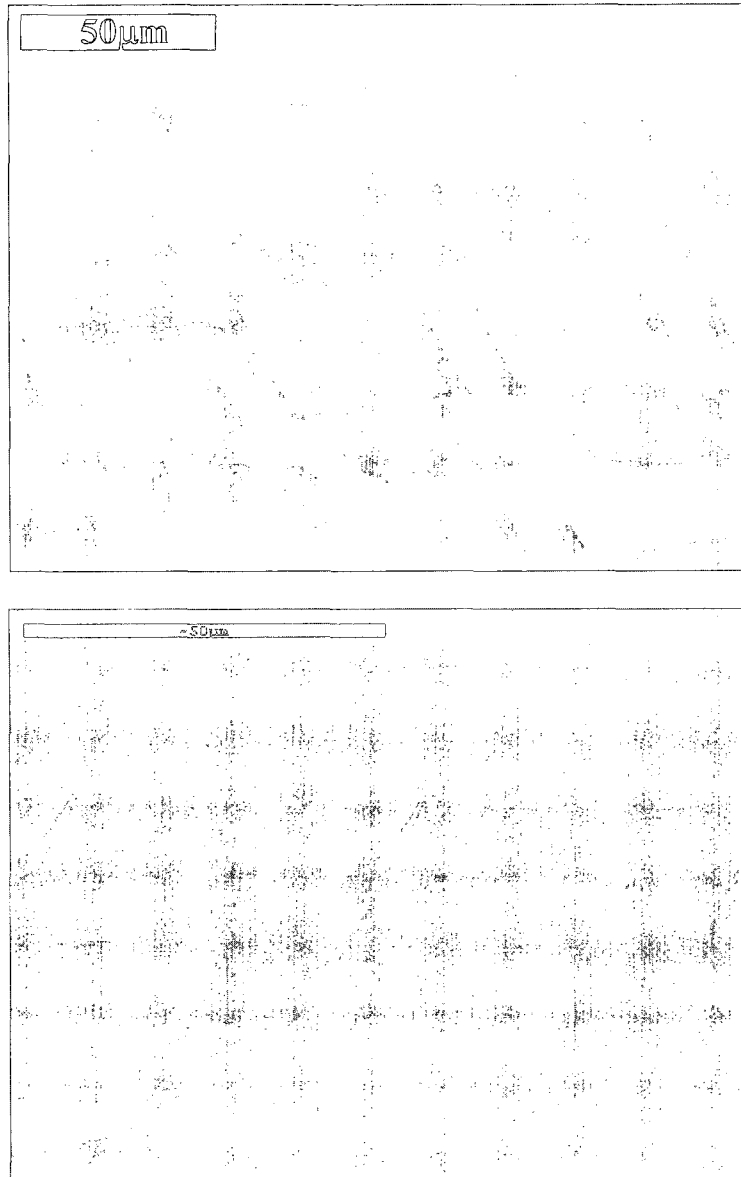
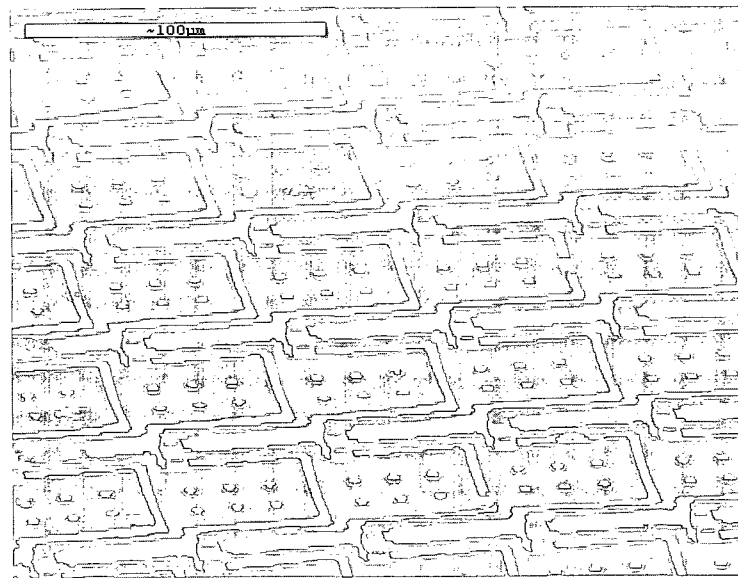
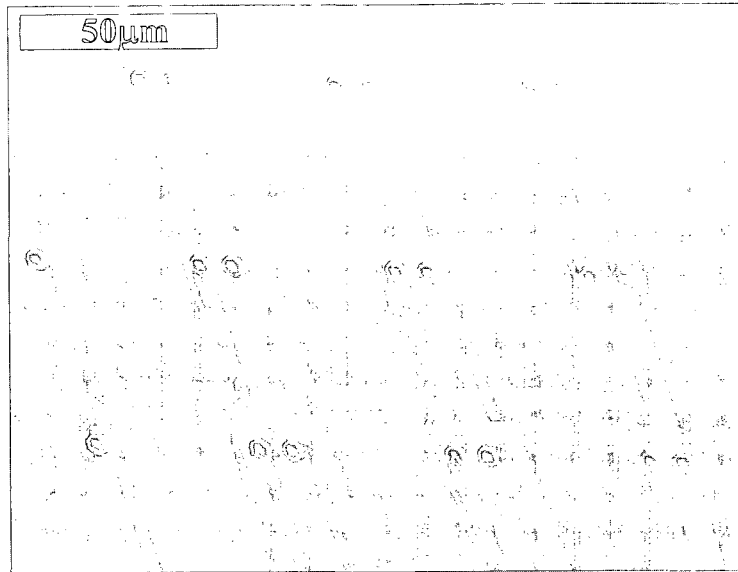


Fig. 5.4: Curvature vs. temperature during the four thermal cycles with different peak temperatures. (Temp. increase: blue symbols; Temp. decrease: pink symbols)



(a)

Fig. 5.5: SEM image of as-released MEMS-based IR detectors which have residual strain mismatch induced curvature.



(b)

Fig. 5.6: SEM image of flattened IR detectors after thermal cycling with a peak temperature of 295 °C.

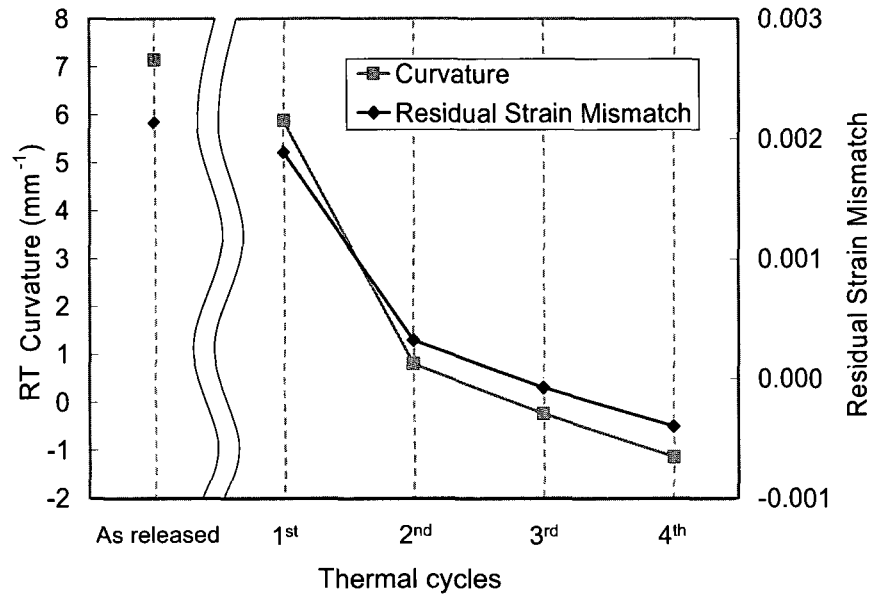
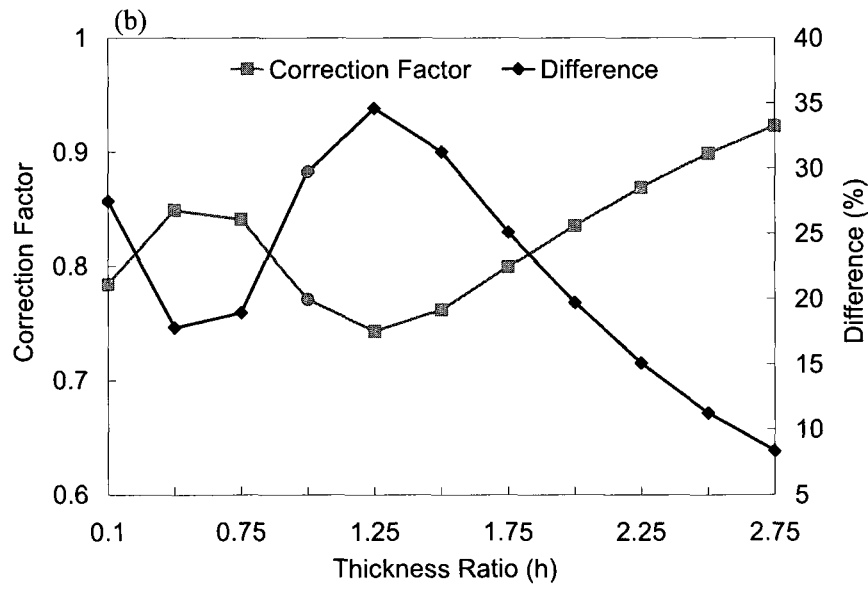
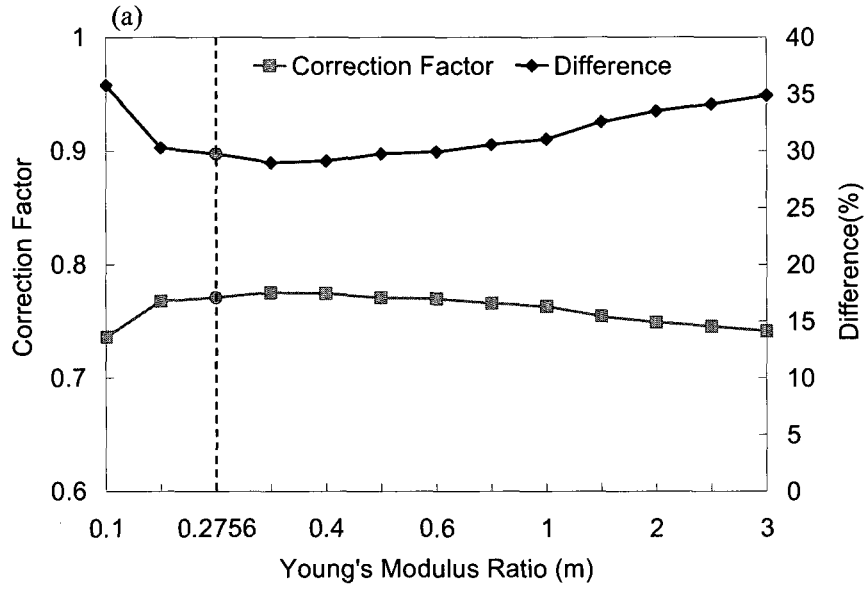


Fig. 5.7: Measured room temperature (RT) curvature and calculated residual strain mismatch after each thermal cycle from Fig. 5.4.



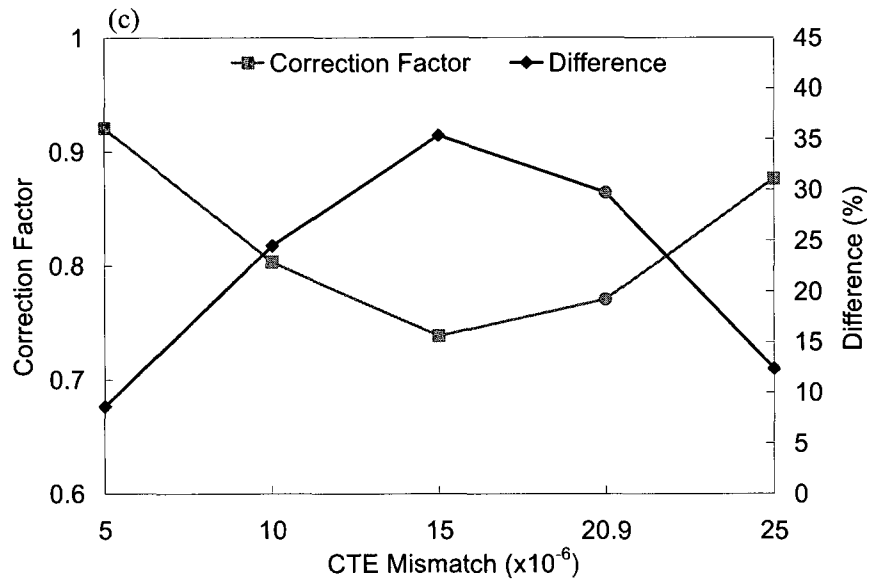


Fig. 5.8: Correction factor and the percentage curvature difference varies as the parameters such as (a) Young's modulus ratio (m), (b) thickness ratio (h) and (c) mismatch of CTE ($\Delta\alpha$) changes.

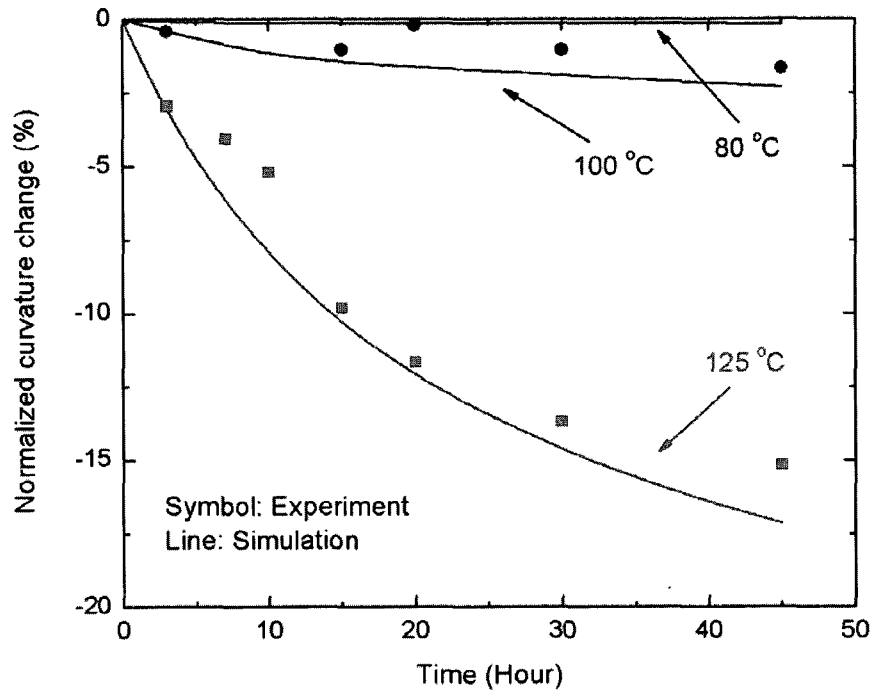


Fig. 5.9: Experimental and simulation result of isothermal holding test on MEMS-based IR detectors.

CHAPTER 6: INELASTIC DEFORMATION OF BILAYER MICROCANTILEVER BEAMS WITH NANOSCALE COATING

6.1 Introduction

From the design viewpoint, the ideal bilayer microcantilevers deform linearly proportional to temperature change and do not exhibit inelastic deformation over the operation period. However, the metal layers are typically not stable after deposition (Dunn *et al.*, 2002; Zhang and Dunn, 2003, 2009). When they are subjected to thermal loading, especially isothermal holding, the microstructural evolution in metal layers can be triggered, such as extinction of excess vacancies, subgrain coalescence and grooving (Miller *et al.*, 2005, 2007a, b; Zhang and Dunn, 2004; Gall *et al.*, 2004). The microstructural evolution results in inelastic strain behavior in metal layers and thus highly inelastic deformation in bilayer microcantilevers. Neglecting the inelastic deformation can result in misinterpretations of the measurement data from bilayer microcantilever-based sensors and can compromise control precision of actuators. Hence, it is of vital importance to perform accurate thermomechanical behavioral characterization on bilayer microcantilevers and to develop an appropriate model for the description of its time-dependent inelastic deformation.

In order to address the aforementioned needs, we studied the thermomechanical deformation of Au/Si₃N₄ microcantilever beams with combined effects of geometric and material nonlinearity. These behaviors need to be fully understood in order to better design, characterize and manufacture reliable MEMS structures and devices. In addition, we demonstrated that the time-dependent inelastic deformation can be suppressed by the use of nano-coatings realized by atomic layer deposition (ALD). Our study suggested that the nanoscale coating causes alternation of the stress state in the metal layer and a change in the fundamental inelastic deformation mechanisms. In this present work, we performed a rational analysis/characterization of thermomechanical deformation on coated Au/Si₃N₄ microcantilevers, and used Finite Element Analysis (FEA) with Power law creep to describe the inelastic deformation of the microcantilevers over a significant period of time. Section 6.2 describes the fabrication of alumina- uncoated/coated microcantilever beams. Interferometric microscopy was employed to *in-situ* measure the deformation of microcantilever beam subjected thermal loading as mention in Section 2.3. Finite element analysis procedure was presented in Sections 6.3. Section 6.4 covers the thermomechanical evolution and the modeling results of the deformation of alumina- uncoated/coated microcantilever beams during thermal cycling and isothermal holding. Section 6.4 also discusses and correlates the microstructural evolution to observed thermomechanical deformation during isothermal holding on both uncoated and coated microcantilever beams using SEM and AFM.

6.2 Specimens Preparation

The alumina- uncoated/coated Au/Si₃N₄ bilayer microcantilever beams were fabricated. The process flow of fabrication procedure is shown in Fig. 6.1. The uncoated and coated Au/Si₃N₄ bilayer microcantilever beams consisted of interposed arrays of 6 Au/Si₃N₄ bilayer microcantilever beams with a 40 μm width and lengths ranging from 60 μm to 360 μm with 60 μm increments. Fig. 6.2 shows one of the specimen arrays, where a 0.5 μm gold layer was grown on top of a 1.15 μm Si₃N₄ layer using surface micromachining techniques with SiO₂ as the sacrificial layer.

Before fabrication, Piranha solution (H₂SO₄:H₂O₂=3:1) and 40% Hydrofluoric acid solution were used to clean the native oxides and organic residues from the <100> silicon wafer, respectively. The first step of the fabrication was to deposit a 1.5 μm thick SiO₂ film as a sacrificial layer using plasma enhanced chemical vapor deposition (PECVD) (PECVD Multiplex, STS Inc.). The SiO₂ layer was then patterned using reactive ion etching (RIE) (790, Plasma-Therm LLC.) with SF₆ gasses to create anchors for the microcantilever beams, as shown in the Fig. 6.1(a). Following the etching processes, a 1.15 μm-thick Si₃N₄ layer and 0.5 μm-thick Au layer with a 5 nm Cr adhesion layer were deposited on top of the SiO₂ layer in series using PECVD and an E-beam thermal evaporator (Auto 306 R&D, BOC Edwards Limited). To make the bilayer cantilevers, the Au/Si₃N₄ bilayer

was patterned using Potassium iodide solution (KI) and RIE with SF₆ and He, respectively, as shown in Fig. 6.1(b). Subsequently, the specimen containing sets of Au/Si₃N₄ bilayer microcantilevers was immersed in the buffered oxide etcher (BOE) for 30 minutes to remove the sacrificial SiO₂ layer. In order to prevent the microcantilever beams from sticking to the substrate, the specimen was immersed in methanol after BOE etching and then dried with a supercritical CO₂ release system, as shown in Fig. 6.1(c). One group of the Au/Si₃N₄ bilayer microcantilever beams were used to investigate their thermal mechanical characteristics including temperature and time -dependent deformation. Another group of the specimens were coated with alumina (Al₂O₃) using ALD technique (Savannah S100, Cambridge NanoTech Inc.), as shown in Fig. 6.1(d), in preparation for inelastic deformation suppression tests. The trimethyl aluminum (Al(CH₃)₃; TMA) and water (H₂O) were used in ALD as two reactants under a pressure of 0.93 Torr at 100 °C (Ott *et al.*, 1997; Leskela and Ritala, 2001). By repeating this bilayer reaction sequence cycle, a linear, atomic-layer-controlled alumina growth was produced. The microcantilever beams were coated with 5 nm, 10 nm, 20 nm, and 40 nm alumina layers resulting from 6, 12, 23, and 45 cycles, respectively.

6.3 Finite Element Model

The finite element model with Power law creep in the Au layer were employed to simulate the inelastic deformation during isothermal holding (Keller *et al.*, 1999;

Shen and Suresh, 1995; Chen *et al.*, 2008). During isothermal holding, Si₃N₄ is assumed to be relatively stable due to the relatively higher melting temperature (1900 °C) and creep resistance compared to Au (Zhang and Dunn, 2004; Gall *et al.*, 2004). Hence, assuming the Si₃N₄ deforms elastically and the inelastic deformation mechanism described by power law creep in the Au layer, the inelastic deformation during isothermal holding could be modeled and represented by using curvature evolution as a function of time. To determine the parameters of Power law creep (A and n in Eq. 4.2), results from FEA was fit to the experimental data. Commercial finite element software ABAQUS v.6.7 was used to perform the simulation (Hibbit, 1998). The FEA model with the same geometry as the uncoated microcantilever beam was constructed. Composite shell elements (S4R) were used with a mesh consisting of 18041 nodes and 3600 elements. Fixed boundary conditions were applied to one end of the beam. Residual stress in each layer was not considered in this model. The inelastic deformation was studied in FEA, using the input data, namely $t_{Au} = 500 \text{ nm}$, $t_{Si_3N_4} = 1150 \text{ nm}$, $E_{Au} = 78 \text{ GPa}$, $E_{Si_3N_4} = 148 \text{ GPa}$, $\alpha_{Au} = 14 \times 10^{-6} / \text{K}$, $\alpha_{Si_3N_4} = 2 \times 10^{-6} / \text{K}$, $\nu_{Au} = 0.4$, and $\nu_{Si_3N_4} = 0.2$, where t is the thickness of the material, E , α , and ν represent the Young's modulus, CTE, and Poisson's ratio, respectively (Shackelford and Alexander, 2001). The model of alumina-coated microcantilever beams consisted of 4 layers, including alumina, Si₃N₄, Au and alumina from the bottom to top layer, where the Young's modulus and Poisson ratio of alumina are 203 GPa and 0.24, respectively (Tripp *et al.*, 2006). To match the experimental

procedure, a uniform temperature change was firstly applied followed by isothermal holding.

6.4 Results and Discussion

6.4.1 Thermal Cycling

We first characterized the temperature-dependent deformation of uncoated and coated microcantilever beams during heating and cooling cycles. In each thermal cycle, the bilayer microcantilever beams were heated from room temperature (25 °C) to specified maximum temperatures and then cooled back down to room temperature. As shown in Fig. 6.3(a), the bilayer microcantilever beams have an initial curvature in their as-released state due to the residual stress in Au and Si₃N₄ layers. During the heating process in the first cycle, the curvature decreased linearly with a constant $dk/dT = -0.0081 \text{ mm}^{-1}/^{\circ}\text{C}$ from room temperature to 100 °C. When the temperature continued to rise, a critical temperature was reached where the curvature changed at a much smaller dk/dT . Similar behavior has been observed in other studies and was attributed to the onset of inelastic deformation (Lin *et al.*, 2009; Lin *et al.*, 2008; Zhang and Dunn, 2003). This inelastic deformation continued until the maximum temperature (125 °C) was reached in the first cycle. During this region, the temperature-induced microstructural change in Au occurs as grain boundaries consolidate and other defects are removed, resulting in tensile straining of the Au film (Zhang and Dunn, 2003, 2004; Gall *et al.*, 2004). Upon cooling from the maximum temperature (125

°C) to room temperature in the first cycle, the curvature increased linearly again throughout the whole process. The slopes of curvature change during both heating and cooling were approximately the same. After returning to room temperature, the curvature of the microcantilever beams was found to be larger than that prior to the cycle. The microcantilevers were heated and subsequently cooled for three more cycles with 150 °C, 175 °C and 200 °C as the peak temperatures. The deformation behavior manifested by thermoelastic and inelastic regions exhibit in each thermal cycle are similar and the subsequent room temperature curvature increased after each cycle. The thermomechanical evolution of 10 nm alumina-coated microcantilever beams is similar as the uncoated microcantilever beams, as shown in Fig. 6.3(b). The presence of alumina layer changed the thermoelastic slope dk/dT slightly to $-0.0072 \text{ mm}^{-1}/^{\circ}\text{C}$. From the design perspective, a desired linear curvature-temperature relation can be achieved by manipulating the maximum temperature of thermal cycling. For repeated cycles below the critical temperature, linear thermoelastic behavior occurs throughout the entire cycle. Linear curvature-temperature relation allows for enhanced reliability during operation and can be predicted analytically. We refer to previous studies (Lin *et al.*, 2009; Lin *et al.*, 2008; Zhang *et al.*, 2004) for a more detailed discussion.

6.4.2 Isothermal Holding

To characterize the time-dependent deformation of uncoated microcantilever

beams, the isothermal holding with various holding temperatures (100 °C, 150 °C and 200 °C) were used. The microcantilever beams underwent thermal cycling three times between room temperature and the isothermal holding temperatures to partially stabilize the Au microstructure and then held at the isothermal holding temperature for 60 hours (Zhang and Dunn, 2004; Lin *et al.*, 2009). During the heating process in the first cycle between room temperature and 150 °C, thermoelastic and inelastic deformation was observed, as shown in Fig. 6.3 (a). In the following second and third cycles, the microcantilever beam deforms thermoelastically and does not have significant inelastic deformation. For the 100 °C and 200 °C isothermal holding test, the microcantilevers were subject the three pre- thermal cycles between room temperature and 100 °C and 200 °C, respectively. After the three pre- thermal cycles, the microcantilever beams were then held at 100 °C, 150 °C, and 200 °C for 60 hours. Meanwhile, the interferometer was employed to *in-situ* measure the full field out of plane deformation. Fig. 6.4 shows that the curvature decreases as time elapsed during isothermal holding at 100 °C, 150 °C, 200 °C. After the isothermal holding at 100 °C, 150 °C and 200°C, the curvature decreased by 2.7 %, 14% and 25%, respectively.

The experiment procedure of isothermal holding test on alumina-coated microcantilever beams is the same as uncoated microcantilever beams. These beams were subjected to three pre- thermal cycles between room temperature

and 150 °C and then held at 150 °C for 60 hours. Fig. 6.5 depicts the curvature of the microcantilever beams coated with 5 nm, 10 nm, 20 nm and 40 nm alumina decreasing by 11.2 %, 6.4 %, 5.6 % and 4.4%, respectively, from the initial curvature over the hold period of 60 hours. Fig. 6.5 also reveals the suppression capability of alumina as a function of thickness. The curvature evolution during isothermal holding changes as the alumina thickness decreases because the thicker alumina provides more constraint stress on the Au layer. The suppression of inelastic deformation during isothermal holding associated with stress evolution and microstructural will be discussed in Section 6.4.3 and Section 6.4.4 respectively. Compared with the inelastic deformation on the uncoated microcantilever beams held at 150 °C for 60 hours in Fig. 6.5, the 40 nm alumina coating significantly suppressed the inelastic deformation of the Au/Si₃N₄ microcantilever beams from 14% to less than 4.4 %.

6.4.3 Finite Element Analysis

In conjunction with the testing data shown in Section 6.4.2, FEA with Power law creep were used to describe the inelastic deformation behavior of Au/Si₃N₄ microcantilever beams during isothermal holding. By using a constant $n=5$ and different A values ($A=0.8\times 10^{-15} \text{ h}^{-1}\text{MPa}^{-5}$, $5.2\times 10^{-15} \text{ h}^{-1}\text{MPa}^{-5}$, and $8\times 10^{-15} \text{ h}^{-1}\text{MPa}^{-5}$ for 100 °C, 150 °C and 200 °C, respectively), the inelastic deformation behavior during isothermal holding was described well (Fig. 6.4). Fig. 6.6 shows the stress distribution through the thickness taken at the center of the

microcantilever beam for $t = 0, 10, 20, 40$ and 60 hours during isothermal holding. At $t = 0$, the stress gradient exists across both the Au and Si_3N_4 layer. In the first 10 hours of isothermal holding, the majority of tensile stress relief in Au due to the compressive stress generated from grain grooving, which will be discussed in Section 6.4.3. Beyond 40 hours of isothermal holding, stresses display much less change. The quantified film stresses in the microcantilever beams help us to understand the thermomechanical and microstructural evolution in Section 6.4.2 and Section 6.4.4 respectively.

An associated finite element model was also constructed to simulate the inelastic deformation of alumina-coated microcantilever beams held at $150\text{ }^\circ\text{C}$ for 60 hours. The material parameters in the Power law creep model of Au obtained from the isothermal holding on uncoated microcantilever beams (i.e., $\dot{\epsilon} = 5.2 \times 10^{-15} \sigma^5$) was incorporated into the finite element model. Although not shown here, the FEA simulation shows a decrease in the curvature change with temperature, but nowhere near the magnitude of that observed. This suggests that the alumina coating not only alters the stress state in the Au layer but also the fundamental deformation mechanisms. This phenomenon was also found in previous literature (Miller *et al.*, 2007a, b; Zhang *et al.*, 2004). This implies that the power law obtained from uncoated microcantilever beams can not be used to model the inelastic behavior of Au for alumina-coated microcantilever beams. Hence, we modified the material parameters in the power law by fitting FEA results to the

experimental data of the alumina-coated microcantilever beams. Again, the appropriate power law of Au (constant $n=5$; $A=3.5 \times 10^{-15} \text{ h}^{-1} \text{MPa}^{-5}$, $1.1 \times 10^{-15} \text{ h}^{-1} \text{MPa}^{-5}$, $1.6 \times 10^{-15} \text{ h}^{-1} \text{MPa}^{-5}$, and $0.6 \times 10^{-15} \text{ h}^{-1} \text{MPa}^{-5}$ for 5 nm, 10 nm, 20 nm and 40 nm alumina-coated microcantilever beams, respectively) for alumina-coated microcantilever beams was obtained. Fig. 6.5 shows the comparison between the FEA simulation with a modified power law and the experimental results. It can be seen that the tendencies of both sets of data essentially agree with each other. Fig. 6.7 shows the tensile stress does not significantly decrease, comparing with Fig. 6.6(b), because the microstructure evolution is suppressed by 10 nm alumina. Hence, the inelastic deformation of alumina-coated microcantilever beams (Fig. 6.5) is much smaller than uncoated (Fig. 6.4).

6.4.4 Microstructural Evolution

The inelastic deformation of uncoated and coated microcantilever beams during isothermal holding may be due to the volumetric change in the Au layer (Miller *et al.*, 2005, 2007b; Ohring, 2002). It is commonly accepted that the tensile stress in the metal layer is generated by volumetric reduction such as recovery, grain growth, recrystallization (Nix, 1989), surface texture consolidation (Thouless, 1993), and hillocking (Hwang *et al.*, 2006). On the other hand, the compressive stress in the metal layer is generated by volumetric addition such as grain boundary grooving (Mullins, 1958), grain boundary separation (Harris and King, 1995), diffusion of a foreign chemical species, precipitation, and chemical

reaction (Gardner and Flinn, 1990).

The inelastic deformation occurred in a high temperature region of three pre-thermal cycles due to the recovery and grain growth. The microstructure of the evaporated Au was not stable in the as-deposited condition and the increased temperature promoted Au subgrain to coalesce (Zhang and Dunn, 2003; Nix, 1989). This temperature-induced microstructural evolution is typically a volumetric reduction process which will result in an increased tensile stress in the Au layer. The generated tensile stress competes with the compressive stress due to thermoelastic deformation and thus results in a much smaller $d\kappa/dT$ in the inelastic regime than in the thermoelastic regime (Fig. 6.3). After partially stabilizing the microstructural Au during three pre-thermal cycles, the microcantilever beams were subjected to isothermal holding temperature for 60 hours. During the isothermal holding, grain growth stagnates thereafter, marked by the formation and growth of grooves at the grain boundaries (Miller *et al.*, 2005, 2007b). SEM was employed to measure the microstructural evolution on Au as shown in Fig. 6.8. Initially, the Au surface is relatively smooth in the as-released beams at room temperature as shown in Fig. 6.8(a). For the microcantilever beam held at an isothermal holding temperature of 100 °C as seen in Fig. 6.8(b), the grain size and grain grooving of Au surfaces were slightly increased compared with the as-released microcantilever beams. After 150 °C and 200 °C isothermal holdings, the grain size and groove size were significantly

increased and morphology was rougher as shown in Fig. 6.8(c-d). The grooving process usually accompanies with diffusion and oxidation of Cr and Si (Miller *et al.*, 2005, 2007b). The grain grooving, diffusion and oxidation are typically volumetrically addition processes, which result in increased compressive stresses in the Au layer (Miller *et al.*, 2007b). Such microstructural evolution correlates with the decreases in curvature of the microcantilever beams during isothermal holding. The mean roughness (R_a) and mean square roughness (R_q) of the Au layer are shown in Table 6.1. The roughness of the Au surface is increased 0.2 %, 15.7 % and 20.7 % by 100 °C, 150 °C, and 200 °C isothermal holdings, respectively. Previous studies have shown that the grain growth process, which results in tensile stress generation in Au layer, can be triggered by thermal cycling (Hearne *et al.*, 1999; Venkatraman and Bravman, 1992). Our SEM results demonstrated that grain grooving was activated after the isothermal holding period. The degree of both the grain growth and grain grooving processes are highly dependent on holding temperature.

SEM was also employed to measure the morphology on the alumina-coated microcantilevers, as shown in Fig. 6.9. Although the Au was covered by nanocoating, the grain size and grain boundary of the Au can clearly still be measured. After 60 hours of isothermal holding at 150 °C, the morphology images do not show any significant difference between the 20 nm, and 40 nm alumina-coated microcantilever beams, and the grain size are close to the Au

layer on the as-released beams as shown in Fig. 6.8(a). For the 5 nm and 10 nm alumina-coated microcantilevers, however, the grain size and grooving seem slightly increased, but nowhere near the magnitude of that observed on the uncoated microcantilever beams in Fig. 6.8(c). This suggests that the alumina nanocoating constrains the Au surface and suppresses the grain growth and grain grooving during the isothermal holding. Previous literatures also found that diffusion and oxidation were suppressed by nanocoating of thick native oxide (Shen and Suresh, 1995; Shen and Ramamurty, 2003). In addition, thicker alumina coating layer suppresses more inelastic deformation during isothermal holding. As shown in Fig. 6.10, the stress decrease in Au is inversely proportional to the thickness of alumina. This may be because that the thicker alumina layer provides more constraint stress on the Au surface and more effectively suppresses the net volumetric change in Au from grain growth, grooving, diffusion and oxidation.

6.5 Conclusions

Understanding of the thermomechanical behavior of coated and uncoated microcantilevers, including temperature and time- dependent deformation, is critical to the acquisition of the robust and reliable MEMS structures and devices for the next generation. The present study forms a comprehensive methodology for the thermomechanical characterization of coated/uncoated bilayer microcantilevers to meet the performance and reliability requirements of MEMS

devices, as well as a FEA model to describe the inelastic deformation and stress evolution in such structures. Moreover, to better understand the stress evolution and alumina suppression mechanism, SEM and AFM were employed to explore the grain growth and grain boundary grooving after isothermal holding. Results from this study also contribute to the fundamental understanding and analysis of similar thermomechanical responses of similar microcantilevers commonly used in MEMS.

Table 6.1: Surface roughness of uncoated microcantilever beams after isothermal holding at various temperatures.

	RMS roughness (nm)	Average roughness (nm)
As-released	4.92	4.01
100 °C	4.95	4.02
150 °C	5.896	4.64
200 °C	6.159	4.84

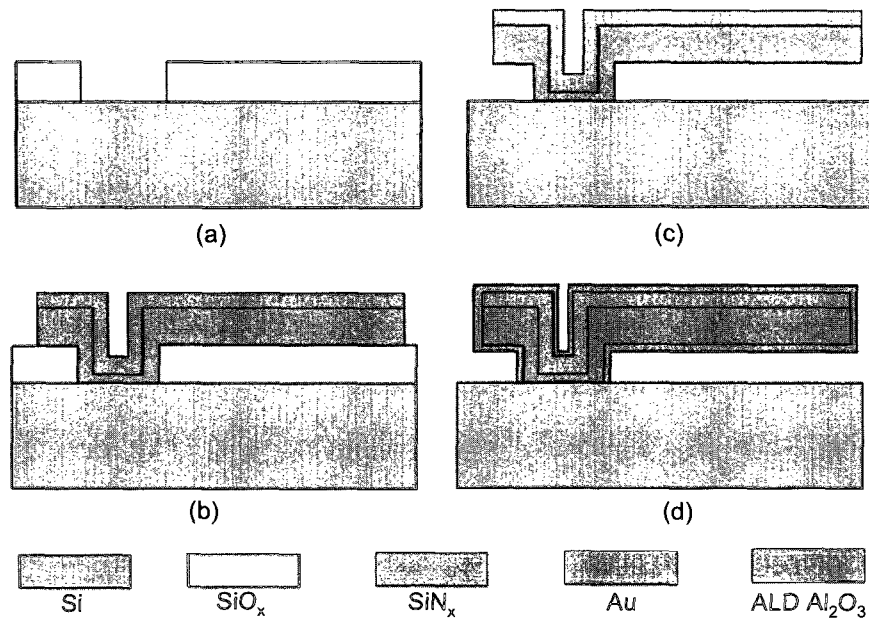


Fig. 6.1: Fabrication process of the Au/ Si₃N₄ bilayer microcantilever beams with nanocoating: (a) deposition of 1.5 μm thick SiO₂ and etching of SiO₂ by RIE with SF₆, (b) deposition of a 1.15 μm thick PECVD Si₃N₄ layer and a 0.5 μm thick e-beam evaporated Au layer, and patterning of Au and Si₃N₄ layers using KI and RIE with SF₆ and He, respectively, (c) releasing of the microcantilever beams by isotropic etching of SiO₂ with BOE and then drying by supercritical CO₂ release system, (d) nanocoating of alumina by ALD.

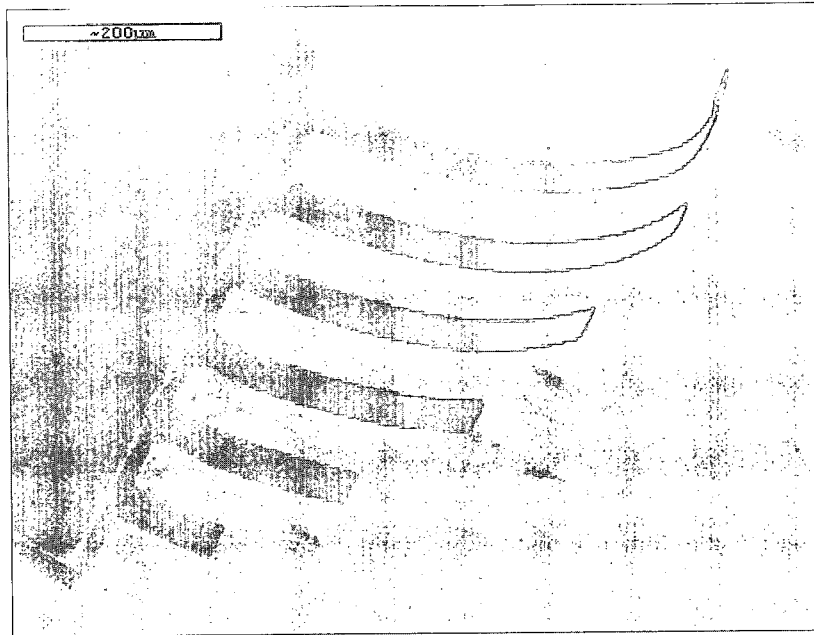
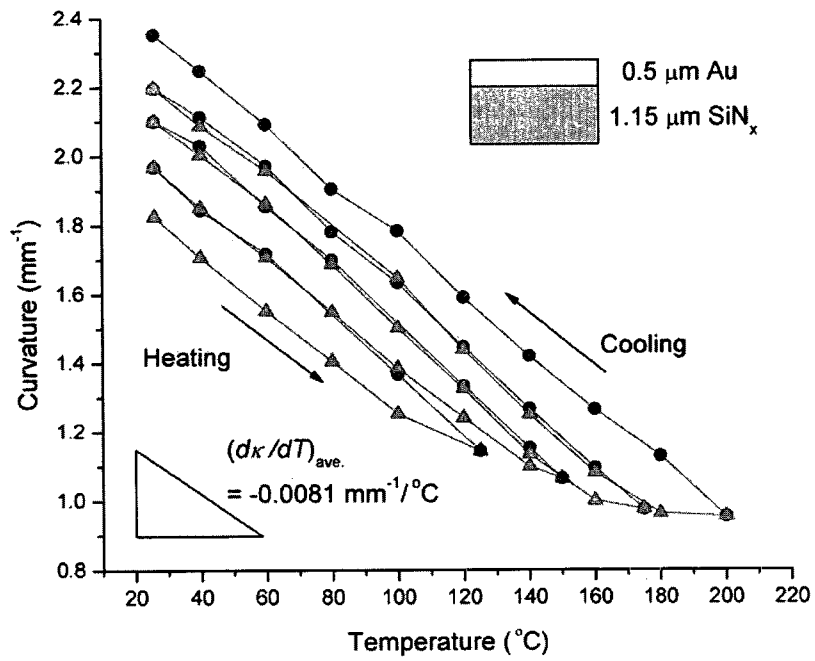
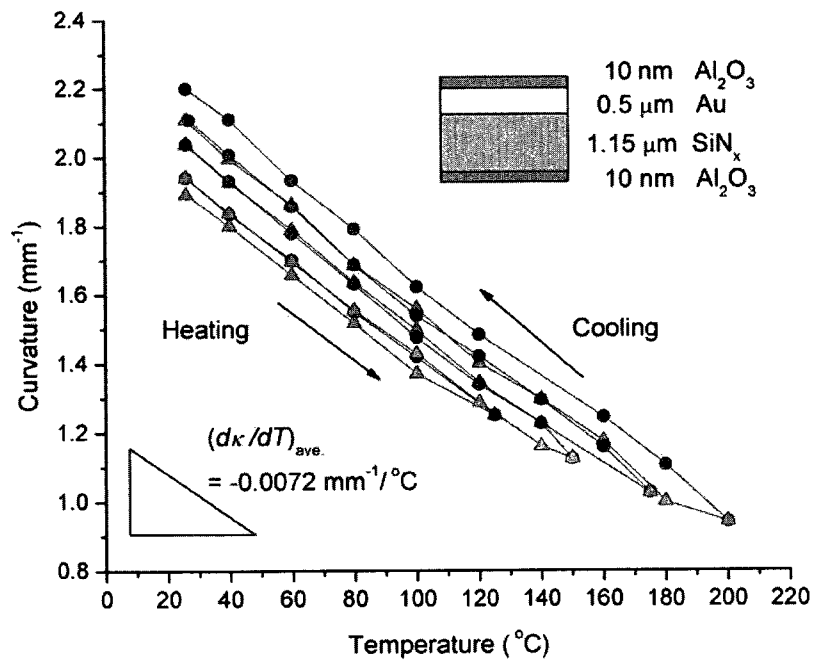


Fig. 6.2: SEM image of an array of Au ($0.5\ \mu\text{m}$ thick)/ Si_3N_4 ($1.15\ \mu\text{m}$ thick) microcantilever beams suspended over a silicon substrate.



(a)



(b)

Fig 6.3: Curvature of (a) Au/ Si₃N₄ microcantilever beams and (b) ALD alumina coated microcantilever beams as a function of temperature during four thermal cycles with peak temperatures of 125 °C, 150 °C, 175 °C, and 200 °C. The triangle and circle symbols are measured curvatures during the heating and cooling process in each cycle, respectively.

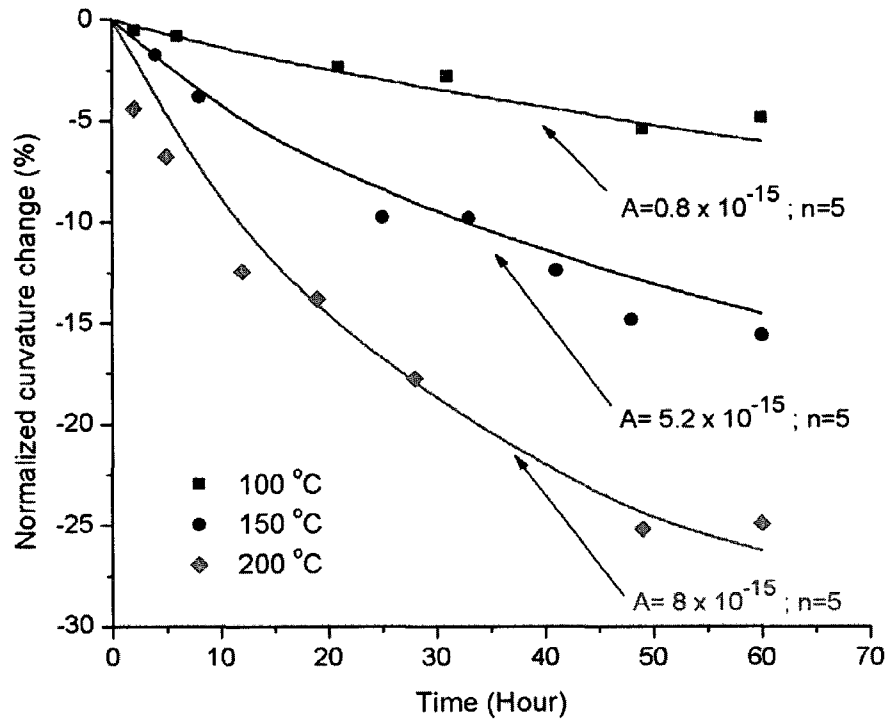


Fig. 6.4: Curvature evolution during the 60 hours isothermal holding at 100 °C, 150 °C and 200°C for Au/ Si₃N₄ microcantilever beams. The symbols represent experimental data while the solid lines represent simulation results.

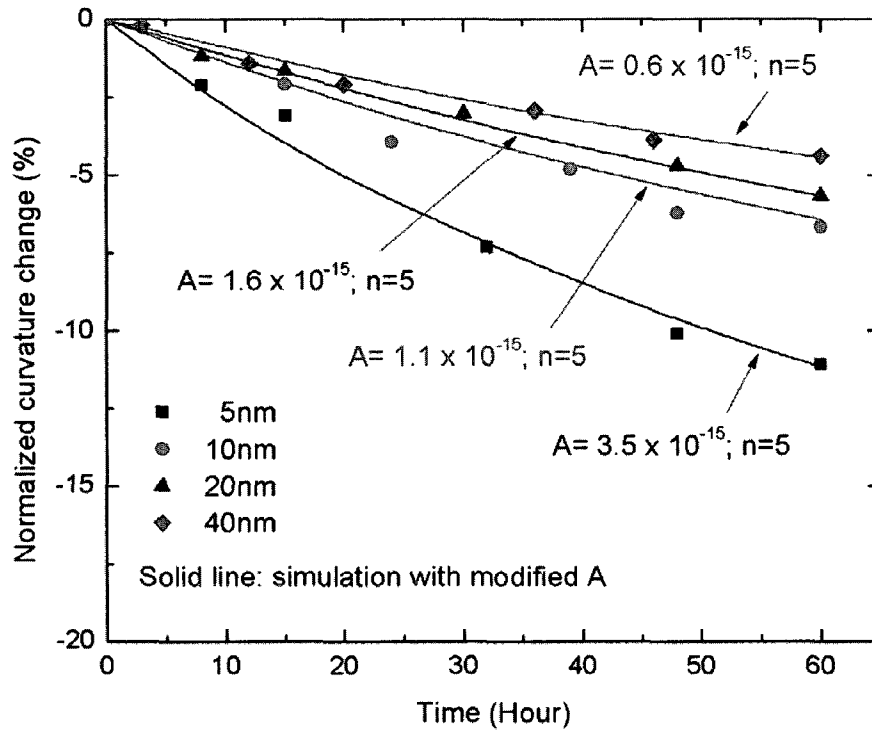
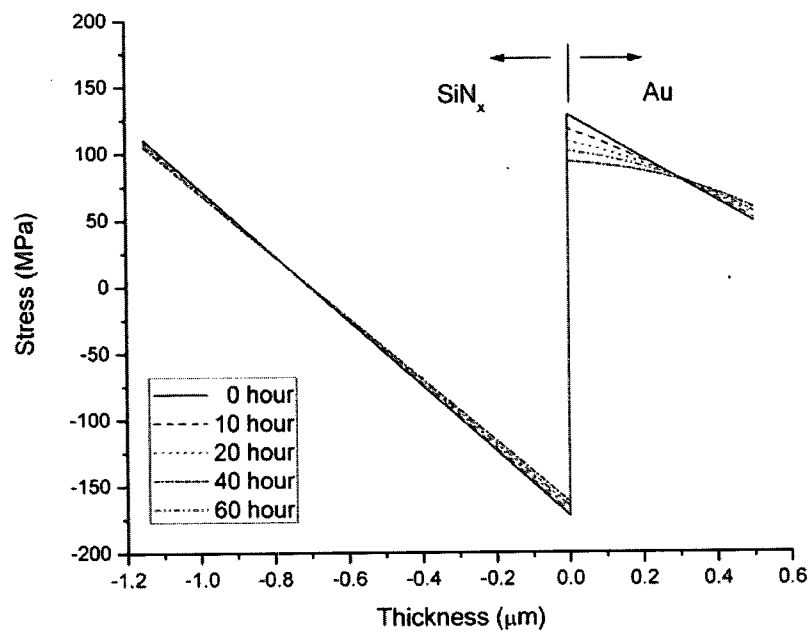
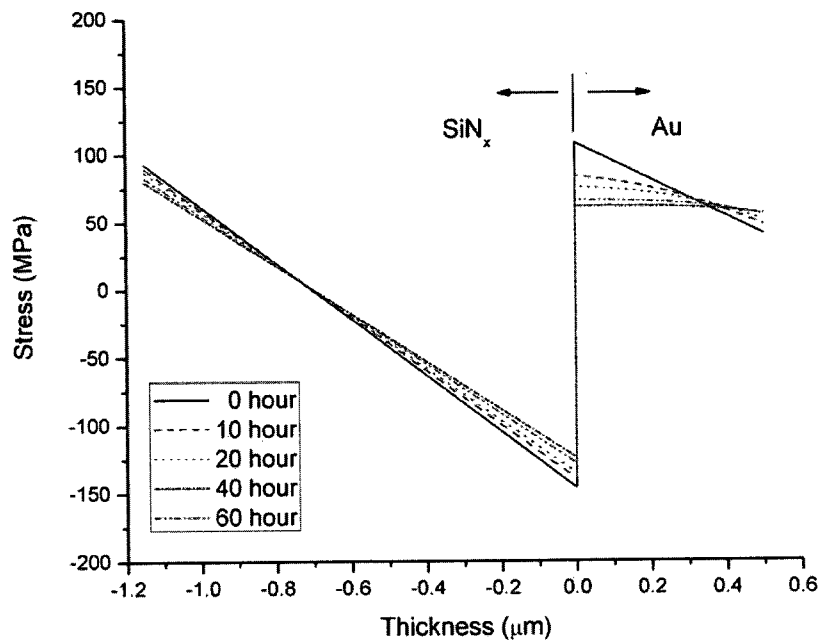


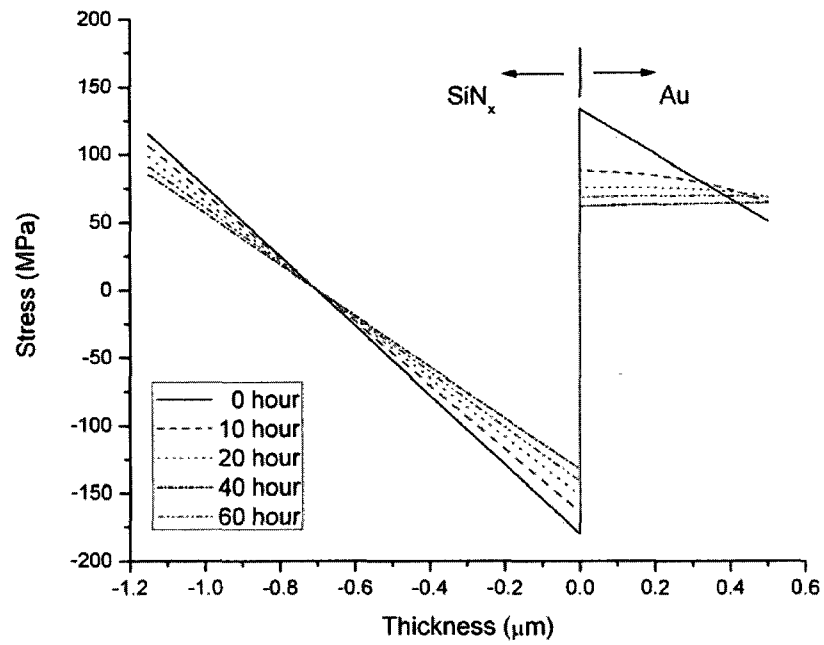
Fig. 6.5: Curvature evolution during the 60 hours isothermal holding at 150 °C for 5nm, 10 nm, 20nm and 40 nm ALD alumina coated microcantilever beams. The symbols represent experimental data while the solid lines represent simulation results.



(a)



(b)



(c)

Fig. 6.6: The stress distribution in both Au and Si₃N₄ layers of microcantilever beams for 0, 10, 20, 40 and 60 hour duration in isothermal holding at (a) 100 °C (b) 150 °C and (c) 200 °C.

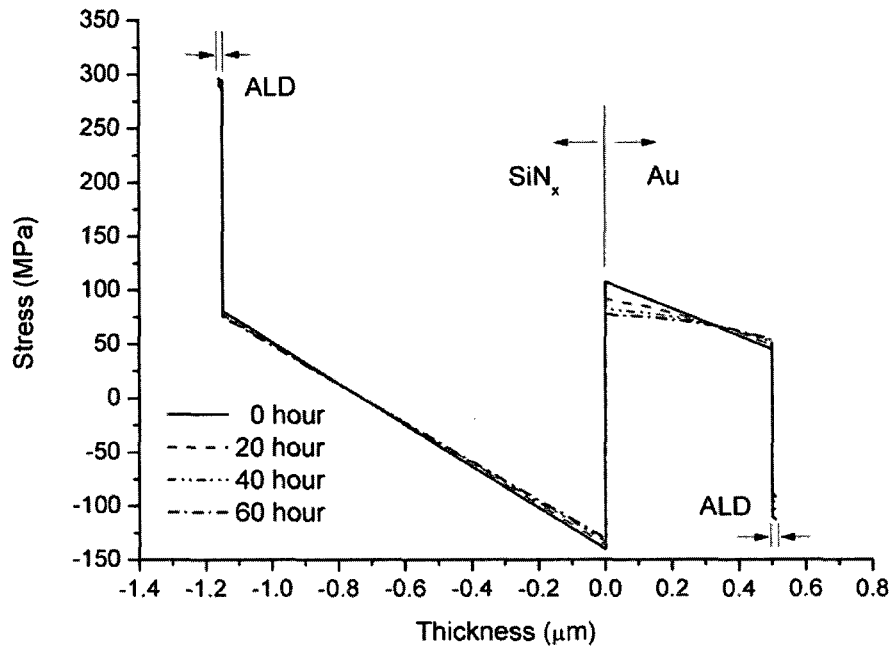


Fig. 6.7: The stress distribution in 10 nm ALD alumina, Au and Si₃N₄ layers of ALD coated microcantilever beams for 0, 10, 20, 40 and 60 hour duration in isothermal holding at 150 °C.

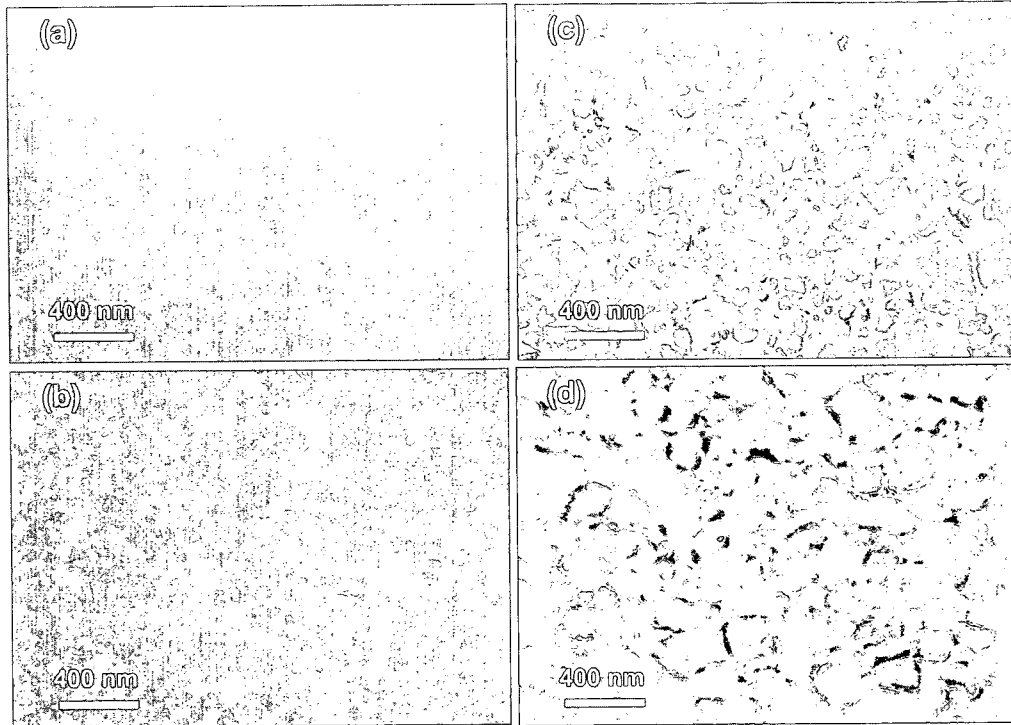


Fig. 6.8: SEM images of surface profiles on microcantilever beams (a) before and after 60 hours isothermal holding at (b) 100 °C, (c) 150 °C and (d) 200°C.

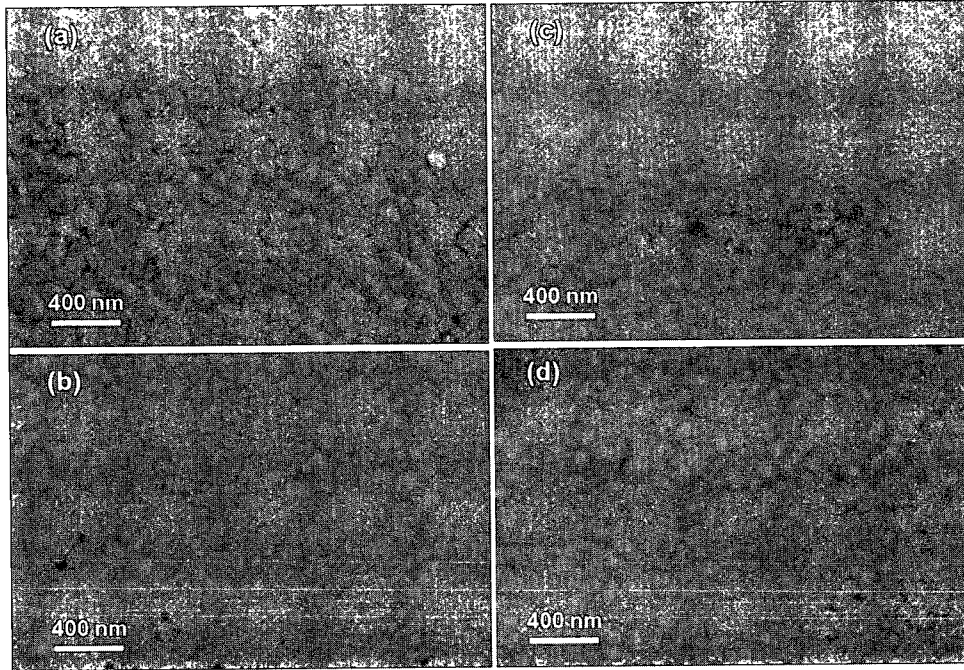


Fig. 6.9: SEM images of surface profile on (a) 5 nm, (b) 10 nm, (c) 20 nm and (d) 40 nm ALD alumina coated microcantilever beams after 60 hours of isothermal holding at 150 °C.

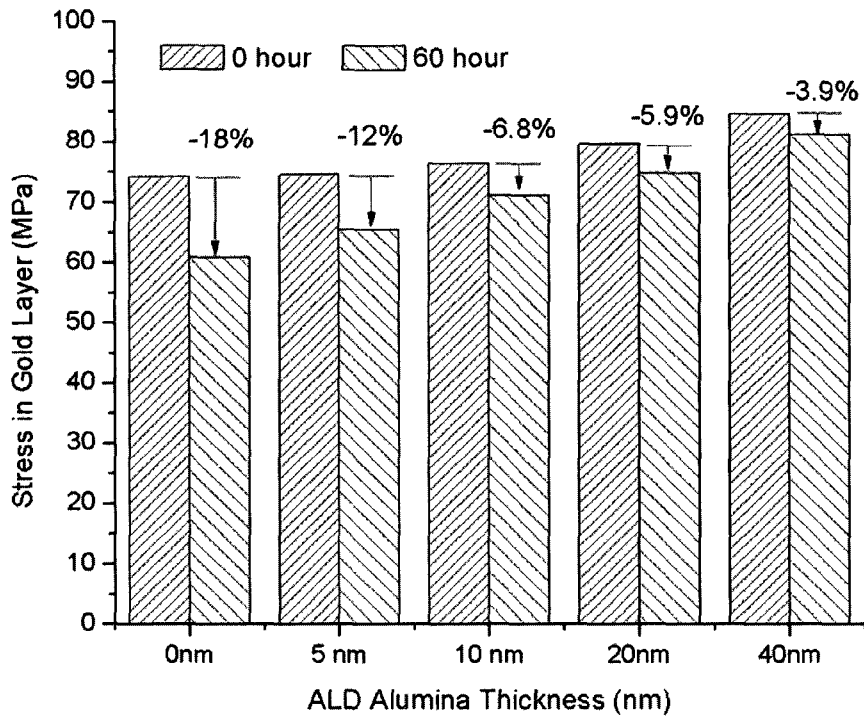


Fig. 6.10: The tensile stress decrease in Au layer after 150 °C isothermal holding in microcantilever beams with different ALD alumina thicknesses.

CHAPTER 7: COMPOSITE MATERIAL FOR IR ABSORBER

Silicon oxynitride (SiON) has been receiving a great deal of attention in microelectromechanical system (MEMS) integration due to its composition-dependent tunability of optical, electronic and mechanical properties. The SiON films are intended to replace the Si_3N_4 as a leading candidate for IR absorber in cantilever-based IR detectors. The wavelength of absorbance peaks of SiON can be tuned to match the blackbody radiation peaks of targets of interest, in order to improve the sensitivity of the IR detectors. However, study on mechanical behaviors of SiON films have not been reported in literature. In this work, the SiON films are fabricated, in order to study the material and mechanical properties by using EDX, FTIR and nanoindenter. These studies are performed to achieve a fundamental understanding required to design microcantilever-based IR detectors.

7.1. Introduction

Silicon oxynitride (SiON) has been under extensive investigation for over a decade as it is a promising material system for the development of optics, photonics and microelectronics applications. These applications vary to include waveguide devices, anti-reflective coating, nonvolatile memories and gate dielectrics (Worhoff et al., 1999; Melloni et al., 2003; Lien et al., 2000; Habermehl et al., 1999; Hattangady et al., 1996; Gusev et al., 1999). SiON demonstrates

unique tunability of optical and electronic properties when changing the chemical composition of oxygen and nitrogen, from silicon dioxide (SiO_2) to silicon nitride (Si_3N_4). For instance, the refractive index (n) can be varied from 1.47 (SiO_2) to 2.3 (Si_3N_4) (Gunning *et al.*, 1989), and the dielectric constant (ϵ) can be varied from 3.9 (SiO_2) to 7.8 (Si_3N_4) (Brown *et al.*, 1968). Furthermore, the residual stress can be transformed from compressive (SiO_2) to tensile (Si_3N_4) mode (Denisse *et al.*, 1986; Thurn *et al.*, 2004). This flexibility in mechanical properties allows SiON films with low residue stress and high thermal stability to be integrated into the microelectromechanical systems (MEMS) (Habermehl *et al.*, 2000; Rand and Roberts, 1973). In this paper, SiON is proposed to replace Si_3N_4 as a leading candidate of IR absorber in microcantilever-based IR detectors. The wavelength of absorbance peaks of SiON can be tuned to match the blackbody radiation peaks of targets of interest, in order to improve the sensitivity of the IR detectors. In addition, SiON not only provides the tunability in wavelength of absorbance peak, but also provides a large degree of freedom for the design of mechanical cantilever systems.

As an efficient thin film deposition process, plasma enhanced chemical vapor deposition (PECVD) has been widely employed to fabricate silicon oxynitride films. However, the PECVD deposited SiON films inevitably contain a significant amount of hydrogen incorporated in the Si-H, O-H and N-H bonding configuration. This inclusion is due to hydrogen precursors, such as silicon hydrochloride

(SiH_2Cl_2), silicon hydride (SiH_4) and ammonia (NH_3), used in the PECVD process (Denisse et al., 1986). Hydrogen incorporation greatly restricts the scope of achievable optical, electronic and mechanical properties of PECVD deposited SiON films. Therefore, a post-deposition annealing must be performed at temperatures above 850 °C to eliminate the hydrogen incorporation (Denisse *et al.*, 1986). However, such high temperature annealing results in large thermal induced stress in SiON films and is not compatible with MEMS and complementary metal-oxide-semiconductor (CMOS) processing. RF magnetron sputtering is a versatile technique that has been used to deposit thin films of a wide variety of materials. Compared with conventional PECVD SiON processes, the major advantage of RF magnetron sputtering of SiON is the elimination of the hydrogen incorporation, since there are no hydrogen precursors involved in the deposition. Additionally, RF magnetron sputtering can flexibly yet reliably control various characteristics of SiON films, such as microstructure and stoichiometry, to tune the specific properties of the films.

Time-dependent plastic deformation (creep) behavior is one of the critical issues related to the long-term reliability of MEMS devices, and worthy of extensive study and additional understanding. Although extensive research has been conducted on sputtered SiON films in microelectronic and optical applications, only a few attempts have been made to study their mechanical properties (Guimaraes *et al.*, 2001; Jozwik *et al.*, 2004; Alayo *et al.*, 2004). Furthermore, a

study on creep deformation behaviors of SiON films at room temperature has not been reported in literature. Depth-sensing nanoindentation is a powerful technique for studying the mechanical properties of materials in micro- or nano-scaled dimensions. By precisely recording the load-displacement data and constructing relevant analysis models, nanoindentation has been successfully used to reveal and interpret the mechanisms of various mechanical properties, including hardness, elastic modulus, creep and stress relaxation, etc (Oliver and Pharr, 1992, 2004).

In the present work, SiON films with different composition of oxygen and nitrogen content, ranging from silicon oxide to silicon nitride, are deposited by RF magnetron sputtering. Creep behaviors of sputtered SiON films have been investigated by depth-sensing nanoindentation with constant-load controlled experiments carried out at room temperature. Energy dispersive X-ray (EDX) spectroscopy and Fourier-transform infrared (FT-IR) spectroscopy are employed to characterize SiON films with respect to stoichiometric composition, types of chemical bonding and microstructures. A deformation mechanism based on chemical bonding structure and shear transformation zone (STZ) amorphous plasticity theory is proposed to interpret elastic and plastic mechanical properties of SiON films. The experimental procedures, results, analysis and interpretations presented in this paper are expected to provide valuable information for

fundamental understanding required to design microcantilever-based IR detectors.

7.2. Theoretical Background

7.2.1. Oliver-Pharr method

Building on the work of many other researchers (Oliver and Pharr, 1992), in 1992 Oliver and Pharr introduced a now-classic method for measuring hardness and elastic modulus by nanoindentation techniques. Since then, this method has been widely adopted to characterize the mechanical behavior of materials at small scales, while numerous changes and refinements have been made to further improve its accuracy (Oliver and Pharr, 2004). The schematic of a typical nanoindentation load-displacement (P-h) curve is shown in Fig. 2.10, with the important parameters labeled. The reduced modulus (E_r) can be obtained by fitting the initial unloading slope (S) from loading-displacement data to the equation:

$$E_r = \frac{\sqrt{\pi}}{2\sqrt{A(h_c)}} S \quad (7.1)$$

where $A(h_c)$ is the area function of the Berkovich tip, which is calibrated by a standard material such as the fused quartz, whose $E=72$ GPa and $\nu=0.170$. $S=dP/dh$ is defined as the slope of the upper portion of the unloading curve

during the initial stages of unloading. In practice, S is measured by first fitting the upper portion of unloading curve with a Power-law relation $P=\alpha (h-h_f)^m$, where α and m are fitting constants, and h_f is the measured final or permanent depth of penetration after the indenter is fully unloaded. E_r is defined as:

$$\frac{1}{E_r} = \frac{1-\nu_s^2}{E_s} + \frac{1-\nu_i^2}{E_i} \quad (7.2)$$

where the subscripts s and i represent the specimens and indenter, respectively. Young's moduli of SiON films can thus be derived from Eq. 7.2. For diamond indenter tips that are typically used, $E_i=1140$ GPa, and $\nu_i = 0.07$.

In addition, the hardness (H_f) of the SiON films can also be determined by:

$$H_f = \frac{P_{max}}{A(h_c)} \quad (7.3)$$

where P_{max} is the maximum indent load

7.2.2. Nanoindentation creep

For the steady-state time-dependent plastic deformation (or creep) in a uniaxial test, the relationship between the constant strain rate and applied stress can be described by an empirical equation:

$$\dot{\epsilon}_{ind.} = A\sigma^n \quad (7.4)$$

where $\dot{\epsilon}_{ind.}$ is the constant indentation strain rate, σ is the applied stress, n is defined as stress exponent of the Power-law creep, and A is a material-related constant (Poirier, 1985). This empirical equation is equally valid for the nanoindentation creep test with a self-similar indenter (Berkovich tip used in this study). The applied stress σ can be obtained as the average pressure under the indenter, or the indentation hardness:

$$\sigma = \frac{P}{A} \sim \frac{P}{h^2} \quad (7.5)$$

where A is the indenter area function as $A=F(h)$, P is the instantaneous indentation load and h is the instantaneous indentation displacement. However, due to the complex stress and strain involved in the nanoindentation test, the constant strain rate $\dot{\epsilon}$ could be substituted by an equivalent strain rate defined as:

$$\dot{\epsilon}_{ind.} = dh / dt \quad (7.6)$$

where h is the instantaneous indentation displacement and t is the indentation time (Hill, 1992; Storakers and Larsson, 1994). The indentation displacement

rate dh/dt during the creep period can be calculated by fitting the creep displacement-time curve within the constant load holding period with the following empirical law:

$$h(t) = h_0 + a(t - t_0)^b + ct \quad (7.7)$$

where h_0 and t_0 are defined as the initial indentation displacement and creep initiation time, respectively, and a , b and c are fitting constants (Li, 2004). In this study, h_c ($h_c = h - h_0$) and t_c ($t_c = t - t_0$) are used to represent the instantaneous creep displacement and creep time, respectively. By obtaining the equivalent strain rate $\dot{\epsilon}$ and applied stress σ from the nanoindentation data by using Eq. 7.5, Eq. 7.6 and Eq 7.7, the stress exponent n , which reveals the creep properties and mechanisms of the given materials, can be extrapolated from the slope of logarithm of $\dot{\epsilon}_{ind.}$ versus logarithm of σ curve ($\log(\dot{\epsilon}_{ind.}) - \log(\sigma)$) plotted from Eq. 7.4. The physical meaning of stress exponent will be discussed in detail in the section 7.4.4.

7.3. Experimental Procedure

Nanoindentation creep experiments of sputtered SiON films are conducted on a Triboindenter nanomechanical test system (from Hysitron Inc., Minneapolis, MN) using a constant-load controlled mode at room temperature. The indent load

resolution of the Triboindenter is 1 nN with a noise floor of 100 nN, and the indent displacement resolution is 0.02 nm with a noise floor of 0.2 nm. A standard Berkovich tip (from Hysitron Inc.) with a tip radius of approximately 150 nm and a half-angle of 65.35° are used in the experiments. The machine compliance calibration for the transducer-tip configuration and tip area function calibration are performed with a standard fused silica sample before proceeding with all indentation experiments.

7.3.1. Constant rate of loading (CRL)

Constant rate of loading (CRL) tests are performed on both the SiON thin film samples and the standard fused quartz sample in load-control mode, using constant loading rate and the same rate during unloading. The scheme of CRL is demonstrated in Fig. 7.1, in which the maximum indent load is 2 mN, and both constant loading rate and unloading rate are 400 $\mu\text{N/s}$. In all of the experiments, the maximum indentation depth is kept below 150 nm, or 15 % of the SiON film thickness of 1 μm , which avoid any influence of the substrate effects to the results (Bhattacharya and Nix, 1988).

7.3.2. Indentation load relaxation (ILR)

The scheme of Indentation load relaxation is demonstrated in Fig. 7.2, in which the maximum indent load is 2 mN, the holding period is 100 s, and both constant loading rate and unloading rate are 400 $\mu\text{N/s}$. For each SiON specimen, five

replications of the nanoindentation creep experiment are performed repeatedly with the same loading sequence. Thermal drift can induce large uncertainty and errors into the nanoindentation results. To minimize the thermal drift, thermal equilibrium needs to be reached in the isothermal enclosure of the Triboindenter for several hours before the indentation experiments are conducted. In addition, before each individual indentation is initiated, the Berkovich tip is first approached to the sample surface with a pre-loading force of 2 μN and held constant to monitor the thermal drift until a stable drift rate is reached. Compensation is then automatically applied to the indentation results by the Triboindenter.

7.4. Result and Discussion

7.4.1 Chemical and optical properties of SiON films

SiON films are investigated by EDX analysis to determine film composition. Fig. 7.3 shows the EDX spectra of individual SiON films. The corresponding element concentrations of Si, O and N in atomic percentages (at. %) are summarized in Table 7.1. The results of the EDX analysis indicate that all of the SiON films exhibit a Si-sufficient non-stoichiometric composition, which could be a result of oxygen and/or nitrogen byproducts formed in the sputtering process (Sandland, 2005). The small amount of oxygen (5.74 at.%) detected in the SiN_y film could be attributed to the absorption of free oxygen in the surface of the film, evidenced by the absence of absorbance peaks related to Si-O-Si bond in the FT-IR

spectrum of SiN_y film (Fig. 7.4).

According to the bulk phase diagram of the ternary Si-O-N system (Du *et al.*, 1989), Si₂ON₂ is the only crystalline and thermodynamically stable compound of silicon oxynitride. In such a stoichiometric Si₂ON₂ phase, every Si atom is present in a fourfold-coordinated form, as it is in stoichiometric SiO₂, where every O atom is twofold-coordinated with two Si atoms, and Si₃N₄ where every N atom is threefold-coordinated with three Si atoms. For non-stoichiometric amorphous SiO_xN_y films deposited by sputtering or PECVD, two models known as the random mixture model (RMM) and the random bonding model (RBM) have been proposed to depict the chemical bonding structures (Eriksson and Granqvist, 1986; Gritsenko *et al.*, 1998; Philipp, 1972; Sassella, 1993). The SiO_xN_y film with RMM structure is comprised of a random mixture of SiO₂ and Si₃N₄ in separate phases on a microscopic scale. In the SiO_xN_y film with RBM structure, Si atoms randomly bond with O and/or N atoms to form a homogenous O-Si-N network with five different tetrahedral coordinations, in which $y = 4 - x$, and x may vary from 0 to 4 (Eriksson and Granqvist, 1986; Gritsenko *et al.*, 1998; Philipp, 1972; Sassella, 1993).

Fig. 7.4 presents the normalized MIR FT-IR absorbance spectra of sputtered SiON films. The absence of resolvable Si-O-H bonds (around 3500 cm⁻¹), Si-H bonds (stretching mode at 2150-2200 cm⁻¹ and wagging mode at 900 cm⁻¹) or N-

H bonds (stretching mode at $3300\text{-}3400\text{ cm}^{-1}$ and bending mode at 1200 cm^{-1}) in FT-IR spectra indicate that the sputtered SiON films are free from hydrogen incorporation. Three characteristic features of Si-O-Si bonding group can be identified in the FT-IR spectrum of SiO_x film (Galeener, 1979; Lucovsky *et al.*, 1986; Sen and Thorpe, 1977). The strongest absorbance peak (with a shoulder) at approximately 1075 cm^{-1} is the Si-O stretching mode, in which the motion of oxygen atom is in the Si-O-Si bond plane with a direction parallel to the jointing line of two silicon atoms. The weakest absorbance peak near 810 cm^{-1} is the Si-O bending mode, in which the motion of oxygen atom is also present in the Si-O-Si bond plane, but with the direction along the bisector of the Si-O-Si bonding angle. The absorbance peak at 450 cm^{-1} is in the Si-O rocking mode, which results in the motion of oxygen atom being out of the Si-O-Si bond plane. In all Si-O variation modes, the motion of the silicon atom is in the opposite direction to that of the oxygen atom. In the FT-IR spectrum of the SiN_y film, the absorbance peaks of Si-N stretching mode near 840 cm^{-1} and wagging mode near 460 cm^{-1} are predominant spectral features (Tsu *et al.*, 1986).

The main absorbance peaks in the FT-IR spectra of three SiO_xN_y films continuously shift from that of SiN_y toward SiO_x as the content of nitrogen in the SiO_xN_y films decreases. The shape of the FT-IR spectrum of $\text{SiO}_x\text{N}_{y1}$ film largely resembles that of SiO_x , due to the low nitrogen concentration (5.60 at.%), while the spectra of both $\text{SiO}_x\text{N}_{y2}$ and $\text{SiO}_x\text{N}_{y3}$ films exhibit relatively broad

absorbance peaks. If the SiO_xN_y films are random mixtures of SiO_2 and Si_3N_4 phases according to the RBM structure, the absorbance peaks should be completely resolved into two separate spectral peaks of Si-O (1075 cm^{-1}) and Si-N (840 cm^{-1}) stretching modes. However, such peak deconvolution could not be accomplished for the absorbance peaks of these SiO_xN_y films, indicating that the broad absorbance peaks in SiO_xN_y FT-IR spectra are actually the combinations of overlapping peaks with different Si-O and Si-N variations in a possible Si-(O, N) random bonding environment. Therefore, the FT-IR results reveal that the SiO_xN_y films deposited by co-sputtering of silicon oxide and silicon nitride can be represented by the RBM structure constituted by one homogenous phase of a disordered O-Si-N network. The RBM structure is also proposed for SiO_xN_y films deposited by other deposition techniques, such as low-pressure chemical vapor deposition (LPCVD), electron-cyclotron resonance chemical vapor deposition (ECRCVD), PECVD and reactive sputtering (Sandland, 2005; Dreer and Wilhartitz, 2004; Scopel et al., 2003; Cova et al., 2005). It is important to note that the FT-IR spectra analysis might be more complicated due to the impacts from other film properties including density, residue stress, defects and substoichiometry.

7.4.2 Young's Modulus and indentation-hardness of SiON films

Prior to the nanoindentation creep experiments, regular constant-rate of loading nanoindentation tests (loading/unloading rate: $400\text{ }\mu\text{N/s}$) without the maximum

load (2 mN) holding period are performed on SiON films. Young's modulus and indentation-hardness are measured by fitting the unloading segment to an empirical Power-law relation (Oliver and Pharr, 1992, 2004). The load-displacement ($P-h$) curves of the nanoindentation on SiON films are shown in Fig. 7.5. The maximum indentation depth at the peak load of 2 mN in the SiON films is less than 150 nm, which counts for approximately 15 % of the film thickness ($\sim 1 \mu\text{m}$). Therefore, the effect of silicon substrate on the Young's modulus and indentation-hardness is negligible. In addition, the ratio of the final indentation depth h_f to the maximum indentation depth h_{max} (h_f/h_{max}) is less than 0.7, indicating that theoretically the "pile-up" is also negligible (Oliver and Pharr, 2004). The discrete displacement bursts, or "pop-ins", generally associated with structural changes in materials are not observed in the indentation loading segments.

As shown in Fig 7.6 and Table 7.2, both the calculated Young's modulus and indentation-hardness of SiON films increase with increasing nitrogen content ($N/(O+N)$) in film composition. Previous theoretical and experimental studies on amorphous silicon oxide and silicon oxynitride also conclude that the existence of Si-N bonds embedded in Si-O matrix tend to enhance Young's modulus and indentation-hardness approaching the values of silicon nitride (Kroll, 2005; Vila *et al.*, 2003; Vinci and Vlassak, 1996).

7.4.3 Nanoindentation creep analysis of SiON films

The load-displacement ($P-h$) curves of the nanoindentation creep on SiON films are shown in Fig. 7.7, and the corresponding creep displacement h_c ($h-h_0$) versus creep time t_c ($t-t_0$) curves (solid scatters) with respective fittings (solid lines) by Eq. 7.7 are shown in Fig. 7.8. It can be seen that Eq. 7.7 fits the h_c - t_c curves very well, with correlation coefficient $R^2 > 0.95$. Consistent with results of Young's modulus and indentation-hardness measurements (Fig. 7.6 and Table 7.2), the total creep displacement of SiON films decreases with increasing nitrogen content in film composition. As revealed by Fig. 7.8, the creep displacement rate $d(h_c)/d(t_c)$ decreases rapidly and achieves an approximate steady-state value with time.

During the creep period, the stress decreases with creep time due to the constant applied load and the increases in both creep displacement and contact area. Therefore, the stress exponents of SiON films, i.e. the slopes of all curves ($\partial \log(\dot{\epsilon}_{ind.})/\partial \log(\sigma)$), decline as stress decreases with creep time. However, it should be noted that for the SiO_x and high oxygen-containing SiON films (i.e. specimens SiO_xN_y1 and SiO_xN_y2) the stress exponents decline significantly from a large value (greater than 100) at the start of creep to a steady-state value less than 10 at the end of the creep period. On the other hand, for the SiN_y and high nitrogen-containing SiON films (i.e. specimen SiO_xN_y3) the stress exponents decrease relatively slowly, from a similar starting value to a final steady-state

value greater than 25. The change of stress exponents, which vary among the SiON films, suggests that different mechanical properties and deformation mechanisms are induced by the compositional variation in films.

7.4.4 Shear transformation zone (STZ) theory

The different nanonindentation creep behaviors observed in SiON films are interpreted by the shear transformation zone (STZ) theory of amorphous plasticity. The STZ theory is established based on the “free volume” model and “shear band” concept, and successfully extends to depict plastic deformation mechanisms for a wide range of amorphous materials (Argon, 1979; Falk and Langer, 1998; Langer, 2001; Spaepen, 1977). The “shear band” concept describes a microscopic region of localized plastic deformation under high levels of stress/strain rates. The formation of a shear band is associated with the shear transformation of a small volume of material consisting of atoms (tens of atoms at most) with a certain orientation, known as a basic shear unit, or the “shear transformation zone”. Therefore, the process of shear deformation of multiple STZs determines the characteristic of plastic flow, which is represented as the stress exponent n in Eq. 7.4. A large value of n indicates that the flow is inhomogeneous and is concentrated in a limited number and size of STZs. A small value of n then indicates a more homogenous and diffusional flow in plastic deformation. In the extreme case when n equals one, a completely Newtonian viscous flow would result. That is, the strain rate increases linearly with applied

stress.

Despite thermal annealing at 400 °C for 30 minutes, all SiON films that sputtered at room temperature are still largely amorphous, and inevitably contain defects, including structural voids and distorted (compressed or stretched) or defected (dangling or broken) bonds. The O-Si-O covalent bonds inside the Si-O tetrahedral structure have a fixed directional arrangement in bond angle (109°) and Si-O bond distance (1.61 Å). In comparison, the Si-O-Si bridging bonds connecting the tetrahedral units are flexible. Without inducing change in potential energy, the Si-O-Si bond angle (normally about 144°) can be varied from 110° to 160° , and the bond can also rotate freely around the Si-O axis. Although the silicon nitride shares a common tetrahedral structure with silicon oxide, the Si-N-Si bridging bonds connecting the silicon-nitrogen tetrahedral units are very rigid due to the necessity of nitrogen atoms forming three equivalent bonds to silicon atoms, rather than the two bonds in Si-O-Si. Furthermore, silicon nitride possesses a more dense packing structure than silicon oxide, providing fewer open channels than exists in the latter structure. Therefore, taking into account the characteristics of atomic bonding in the materials, the STZ clusters in sputtered SiON films upon nanoindentation creep are believed to consist of fundamental Si-O (for SiO_x), Si-N (for SiN_y) or O-Si-N (for SiO_xN_y with a RBM structure) tetrahedral units, which are bonded by the distorted and/or defected Si-O-Si and Si-N-Si bridging bonds.

As demonstrated in Fig. 7.9(a) to 7.9(e), at the beginning of the creep loading, the high level of stress results in an inhomogeneous plastic flow with a large stress exponent in all SiON films. When the applied stress exceeds the threshold stress, individual STZ clusters under the indenter containing Si-O, Si-N or O-Si-N tetrahedral units are collectively activated and start to move. This localized atomic-scale shear transformation further leads to rapid interaction, propagation and rearrangement among the nearby STZs, as well as the coalescence of adjacent free volumes. Consequently, relatively large shear bands of STZs with accumulated free volume are produced. As a result, a mechanical softening in materials occurs as the average applied stress into the materials is reduced due to formation of shear bands and increases in free volume. For the amorphous SiO_x film, the relatively flexible Si-O-Si bridging bonds and less dense packing Si-O structure could attribute to the formation of numerous shear bands to accommodate the applied stress and strain. The stress exponent gradually declines to a steady-state value, indicating that a more homogeneous flow is eventually reached. However, for the amorphous SiN_y film, some activated STZs may be blocked by the rigid Si-N-Si bridging bonds in movement. Therefore, few shear bands are produced in SiN_y film through STZ propagation, resulting in a more localized and less homogeneous flow, when compared to that in the SiO_x film. Such deformation mechanisms can be applied to the three SiO_xN_y films with an RBM structure. An increase in nitrogen content is accompanied by nitrogen atoms incorporated substituting oxygen atoms in both O-Si-N tetrahedron and Si-

O-Si bridging bond, thus increasing the Si-N-Si bridging bonds. Therefore, the SiO_xN_y films (SiO_xN_y1 and SiO_xN_y2) with low nitrogen content exhibit creep behaviors similar to that of the SiO_x film, while the SiO_xN_y film (SiO_xN_y3) with high nitrogen content and the SiN_y film demonstrate a similar creep response upon the nanoindentation.

For some materials such as metallic glasses, rapid strain accommodation by shear bands can sometimes result in measurable discrete signals of displacement burst (“pop-in”) during the indentation loading (Schuh and Nieh, 2004). In this work, no distinct displacement bursts are observed in nanoindentation creep experiments for any SiON films. The absence of displacement bursts could imply that numerous small shear bands of STZs can be formed in sputtered SiON films instantly and continuously, leading to more homogenous plastic flows and deformations compared with metallic glasses. Discrete displacement bursts are not detected by the same Triboindenter in the previous nanoindentation study on PECVD deposited silicon oxide films using various loading rates ranging from 10 to 1000 of $\mu\text{N/s}$ (Cao and Zhang, 2006, 2007)

7.5 Conclusions

In this chapter, the SiON films are fabricated to study the material and mechanical properties by using various techniques, in order to achieve a

fundamental understanding required to design of MEMS-based IR detectors. Broadly speaking, the contribution of this study is identifying effective means for engaging the composite material system and engineering mechanics in work important to continuing advancements in MEMS technology. Amorphous SiON films with varying oxygen and nitrogen content ranging from SiO_x to SiN_y are deposited by RF magnetron sputtering. FT-IR analysis reveals that the SiO_xN_y films deposited by co-sputtering silicon oxide and silicon nitride are composed of one homogeneous phase of random bonding O-Si-N network, i.e. a structure interpreted by the RBM. Nanoindentation creep experiments on sputtered SiON films are conducted to investigate the time-dependent plastic deformation in the films at room temperature. The measured Young's modulus and indentation-hardness of SiON films increase as the nitrogen content ($\text{N}/(\text{O}+\text{N})$) increases in film composition. The creep behaviors of SiON films also illustrate a strong correlation with composition of oxygen and nitrogen. Upon nanoindentation creep, the plastic flow in high oxygen-containing SiON films (with a smaller value stress exponent) is more homogeneous than that of high nitrogen-containing SiON films (with a larger value stress exponent). A deformation mechanism established on the chemical bonding structure and STZ amorphous plasticity theory is proposed to explain the observed variations in creep response of SiON films.

Table 7.1: Sputtering RF power applied in SiON film deposition, and corresponding atomic concentration of Si, O and N in film composition.

Specimen	RF Power (W)		Atomic Concentration (at. %)			
	SiO ₂	Si ₃ N ₄	Si	O	N	N/(O+N)
SiO _x	300	0	37.34	62.66	0	0
SiO _x N _y 1	300	100	51.23	43.17	5.60	11.48
SiO _x N _y 2	300	300	41.39	32.36	26.25	44.79
SiO _x N _y 3	100	300	42.44	22.24	35.32	61.36
SiN _y	0	300	46.04	5.74 *	48.23	100

* Free oxygen absorbed in the surface of SiN_y film.

Table 7.2: Young's modulus and indentation-hardness of the SiON films.

Specimen	Young's Modulus, E (GPa)	Hardness, H (GPa)
SiO _x	73.01	8.32
SiO _x N _y 1	125.09	12.50
SiO _x N _y 2	130.75	13.83
SiO _x N _y 3	156.67	15.78
SiN _y	166.13	17.10

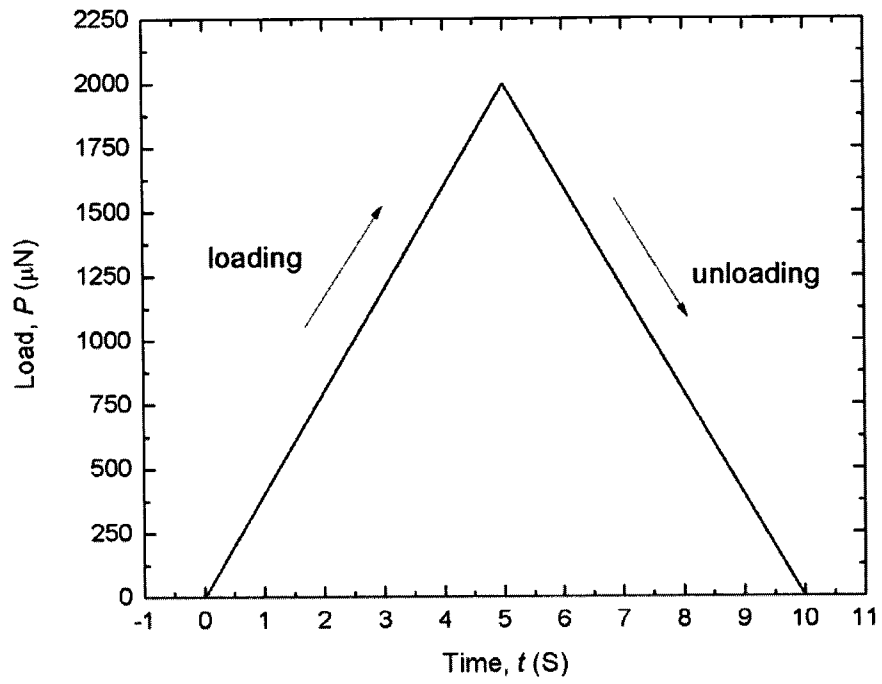


Fig. 7.1: Load scheme of the constant rate of loading (CRL) experiment for the SiON films.

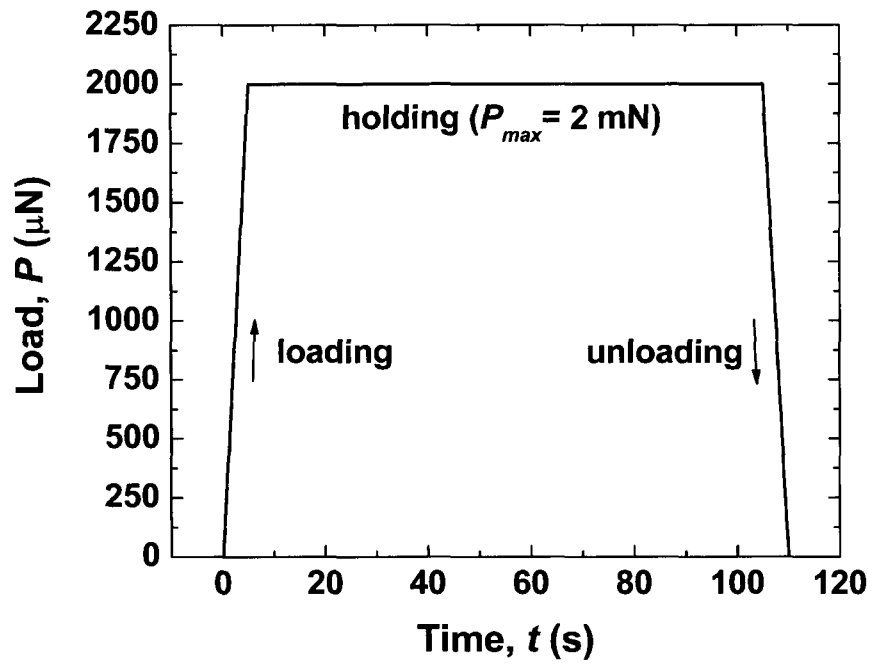


Fig. 7.2: Load scheme of the indentation load relaxation (ILR) experiment for the SiON films.

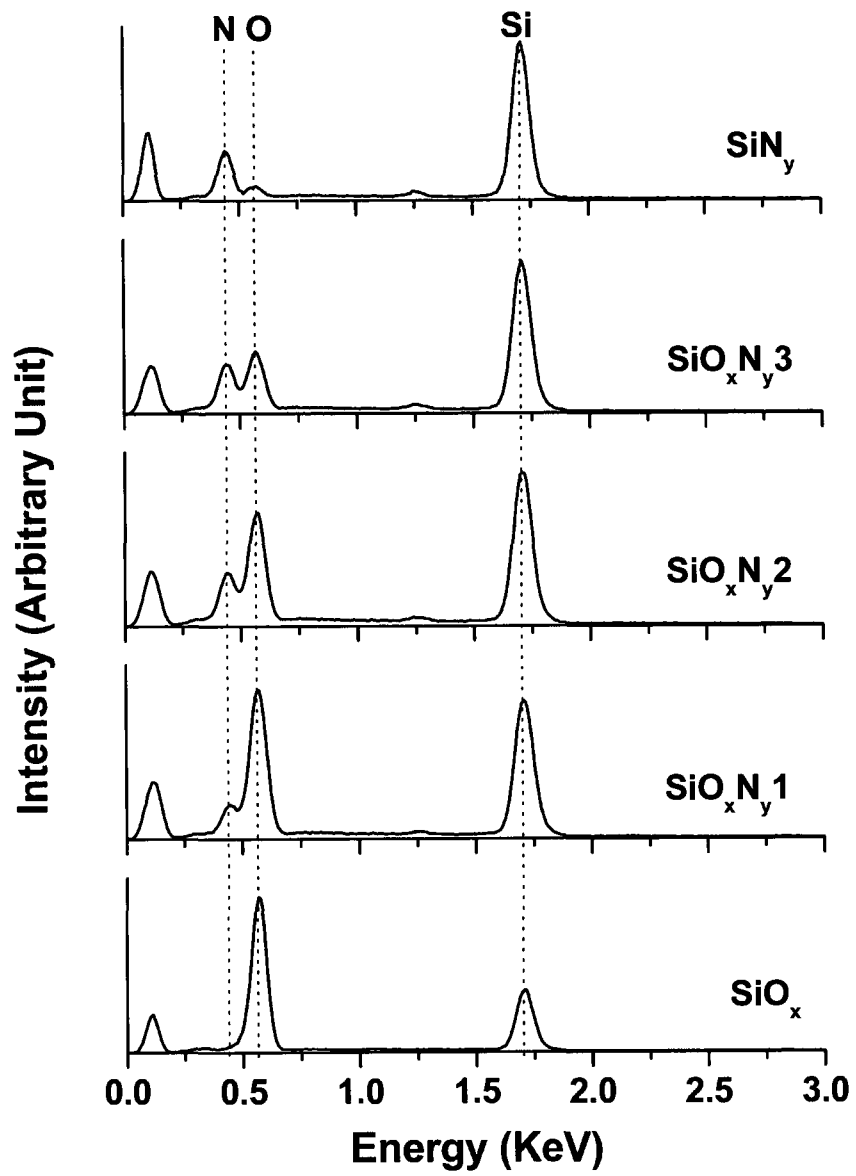


Fig. 7.3: EDX spectra of the SiON films.

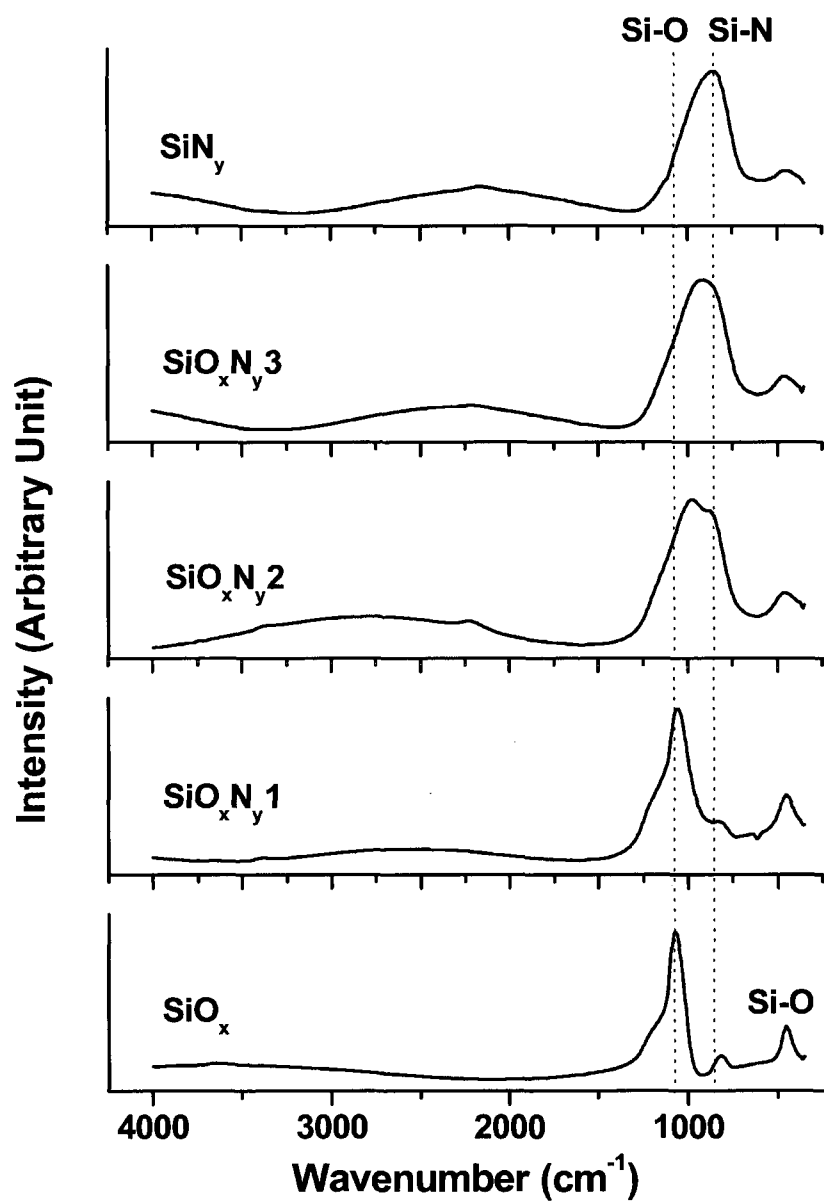


Fig. 7.4: MIR FT-IR absorbance spectra of the SiON films.

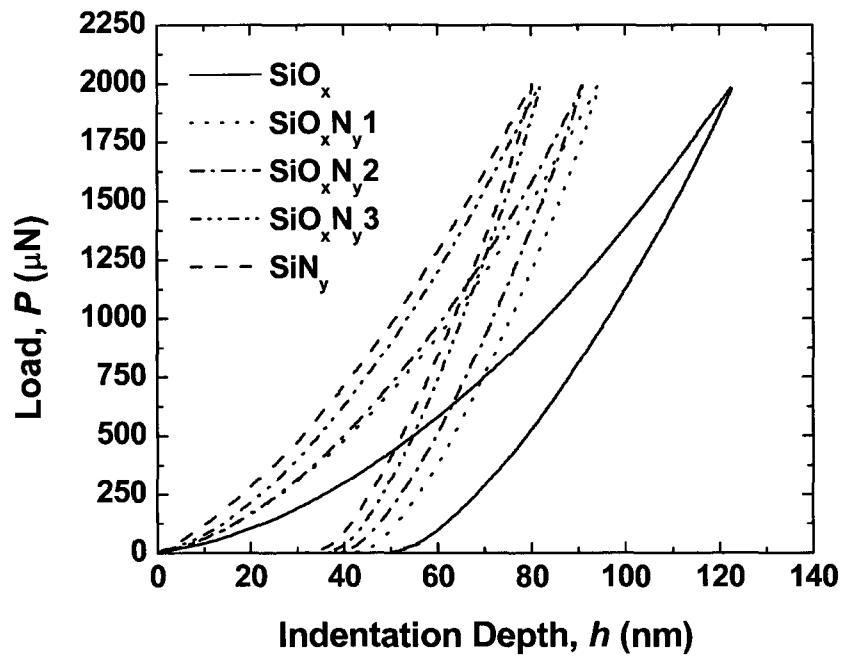


Fig. 7.5: Load-displacement (P - h) curves of the SiON films in the constant rate of loading nanoindentation experiments.

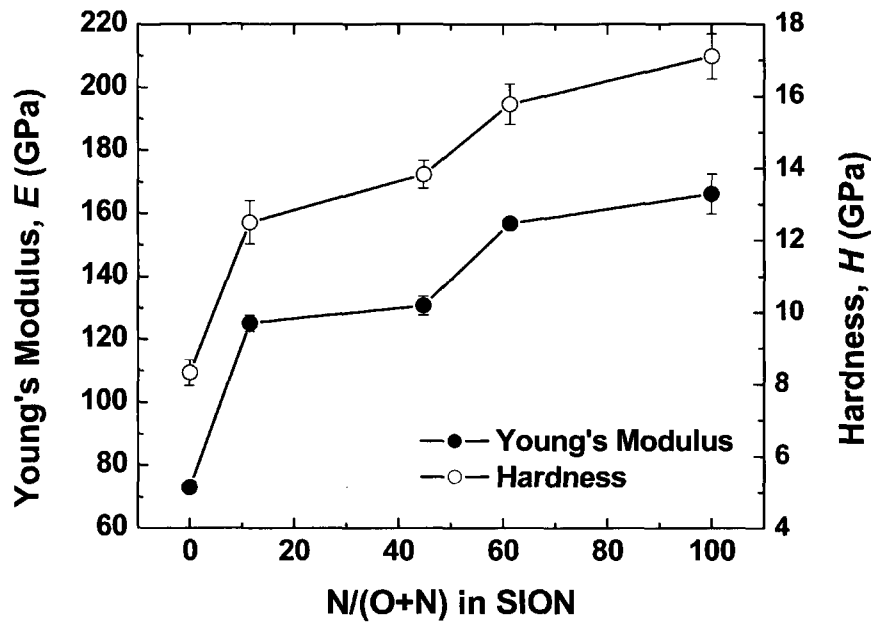


Fig. 7.6: Young's modulus and indentation-hardness of the SiON films as a function of the nitrogen content ($N/(O+N)$).

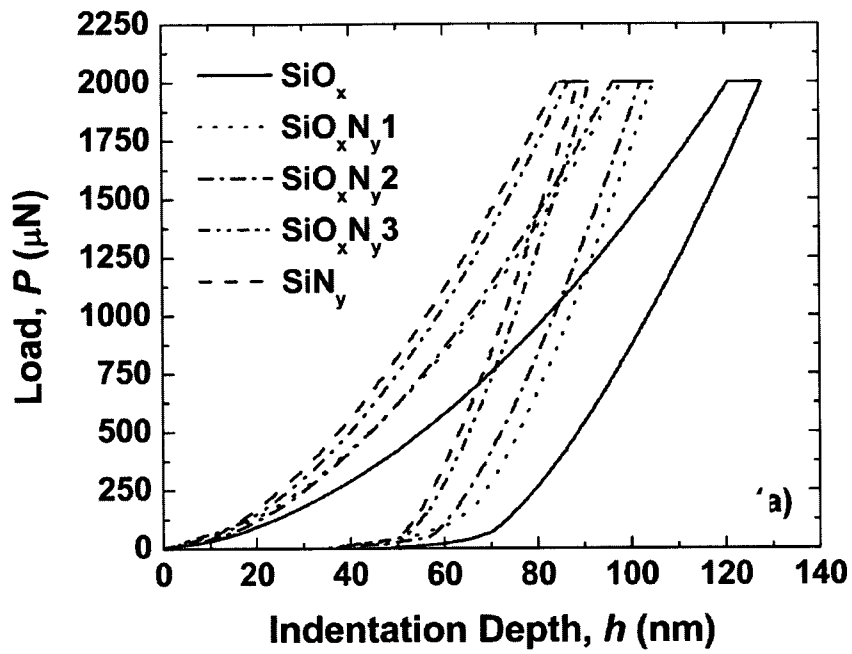


Fig. 7.7: Load-displacement (P - h) curves of nanoindentation creep on the SiON films.

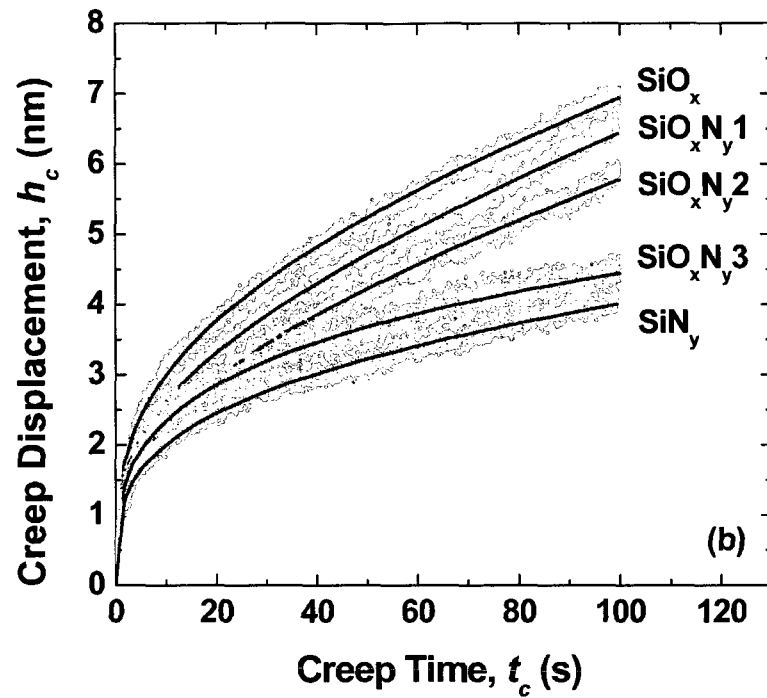
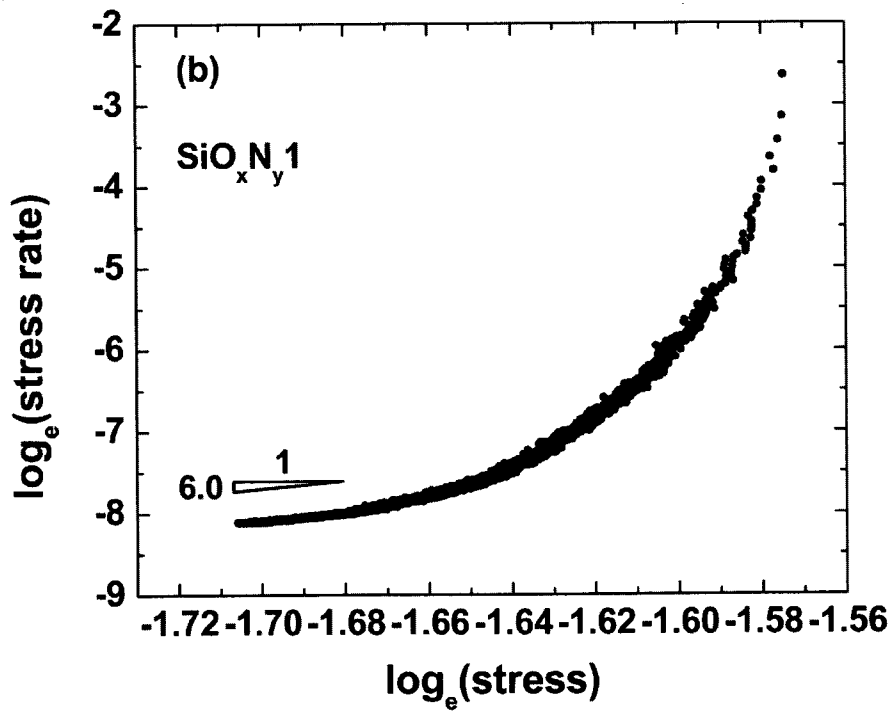
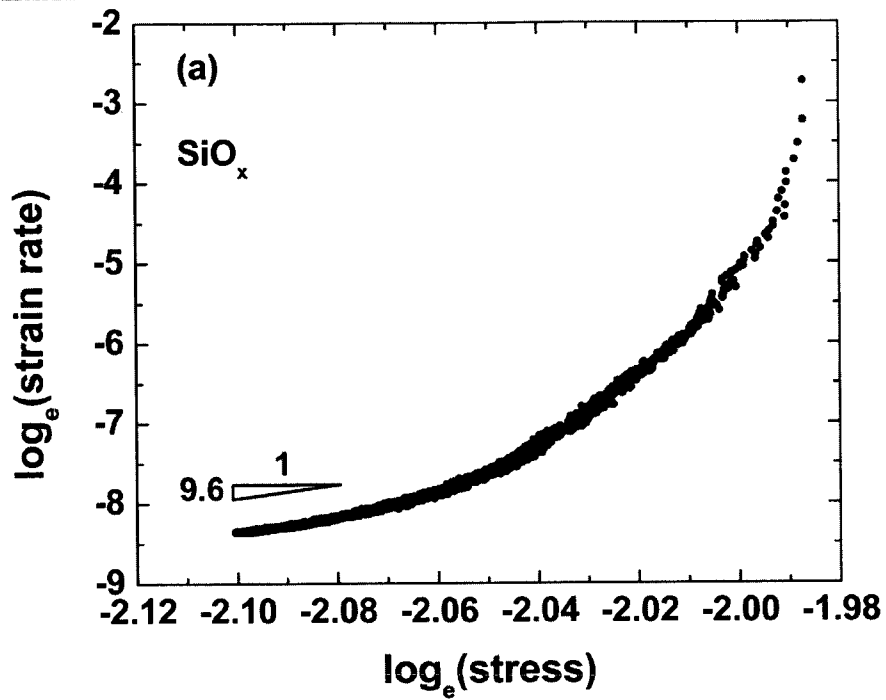
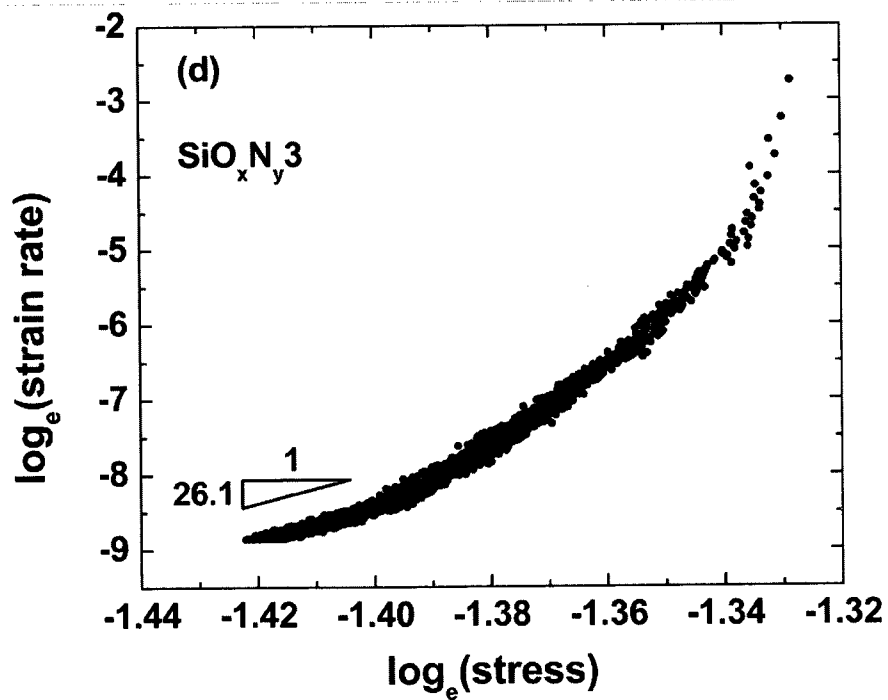
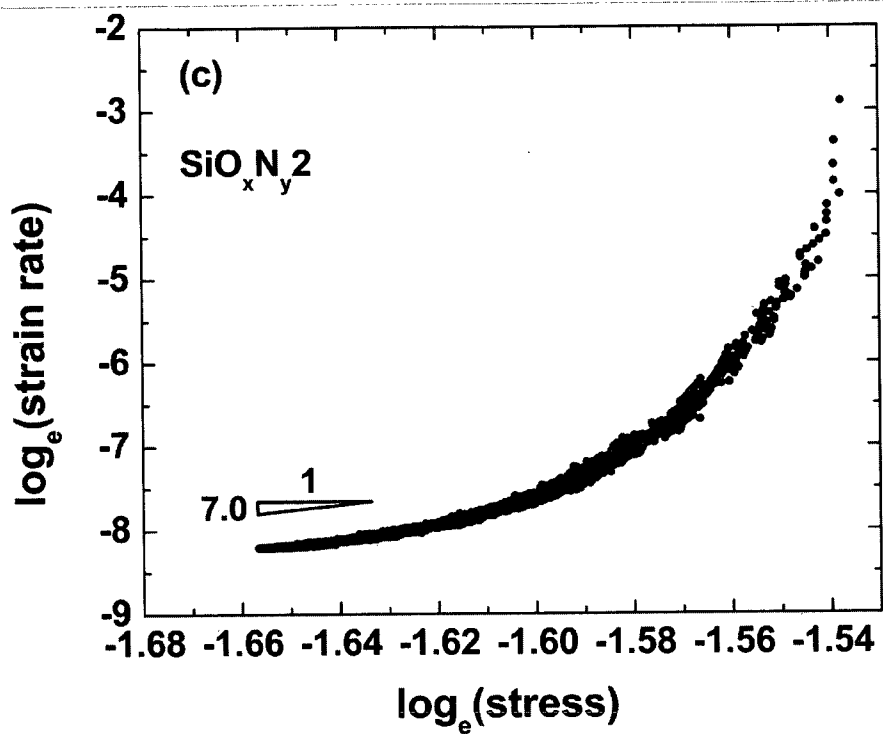


Fig. 7.8: Creep displacement h_c ($h-h_0$) versus creep time t_c ($t-t_0$) curves (solid scatters) with corresponding fittings (solid lines) of nanoindentation creep on the SiON films.





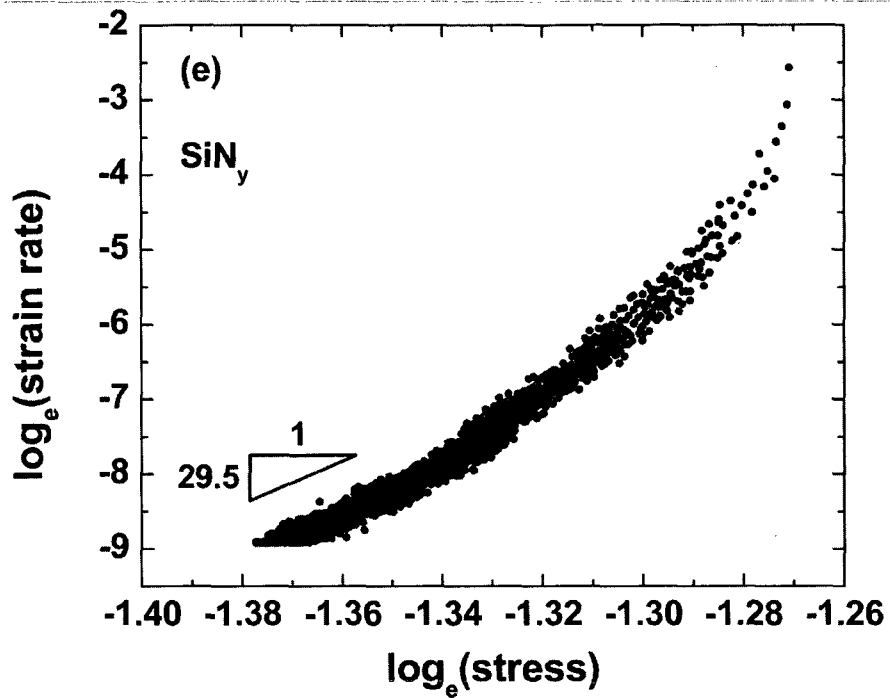


Fig. 7.9: Logarithm relations of strain rate and applied stress in nanoindentation creep for the SiON films: (a) SiO_x; (b) SiO_xN_y1; (c) SiO_xN_y2; (d) SiO_xN_y3 and (e) SiN_y.

CHAPTER 8: CONCLUSIONS AND RECOMMENDATIONS FOR FUTURE WORK

8.1. Summary

This dissertation advances three critical technical issues for next-generation high-sensitivity and tunable MEMS-based IR detectors: 1) planarization, 2) long-term behavior prediction of $\text{Si}_3\text{N}_4/\text{Al}$ bilayer microcantilevers and 3) mechanical and material properties characterization of silicon oxynitride (SiON) thin films. This research provides a comprehensive mechanical and material characterization of the temperature- and time-dependent thermomechanical responses of the $\text{Si}_3\text{N}_4/\text{Al}$ bilayer microcantilever beam under different thermal loading. Also, experimental methodologies and theoretical models for data analysis are developed for this structure. The results of thermal cycling are used to flatten the bilayer microcantilevers, and the results of isothermal holding are used to develop an FEA model. The validated FEA model is ultimately utilized to determine the temperature- and time-dependent deformation of MEMS-based IR detectors in short- and long-term operation. In addition, the mechanical and material properties of the silicon oxynitride thin films are systemically studied using indentation technique for mechanical characterization, Energy Dispersive X-ray analysis (EDX) for material composition and Fourier Transform Infrared spectrometer (FT-IR) for optical characterization.

These experiments, introduced in Chapter 2 and discussed in detail in Chapter 3 through Chapter 6, reveal various interesting and distinctive characteristics of the mechanical behaviors of the bilayer microcantilever structures, and the composite material for each of them are analyzed in depth.

More specifically, five major topics are covered in these chapters:

- 1) **Understand the thermomechanical evolution during cyclic thermal loading of bilayer microcantilever beams (Chapter 3).** The general behavior of the bilayer microcantilever beams when subjected to cyclic thermal loading is characterized with both linear thermoelastic and inelastic regions during cyclic thermal loading.
- 2) **Understand and characterize the creep and stress relaxation behaviors of bilayer microcantilever beams (Chapter 4).** Time-dependent deformation and creep parameters during isothermal holding at various temperatures are fully characterized by a Power-law model.
- 3) **Develop the finite element analysis (FEA) model to simulate and predict the thermomechanical behavior of bilayer microcantilevers (Chapter 4).** The temperature- and time-dependent deformations are

analyzed using FEM with characterized material properties from topics 1 and 2.

- 4) **Improve the planarity and reliability of MEMS-based IR detectors (Chapter 5).** The thermal cycling technique developed in topic 1 and the FEA model developed in topic 3 are employed to flatten the IR detectors and simulate the deformation during long-term operation.

- 5) **Understand the isothermal creep and stress relaxation behaviors in multilayer microcantilevers with nano-coatings (Chapter 6).** Inelastic deformation during isothermal holding at various temperatures will be fully characterized via an *in-situ* full field deformation measurement. The effects of nano-coatings on the thermomechanical responses will be investigated.

- 6) **Systemically study the mechanical behavior, including time-dependent/independent plasticity of composite thin film materials, for IR absorber using indentation testing (Chapter 7).** Particularly, the SiON thin films with tunability in the IR absorption spectrum, which has potential applications in IR detectors, are tested.

8.2 Contributions

Although motivated by the MEMS-based IR detectors, this thesis primarily focuses on contributing to the fundamental scientific understanding of the mechanical behavior of $\text{Si}_3\text{N}_4/\text{Al}$ bilayer microcantilevers and SiON composite materials. A broad range of related topics is covered, including temperature- and time-dependent deformation mechanism, curvature control, FEA model development, and elastic/plastic properties of thin films. To summarize, the major contributions of this thesis encompass the following three aspects:

- 1) The outcome of this thesis presents a comprehensive characterization of the temperature- and time-dependent thermomechanical responses of the bilayer microcantilevers under different thermal conditions.
- 2) Both experimental methodologies and FEA models developed in this dissertation can be readily applied to a wide variety of bilayer microcantilever structures for various applications.
- 3) The indentation procedures, results, analysis and interpretations of the composite material also provide valuable information that will increase the fundamental understanding required to design highly sensitive and tunable MEMS-based IR detectors.

8.3. Recommendations for Future Work

The experimental methodologies and theories in this dissertation establishes a preliminary framework under which future researchers can continue to systematically study other issues related to the development MEMS-based IR detectors. To conclude this dissertation, A few specific topics are recommended that promise to be particularly intriguing for future research:

- 1) **Further material characterization and sophisticated modeling of time-dependent deformation.** Although the results in Chapter 3 and 4 show the feasibility and importance of FEA model development, further material characterization and sophisticated modeling are necessary to improve the Power-law creep and the prediction of thermomechanical deformation. For example, most of the MEMS-based IR detectors operate at low temperature; hence, the material characterization of Al at 25, 50, and 75 °C is desired.
- 2) **Thermomechanical characterization in a vacuum chamber.** The environmental and experimental controls can be further improved to reduce the large scatter in experimental data, likely due to the humidity and temperature fluctuations during testing.
- 3) **Improving the array uniformity of MEMS-based IR detectors.** The array uniformity is a very important issue in the IR community. However, nonuniformity issues still exist and will remain to be a challenge in this work (Fig. 5.6). The array uniformity highly depends on the quality and process

parameters during fabrication, for example, the thickness nonuniformity of Si_3N_4 caused by the fluid dynamics of N_2 flow during PECVD. This would result in nonuniformity in residual stress/strain and, thus, curvature. In order to improve the quality, extensive trial and error work or parameter tuning is needed.

- 4) **Fracture mechanism in the composite thin films.** In this dissertation, the RF magnetron sputter was employed to deposit silicon oxynitride (SiON) thin films. Thereafter, rapid thermal anneal (RTA) was used to enhance the interface of film-film and film-substrate, and densify silicon oxynitride thin films. However, the RTA-induced microstructure change in silicon oxynitride thin films may influence the mechanical properties including Young's modulus, hardness, residual stresses, delamination and fracture toughness. The thermal-induced mechanical behavior changes of silicon oxynitride thin films after various RTA temperatures, which have not been reported previous in the literatures, can be explored by indentation techniques, including nanoindentation and Vickers indentation for mechanical and fracture characterization, respectively.

Appendix A: ABAQUS PROGRAM FOR BILAYER MICROCANTILEVER BEAMS

```
*NODE, SYSTEM=R
1, 0, 0, 0
41, 0, 20E-3, 0
9001, 90E-3, 0, 0
9041, 90E-3, 20E-3, 0
*NGEN, NSET=IN
1, 41, 1
*NGEN, NSET=OUT
9001, 9041, 1
*NFILL, NSET=ALLNODES
IN, OUT, 180, 50
*ELEMENT, TYPE=S8R
1, 1, 101, 103, 3, 51, 102, 53, 2
*ELGEN, ELSET=THIN SHELL1
1, 20, 2, 1, 90, 100, 20
*SHELL SECTION, ELSET=THIN SHELL1, COMPOSITE
0.2E-3, 3, AL
0.2E-3, 3, SI3N4
** thickness=0.2 um integrate point= 3 or 5 or 7
*MATERIAL, NAME=AL
*ELASTIC, TYPE=ISOTROPIC
70E3, 0.3
** young's modules
*EXPANSION, TYPE=ISO
23E-6
```

```

*Creep, Law=time
9E-15, 5.3
**A, n
*MATERIAL, NAME=SI3N4
*ELASTIC, TYPE=ISOTROPIC
254E3, 0.2
*EXPANSION, TYPE=ISO
2.1E-6
*NSET, NSET=FIXED, GEN
1, 41, 1
*NSET, NSET=MID, GEN
21, 9021, 250
*NSET, NSET=ALLNODE, GEN
1, 9041, 1
*****
*****
*BOUNDARY
FIXED, ENCASTRE
** encastre= fix all degree freedom
*****
*****
*INITIAL CONDITIONS, TYPE=TEMPERATURE
ALLNODE, 0
*****
*STEP, NLGEOM, INC=1000000
*STATIC
0.01, 1., 1e-15, 0.05
*TEMPERATURE
ALLNODE, 140

```



```
*NODE PRINT,NSET=MID,FREQUENCY=100000
COORD,U3
*END STEP
**
** STEP:creep
**
*Step, inc=2000000
*Visco,cetol=1.E-4,STABILIZE
1.e-6,45, 1.e-15,1
*Restart, write, frequency=1
*NODE PRINT,NSET=MID,FREQUENCY=1
COORD,U3
*End Step
```

Appendix B: ABAQUS PROGRAM FOR MEMS-BASE IR DETECTORS

SDRC I-DEAS ABAQUS FILE TRANSLATOR 28-Jan-07 01:18:35

*NODE, NSET=ALLNODES, SYSTEM=R

```

1, 3.0000000E+00, 5.0000000E+01, 4.0000000E-01
2, 3.0000000E+00, 0.0000000E+00, 4.0000000E-01
3, 2.8500000E+01, 5.0000000E+01, 4.0000000E-01
4, 0.0000000E+00, 5.3000000E+01, 4.0000000E-01
5, 0.0000000E+00, 0.0000000E+00, 4.0000000E-01
6, 6.0000000E+00, 1.0000000E+02, 4.0000000E-01

```

```

⋮      ⋮      ⋮      ⋮

```

```

8955, 3.9220137E+01, 7.9813370E+01, 4.0000000E-01
8956, 3.9480268E+01, 7.8497568E+01, 4.0000000E-01
8957, 3.9859202E+01, 7.8013634E+01, 4.0000000E-01
8958, 3.9411009E+01, 7.7563918E+01, 4.0000000E-01
8959, 3.9805214E+01, 7.7045465E+01, 4.0000000E-01
8960, 3.9041499E+01, 7.8134061E+01, 4.0000000E-01

```

*ELEMENT, TYPE=S8R , ELSET=THIN SHELL1

```

1, 12, 1, 640, 1863, 13, 1867, 1866, 1869
2, 161, 734, 743, 1, 1868, 1871, 1870, 160
3, 1, 743, 740, 640, 1870, 1873, 1872, 1867
4, 3, 60, 1562, 519, 63, 1875, 1874, 518
5, 2, 164, 693, 65, 167, 1877, 1876, 62
6, 162, 5, 271, 692, 163, 270, 1879, 1878

```

```

      |      |      |      |      |      |      |      |      |
2779, 5482, 5479, 5495, 5498, 7582, 7583, 7584, 7587
2780, 5485, 5483, 5482, 5481, 6421, 7585, 7586, 7431
2781, 5481, 5482, 5498, 5497, 7586, 7587, 7589, 7435
2782, 5491, 5492, 5506, 5520, 7564, 7425, 7588, 7591
2783, 5494, 5491, 5520, 5532, 7568, 7591, 7590, 7593
2784, 5493, 5494, 5532, 5542, 7572, 7593, 7592, 7595
*NMAP,TYPE=RECTANGULAR,NSET=ALLNODES
0,0,0

1E-3,1E-3,1E-3
*SHELL SECTION,ELSET=THIN SHELL1 ,COMPOSITE
  0.2E-3,3,SI3N4
  0.2E-3,3,AL
** thickness=0.2 um   integrate point= 3 or 5 or 7
*MATERIAL,NAME=AL
*ELASTIC,TYPE=ISOTROPIC
  70E03,0.3
** young's modules
*EXPANSION,TYPE=ISO
  23E-6
*Creep,Law=time
  5.8E-20,5.3
*MATERIAL,NAME=SI3N4
*ELASTIC,TYPE=ISOTROPIC
  254E03,0.2
*EXPANSION,TYPE=ISO

```

```

2.1E-6
*NSET,NSET=F
2,5,163,162,165,164,167,
4490,4750,4749,4752,4751,4754,4487
*NSET,NSET=L1,GEN
423,519,2
*NSET,NSET=L2
3,9,
*NSET,NSET=L
L1,L2
*NSET,NSET=ALLNODE,GEN
1,8960,1
*****
*****
*BOUNDARY
F,ENCASTRE
** encastre= fix all degree freedom
*****
*****
*INITIAL CONDITIONS, TYPE=TEMPERATURE
ALLNODE,0
*****
*STEP,NLGEOM,INC=1000000
*STATIC
0.001, 1., 1e-15, 0.05
*TEMPERATURE
ALLNODE,20
*NODE PRINT,NSET=L,FREQUENCY=100000
COORD,U3

```

```
*END STEP
**
** STEP:creep
**
*Step, inc=2000000
*Visco,cetol=1.E-4,STABILIZE
1.e-6,2000, 1.e-15,1
*Restart, write, frequency=1
*NODE PRINT,NSET=L,FREQUENCY=1
COORD,U3
*End Step
```

BIBLIOGRAPHY

Abermann R, Koch R and Kramer R 1979 Electron-microscope structure and internal-stress in thin silver and gold-films deposited onto MgF₂ and SiO₂ substrates. *Thin Solid Films* 58 365-70

Abermann R, Kramer R and Maser J 1978 Structure and internal-stress in ultrathin silver films deposited on MgF₂ and SiO₂ substrates. *Thin Solid Films* 52 215-29

Alayo M I, Criado D, Goncalves L C D and Pereyra I 2004 Deposition and characterization of silicon oxynitride for integrated optical applications. *Journal of Non-Crystalline Solids* 338-40 76-80

Amantea R, Goodman L A, Pantuso F, Sauer D J, Varghese M, Villani T S and White L K 1998 Progress towards an uncooled IR imager with 5 mK NETD. *Proceedings of SPIE*. 3436 647-59

Amantea R, Knoedler C M, Pantuso F P, Patel V K, Sauer D J and Tower J R 1997 An uncooled IR imager with 5 mK NETD. *Proceedings of SPIE* 3061 210-22

Argon A S 1979 Plastic-Deformation in Metallic Glasses. *Acta Metallurgica* 27 47-58

Astie S, Gue A M, Scheid E and Guillemet J P 2000 Design of a low power SnO₂ gas sensor integrated on silicon oxynitride membrane. *Sensors and Actuators B-Chemical* 67 84-8

Bagolini A, Pakula L, Scholtes T L M, Pham H T M, French P J and Sarro P M 2002 Polyimide sacrificial layer and novel materials for post-processing surface micromachining. *Journal of Micromechanics and Microengineering* 12 385-9

Baselt D R, Fruhberger B, Klaassen E, Cemalovic S, Britton C L, Patel S V, Mlsna T E, McCorkle D and Warmack B 2003 Design and performance of a microcantilever-based hydrogen sensor. *Sensors and Actuators B-Chemical* 88 120-31

Bell P, Hoivik N, Bright V and Popovic Z 2003 A frequency tunable half-wave resonator using a MEMS variable capacitor (Reprinted from *Proc. 35th International Symposium on Microelectronics*, 2002). *Microelectronics International* 20 21-5

Bhattacharya A K and Nix W D 1988 Analysis of elastic and plastic-deformation associated with indentation testing of thin-films on substrates. *International Journal of Solids and Structures* 24 1287-98

Bifano T G, Johnson H T, Bierden P and Mali R K 2002 Elimination of stress-induced curvature in thin-film structures. *Journal of Microelectromechanical Systems* 11 592-7

Brown D M, Gray P V, Heumann F K, Philipp H R and Taft E A 1968 Properties of SiON Films on Si. *Journal of the Electrochemical Society* 115 311-7

Burns D M and Bright V M 1998 Development of microelectromechanical variable blaze gratings *Sensors and Actuators a-Physical* 64 7-15

Callister W D and Rethwisch D G 2010 *Materials Science and Engineering: An Introduction* (Hoboken, NJ: John Wiley & Sons)

Cao Z Q, Zhang T Y and Zhang X 2005 Microbridge testing of plasma-enhanced chemical-vapor deposited silicon oxide films on silicon wafers. *Journal of Applied Physics* 97 -

Cao Z Q and Zhang X 2006 Size-dependent creep behaviour of plasma-enhanced chemical vapour deposited silicon oxide films. *Journal of Physics D- Applied Physics* 39 5054-63

Cao Z Q and Zhang X 2007 Nanoindentation creep of plasma-enhanced chemical vapor deposited silicon oxide thin films. *Scripta Materialia* 56 249-52

Chang C L and Chang P Z 2000 Innovative micromachined microwave switch with very low insertion loss. *Sensors and Actuators a-Physical* 79 71-5

Chaudhari P 1972 Grain growth and stress relief in thin films. *Journal of Vacuum Science and Technology* 9 520-2

Chen K S, Chen T C and Ou K S 2008 Development of semi-empirical formulation for extracting materials properties from nanoindentation measurements: Residual stresses, substrate effect, and creep. *Thin Solid Films* 516 1931-40

Chen K S, Chen T Y F, Chuang C C and Lin I K 2004 Full-field wafer level thin film stress measurement by phase-stepping shadow Moire. *IEEE Transactions on Components and Packaging Technologies* 27 594-601

- Chen K S and Hsu R F 2007 Evaluation of environmental effects on mechanical properties and characterization of creep behavior of PMMA. *Journal of the Chinese Institute of Engineers* 30 267-74
- Chen K S, Zhang X and Lin S Y 2003 Intrinsic stress generation and relaxation of plasma-enhanced chemical vapor deposited oxide during deposition and subsequent thermal cycling. *Thin Solid Films* 434 190-202
- Chu W-H, Mehregany M and Mullen R L 1993 Analysis of tip deflection and force of a bimetallic cantilever microactuator. *Journal of Micromechanics and Microengineering* 3 4-7
- Dai C L, Yen K S and Chang P Z 2001 Applied electrostatic parallelogram actuators for microwave switches using the standard CMOS process. *Journal of Micromechanics and Microengineering* 11 697-702
- Datskos P G, Lavrik N V and Rajic S 2004 Performance of uncooled microcantilever thermal detectors. *Review of Scientific Instruments* 75 1134-48
- Datskos P G, Rajic S and Lavrik N V 2005 Performance of uncooled microcantilever thermal detectors. *MOEMS Display and Imaging Systems. III* 5721 136-50
- Degroot P and Deck L 1993 3-Dimensional imaging by sub-Nyquist sampling of white-light interferograms. *Optics Letters* 18 1462-4
- Denisse C M M, Troost K Z, Elferink J B O, Habraken F H P M, Vandeweg W F and Hendriks M 1986 Plasma-enhanced growth and composition of silicon oxynitride films. *Journal of Applied Physics* 60 2536-42
- Dereniak E L and Boreman G D 1996 *Infrared detectors and systems* (Hoboken, NJ: John Wiley & Sons, Inc.)
- Desbiens E, Dolbec R and El Khakani M A 2002 Reactive pulsed laser deposition of high-k silicon dioxide and silicon oxynitride thin films for gate-dielectric applications. *Journal of Vacuum Science & Technology A-Vacuum Surfaces and Films* 20 1157-61
- Doerner M F and Nix W D 1988 Stresses and deformation processes in thin-films on substrates. *CRC Critical Reviews in Solid State and Materials Sciences* 14 225-68

- Du H H, Tressler R E and Spear K E 1989 Thermodynamics of the Si-N-O system and kinetic modeling of oxidation of Si₃N₄. *Journal of the Electrochemical Society* 136 3210-5
- Dunn M L, Zhang Y H and Bright V M 2001 Deformation and stability of gold/polysilicon layered MEMS plate structures subjected to thermal loading. *Mechanical Properties of Structural Films* 1413 306-17
- Dunn M L, Zhang Y H and Bright V M 2002 Deformation and structural stability of layered plate microstructures subjected to thermal loading. *Journal of Microelectromechanical Systems* 11 372-84
- Eriksson T S and Granqvist C G 1986 Infrared optical-properties of silicon oxynitride films - experimental-data and theoretical interpretation. *Journal of Applied Physics* 60 2081-91
- Fadel M, Bulters M, Niemand M, Voges E and Krummrich P M 2009 Low-loss and low-birefringence high-contrast silicon-oxynitride waveguides for optical communication. *Journal of Lightwave Technology* 27 698-705
- Falk M L and Langer J S 1998 Dynamics of viscoplastic deformation in amorphous solids. *Physical Review E* 57 7192-205
- Finot M, Blech I A, Suresh S and Fujimoto H 1997 Large deformation and geometric instability of substrates with thin-film deposits. *Journal of Applied Physics* 81 3457-64
- Finot M and Suresh S 1996 Small and large deformation of thick and thin-film multi-layers: Effect of layer geometry, plasticity and compositional gradients. *Journal of the Mechanics and Physics of Solids* 44 683-721
- Freund L B 1993 The stress-distribution and curvature of a general compositionally graded semiconductor layer. *Journal of Crystal Growth* 132 341-4
- Freund L B 2000 Substrate curvature due to thin film mismatch strain in the nonlinear deformation range. *Journal of the Mechanics and Physics of Solids* 48 1159-74
- Freund L B, Floro J A and Chason E 1999 Extensions of the Stoney formula for substrate curvature to configurations with thin substrates or large deformations. *Applied Physics Letters* 74 1987-9

- Freund L B and Suresh S 2003 Thin Film Materials (Cambridge, UK: Cambridge University Press)
- Galeener F L 1979 Band limits and the vibrational-spectra of tetrahedral glasses. *Physical Review B* 19 4292-7
- Gall K, West N, Spark K, Dunn M L and Finch D S 2004 Creep of thin film Au on bimaterial Au/Si microcantilevers. *Acta Materialia* 52 2133-46
- Gao J, Zhang Q C, Jiao B B and Chen D P 2009 Optical sensitivity analysis of a bent micro reflector array in uncooled infrared imaging. *Journal of Micromechanics and Microengineering* 19 095018
- Gardner D S and Flinn P A 1990 Mechanical-stress as a function of temperature for aluminum-alloy films. *Journal of Applied Physics* 67 1831-44
- Go J S, Cho Y H, Kwak B M and Park K 1996 Snapping microswitches with adjustable acceleration threshold. *Sensors and Actuators A-Physical* 54 579-83
- Grbovic D, Lavrik N V, Datskos P G, Forrai D, Nelson E, Devitt J and McIntyre B 2006 Uncooled infrared imaging using bimaterial microcantilever arrays. *Applied Physics Letters* 89 073118
- Gritsenko V A, Xu J B, Kwok R W M, Ng Y H and Wilson I H 1998 Short range order and the nature of defects and traps in amorphous silicon oxynitride governed by the Mott rule. *Physical Review Letters* 81 1054-7
- Guimaraes M S, Sinatora A, Alayo M I, Pereyra I and Carreno M N P 2001 Mechanical and thermophysical properties of PECVD oxynitride films measured by MEMS. *Thin Solid Films* 398 626-31
- Gunning W J, Hall R L, Woodberry F J, Southwell W H and Gluck N S 1989 Codeposition of continuous composition rugate filters. *Applied Optics* 28 2945-8
- Habermehl S, Glenzinski A K, Halliburton W M and Sniegowski J J 2000 Properties of low residual stress silicon oxynitrides used as a sacrificial layer. *Materials Science of Microelectromechanical Systems (MEMS) Devices II* 605 49-54
- Harris K E and King A H 1995 A TEM investigation of the effects of tensile stress on thin film microstructure and surface morphology. *Thin Films: Stresses and Mechanical Properties V* 356 75-80

Hearne S, Chason E, Han J, Floro J A, Figiel J, Hunter J, Amano H and Tsong I S T 1999 Stress evolution during metalorganic chemical vapor deposition of GaN. *Applied Physics Letters* 74 356-8

Hibbit K S, Inc. 1998 ABAQUS User Manual: Hibbit, Karlsson & Sorensen, Inc.)

Hill R 1992 Similarity analysis of creep indentation tests. *Proceedings of the Royal Society of London Series A-Mathematical Physical and Engineering Sciences* 436 617-30

Hsueh C H 2002 Modeling of elastic deformation of multilayers due to residual stresses and external bending. *Journal of Applied Physics* 91 9652-6

Huang S 2007 Development of double-cantilever infrared detectors. (Boston: Boston University)

Huang S, Tao H, Lin I K and Zhang X 2008 Development of double-cantilever infrared detectors: Fabrication, curvature control and demonstration of thermal detection. *Sensors and Actuators A-Physical* 145 231-40

Huang S S, Li B and Zhang X 2006 Elimination of stress-induced curvature in microcantilever infrared focal plane arrays. *Sensors and Actuators A-Physical* 130 331-9

Huang S S and Zhang X 2006 Extension of the Stoney formula for film-substrate systems with gradient stress for MEMS applications. *Journal of Micromechanics and Microengineering* 16 382-9

Hunter S R, Maurer G, Jiang L and Simelgor G 2006 High-sensitivity uncooled microcantilever infrared imaging arrays. *Proceedings of SPIE* 6206 62061J

Hwang S J, Lee Y D, Park Y B, Lee J H, Jeong C O and Joo Y C 2006 In situ study of stress relaxation mechanisms of pure Al thin films during isothermal annealing. *Scripta Materialia* 54 1841-6

Janda M and Stefan O 1984 Intrinsic Stress in chromium thin-films measured by a novel method. *Thin Solid Films* 112 127-37

Jozwik M, Delobelle P, Gorecki C, Sabac A, Nieradko L, Meunier C and Munnik F 2004 Optomechanical characterisation of compressively prestressed silicon oxynitride films deposited by plasma-enhanced chemical vapour deposition on silicon membranes. *Thin Solid Films* 468 84-92

- Jung S, Hwang S and Yi J 2008 Memory properties of oxide-nitride-oxynitride stack structure using ultra-thin oxynitrided film as tunneling layer for nonvolatile memory device on glass. *Thin Solid Films* 517 362-4
- Keller R M, Baker S P and Arzt E 1999 Stress-temperature behavior of unpassivated thin copper films. *Acta Materialia* 47 415-26
- Klein C A 2000 How accurate are Stoney's equation and recent modifications. *Journal of Applied Physics* 88 5487-9
- Kroll P 2005 A DFT study of amorphous silicon oxynitride. *Journal of Non-Crystalline Solids* 351 1127-32
- Kruse P W and Skatrud D D 1997 *Uncooled infrared imaging arrays and systems* (San Diego, CA: Academic Press)
- Langer J S 2001 Microstructural shear localization in plastic deformation of amorphous solids *Physical Review E* 6401 -
- Lee H J, Cornella G and Bravman J C 2000 Stress relaxation of free-standing aluminum beams for microelectromechanical systems applications. *Applied Physics Letters* 76 3415-7
- Lee S, Wallis T M, Moreland J, Kabos P and Lee Y C 2007 Asymmetric dielectric trilayer cantilever probe for calorimetric high-frequency field imaging. *Journal of Microelectromechanical Systems* 16 78-86
- Leskela M and Ritala M 2001 Atomic layer deposition (ALD): from precursors to thin film structures. In: *2nd Asian Conference on Chemical Vapor Deposition (CVD)*, (Gyeongju, South Korea: Elsevier Science Sa) pp 138-46
- Li B 2004 Design and simulation of an uncooled double-cantilever microbolometer with the potential for similar to mK NETD. *Sensors and Actuators A-Physical* 112 351-9
- Li C B, Jiao B B, Shi S L, Chen D P, Ye T C, Zhang Q C, Guo Z Y, Dong F L and Miao Z Y 2006 A novel uncooled substrate-free optical-readable infrared detector: design, fabrication and performance. *Measurement Science & Technology* 17 1981-6
- Li H and Ngan A H W 2004 Size effects of nanoindentation creep. *Journal of Materials Research* 19 513-22

- Lin I-K, Wu P-H, Ou K-S, Chen K-S and Zhang X 2010a The Tunability in Mechanical Properties and Fracture Toughness of Sputtered Silicon Oxynitride Thin Films for MEMS-Based Infrared Detectors. (Boston: Materials Research Society Symposium Proceedings) pp 1222-DD02-20
- Lin I-K, Zhang X and Zhang Y 2010b Suppression of Inelastic Deformation in Multilayer Microcantilevers with Nanoscale Coating. (Boston: Materials Research Society Symposium Proceedings) pp 1222-DD02-19
- Lin I K, Zhang X and Zhang Y H 2009 Thermomechanical behavior and microstructural evolution of SiN_x/Al bimaterial microcantilevers. *Journal of Micromechanics and Microengineering* 19 085010
- Lin I K, Zhang Y H and Zhang X 2008b The deformation of microcantilever-based infrared detectors during thermal cycling. *Journal of Micromechanics and Microengineering* 18 075012
- Lu J 1996 Handbook of Measurement of Residual Stresses (Lilburn, GA: Fairmount Press)
- Lucas B N and Oliver W C 1999 Indentation power-law creep of high-purity indium. *Metallurgical and Materials Transactions A-Physical Metallurgy and Materials Science* 30 601-10
- Lucovsky G, Richard P D, Tsu D V, Lin S Y and Markunas R J 1986 Deposition of silicon dioxide and silicon-nitride by remote plasma enhanced chemical vapor-deposition. *Journal of Vacuum Science & Technology a-Vacuum Surfaces and Films* 4 681-8
- Madou M 1997 Fundamentals of Microfabrication (New York: CRC Press LLC)
- Miller D C, Dunn M L and Bright V M 2001a Thermally induced change in deformation of multimorph MEMS structures. *Proceedings of SPIE* 4558 32-44
- Miller D C, Herrmann C F, Maier H J, George S M, Stoldt C R and Gall K 2005 Intrinsic stress development and microstructure evolution of Au/Cr/Si multilayer thin films subject to annealing. *Scripta Materialia* 52 873-9
- Miller D C, Herrmann C F, Maier H J, George S M, Stoldt C R and Gall K 2007a Thermo-mechanical evolution of multilayer thin films: Part I. Mechanical behavior of Au/Cr/Si microcantilevers. *Thin Solid Films* 515 3208-23

Miller D C, Herrmann C F, Maier H J, George S M, Stoldt C R and Gall K 2007b Thermo-mechanical evolution of multilayer thin films: Part II. Microstructure evolution in Au/Cr/Si micro cantilever.s Thin Solid Films 515 3224-40

Miller D C, Zhang W G and Bright V M 2001b Micromachined, flip-chip assembled, actuatable contacts for use in high density interconnection in electronics packaging. Sensors and Actuators A-Physical 89 76-87

Modreanu M, Gartner M and Cristea D 2002 Investigation on preparation and physical properties of LPCVD SiXOyNZ thin films and nanocrystalline Si/SixOYNZ superlattices for Si-based light emitting devices. Materials Science & Engineering C-Biomimetic and Supramolecular Systems 19 225-8

Modreanu M, Tomozeiu N, Cosmin P and Gartner M 1999 Optical properties of LPCVD silicon oxynitride. Thin Solid Films 337 82-4

Mullins W W 1958 The effect of thermal grooving on grain boundary motion. Acta Metallurgica 6 414-27

Nix W D 1989 Mechanical-properties of thin-films. Metallurgical Transactions A-Physical Metallurgy and Materials Science 20 2217-45

Ohring M 2002 Materials science of thin films (San Diego, CA: Academia Press)

Oliver W C and Pharr G M 1992 An improved technique for determining hardness and elastic-modulus using load and displacement sensing indentation experiments. Journal of Materials Research 7 1564-83

Oliver W C and Pharr G M 2004 Measurement of hardness and elastic modulus by instrumented indentation: Advances in understanding and refinements to methodology. Journal of Materials Research 19 3-20

Onishi T, Iwamura E and Takagi K 1999 Morphology of sputter deposited Al alloy films. Thin Solid Films 340 306-16

Ott A W, Klaus J W, Johnson J M and George S M 1997 Al₂O₃ thin film growth on Si(100) using binary reaction sequence chemistry. Thin Solid Films 292 135-44

Philipp H R 1972 Optical and bonding model for non-crystalline SiO_x and SiO_xN_y materials. Journal of Non-Crystalline Solids 8-10 627-32

Poirier J P 1985 Creep of Crystals -High Temperature Deformation Processes in Metals, Ceramics and Minerals (Cambridge, U.K.: Cambridge University Press)

Poisl W H, Oliver W C and Fabes B D 1995 The relationship between indentation and uniaxial creep in amorphous selenium. *Journal of Materials Research* 10 2024-32

Raiteri R, Grattarola M, Butt H J and Skladal P 2001 Micromechanical cantilever-based biosensors. *Sensors and Actuators B-Chemical* 79 115-26

Rand M J and Roberts J F 1973 Silicon oxynitride films from $\text{No-Nh}_3\text{-SiH}_4$ reaction. *Journal of the Electrochemical Society* 120 446-53

Riethmuller W and Benecke W 1988 Thermally excited silicon microactuators. *IEEE Transactions on Electron Devices* 35 758-63

Rogalski A 2003 Infrared detectors: status and trends. *Progress in Quantum Electronics* 27 59-210

Sassella A 1993 Tetrahedron model for the optical dielectric function of H-rich silicon oxynitride. *Physical Review B* 48 14208-15

Schuh C A and Nieh T G 2003 A nanoindentation study of serrated flow in bulk metallic glasses. *Acta Materialia* 51 87-99

Schuh C A and Nieh T G 2004 A survey of instrumented indentation studies on metallic glasses. *Journal of Materials Research* 19 46-57

Schwaiger R, Moser B, Dao M, Chollacoop N and Suresh S 2003 Some critical experiments on the strain-rate sensitivity of nanocrystalline nickel. *Acta Materialia* 51 5159-72

Sehr H, Evans A G R, Brunnschweiler A, Ensell G J and Niblock T E G 2001 Fabrication and test of thermal vertical bimorph actuators for movement in the wafer plane. *Journal of Micromechanics and Microengineering* 11 306-10

Sen P N and Thorpe M F 1977 Phonons in Ax_2 glasses - from molecular to band-like modes. *Physical Review B* 15 4030-8

Senesac L R, Corbeil J L, Rajic S, Lavrik N V and Datskos P G 2003 IR imaging using uncooled microcantilever detectors. *Ultramicroscopy* 97 451-8

Serenyi M, Racz M and Lohner T 2001 Refractive index of sputtered silicon oxynitride layers for antireflection coating. *Vacuum* 61 245-9

Shackelford J F and Alexander W 2001 *CRC materials science and engineering handbook* (Sound Parkway, NW: CRC Press)

- Shen Y L and Ramamurty U 2003 Constitutive response of passivated copper films to thermal cycling. *Journal of Applied Physics* 93 1806-12
- Shen Y L and Suresh S 1995 Thermal cycling and stress-relaxation response of Si-Al and Si-Al-SiO₂ layered thin-films. *Acta Metallurgica et Materialia* 43 3915-26
- Spaepen F 1977 Microscopic mechanism for steady-state inhomogeneous flow in metallic glasses. *Acta Metallurgica* 25 407-15
- Storakers B and Larsson P L 1994 An analysis of fully plastic Brinell indentation. *Journal of the Mechanics and Physics of Solids* 42 307-32
- Tao H, Strikwerda A C, Fan K, Padilla W J, Zhang X and Averitt R D 2009 Reconfigurable terahertz metamaterials. *Physical Review Letters* 103 -
- Thouless M D 1993 Effect of surface-diffusion on the creep of thin-films and sintered arrays of particles. *Acta Metallurgica et Materialia* 41 1057-64
- Thurn J, Cook R F, Kamarajugadda M, Bozeman S P and Stearns L C 2004 Stress hysteresis and mechanical properties of plasma-enhanced chemical vapor deposited dielectric films. *Journal of Applied Physics* 95 967-76
- Timoshenko S 1925 Analysis of bimetal thermostats. *Journal of the Optical Society of America* 11 233
- Tripp M K, Stampfer C, Miller D C, Helbling T, Hermann C F, Hierold C, Gall K, George S M and Bright V M 2006 The mechanical properties of atomic layer deposited alumina for use in micro- and nano-electromechanical systems. *Sensors and Actuators A-Physical* 130 419-29
- Tsu D V, Lucovsky G and Mantini M J 1986 Local atomic-structure in thin-films of silicon-nitride and silicon diimide produced by remote plasma-enhanced chemical-vapor deposition. *Physical Review B* 33 7069-76
- Tymiak N I, Kramer D E, Bahr D F, Wyrobek T J and Gerberich W W 2001 Plastic strain and strain gradients at very small indentation depths. *Acta Materialia* 49 1021-34
- Venkatraman R and Bravman J C 1992 Separation of film thickness and grain-boundary strengthening effects in Al thin-films on Si. *Journal of Materials Research* 7 2040-8

- Vickers-Kirby D J, Kubena R L, Stratton F P, Joyce R J, Chang D T and Kim J 2000 Anelastic creep phenomena in thin metal plated cantilevers for MEMS. In: Materials Research Society Symposium, (Boston, MA pp EE2.5.1-EE2.5.6
- Vila M, Caceres D and Prieto C 2003 Mechanical properties of sputtered silicon nitride thin films. Journal of Applied Physics 94 7868-73
- Vinci R P and Vlassak J J 1996 Mechanical behavior of thin films. Annual Review of Materials Science 26 431-62
- Wang X, Ma S L, Yu X M, Liu M, Liu X H and Zhao Y J 2007 IR imaging using a cantilever-based focal plane array fabricated by deep reactive ion etching technique. Applied Physics Letters 91 054109
- Williams K R, Gupta K and Wasilik M 2003 Etch rates for micromachining processing - Part II. Journal of Microelectromechanical Systems 12 761-78
- Williams K R and Muller R S 1996 Etch rates for micromachining processing Journal of Microelectromechanical Systems 5 256-69
- Yan H Y, Ou K S and Chen K S 2008 Mechanical properties measurement of PECVD silicon nitride after rapid thermal annealing using nanoindentation technique. Strain 44 259-66
- Zhang Y H and Dunn M L 2003 Deformation of blanketed and patterned bilayer thin-film microstructures during post-release and cyclic thermal loading. Journal of Microelectromechanical Systems 12 788-96
- Zhang Y H and Dunn M L 2004 Geometric and material nonlinearity during the deformation of micron-scale thin-film bilayers subject to thermal loading. Journal of the Mechanics and Physics of Solids 52 2101-26
- Zhang Y H and Dunn M L 2009 Patterned bilayer plate microstructures subjected to thermal loading: Deformation and stresses. International Journal of Solids and Structures 46 125-34
- Zhang Y H, Dunn M L, Gall K, Elam J W and George S M 2004 Suppression of inelastic deformation of nanocoated thin film microstructures. Journal of Applied Physics 95 8216-25
- Zhao Y, Mao M Y, Horowitz R, Majumdar A, Varesi J, Norton P and Kitching J 2002 Optomechanical uncooled infrared imaging system: Design, microfabrication, and performance. Journal of Microelectromechanical Systems 11 136-46

VITA

I-Kuan Lin

110 Cummington St. Boston, MA 02215

Email: ikuan@bu.edu

Author's Background:

I-Kuan "Ken" Lin is currently a Ph.D. candidate in the Department of Mechanical Engineering, Boston University (Boston, Massachusetts). His research advisor is Professor Xin Zhang. I-Kuan Lin received the B.S. degree in mechanical and electrical engineering (double major) from Da-Yeh University, Changhua, Taiwan, in 2002 and the M.S. degree in mechanical engineering from National Cheng Kung University (NCKU), Tainan, Taiwan, in 2004. He is currently working toward the Ph.D. degree in the Department of Mechanical Engineering, Boston University, Boston, MA, USA. He was a Research Assistant with the System Dynamics Laboratory for Mechatronics and Microsystems, Department of Mechanical Engineering, NCKU, and the Advanced Lithography Division, National Nano Device Laboratory, during his master's study. From 2004 to 2006, he was a Research Assistant with the Institute of Physics, Academia Sinica, Taipei, Taiwan, where he worked on fabrication of 25-nm X-ray phase zone plates using e-beam lithography and electroplating. His Ph.D. research includes mechanical analysis and material characterization of polymer MEMS and amorphous thin film, and thermomechanical behavior of multilayer microcantilever structures with nanocoating.

Research Experience during PhD Study:

(1) Mechanical Behavior of Amorphous Plasma-Enhanced Chemical Vapor Deposited Silicon Oxide Films for MEMS Applications.

(National Science Foundation)

— Mechanical responses of the amorphous thin films will be probed under different thermal conditions, stress levels, and in both elastic and plastic regions.

(2) Uncooled Cantilever Microbolometer Focal Plane Arrays with mK Temperature Resolution: Engineering Mechanics for the Next Generation.

(Air Force Office of Scientific Research)

— To contribute to the scientific understanding of micro- and nano- mechanics of thin films so as to develop a new, revolutionary approach to the design and fabrication of robust, MEMS-based, cantilever infrared detectors.

(3) Micro- and Nano- Mechanics of Thin Film and Thin Film Coatings.

(Defense Advanced Research Projects Agency)

— To understand the inelastic deformation mechanics in thin film and nano coatings, relate these behaviors to the design and analysis, and apply these principles to improve the performance of devices in sub-micron scale.

(4) Elastic and Viscoelastic Characterization and Modeling of Polymer based Structures for Biological Applications.

(National Science Foundation)

— A more in-depth method for viscoelastic characterization, modeling, and analysis that are associated with the bending behavior of the polymer-based transducer.

Publications during PhD Study:

Archival Journal Articles

- (11) P-H Wu, **I-K Lin**, H-Y Yan, K-S Ou, K-S Chen, and X Zhang, "Mechanical Properties Characterization of Nitride Films Prepared via Sputtering and Plasma Enhanced Chemical Deposition (PECVD) Methods: Comparisons and Applications", *preparation, Journal of Micromechanics and Microengineering.*
- (10) **I-K Lin**, P-H Wu, K-S Ou, Y. Zhang, K-S Chen, and X. Zhang, "Measurement of Fracture Mechanical Properties of Silicon Oxynitride Films after Rapid Thermal Annealing", *preparation, Thin Solid Films.*
- (9) P. Du, **I-K Lin**, H. Lu, and X. Zhang, "Extension of the Beam Theory for the Polymer Bio-transducers with Low Aspect Ratios and Viscoelastic Characteristics", *under review, Journal of Micromechanics and Microengineering.*

- (8) **I-K Lin**, X. Zhang, and Y. Zhang, "Inelastic Deformation of Microcantilevers with Nanoscale Coating", *under review, Journal of Microelectromechanical Systems*.
- (7) B.J. Hansen, N. Kouklin, G. Lu, **I-K Lin**, J. Chen, and X. Zhang, "Transport, Analyte Detection and Opto-Electronic Response of p-Type CuO Nanowires", *Journal of Physical Chemistry C*, 114 (6) (2010) 2440-2447.
- (6) **I-K Lin**, K-S Ou, Y-M Liao, Y. Liu, K-S Chen, and X. Zhang, "Viscoelastic Characterization and Modeling of Polymer Transducers for Biological Applications", *Journal of Microelectromechanical Systems*, 18 (5) (2009) 1087-1099.
- (5) **I-K Lin**, X. Zhang, and Y. Zhang, "Thermomechanical Behavior and Microstructural Evolution of SiN_x/Al Bimaterial Microcantilevers", *Journal of Micromechanics and Microengineering*, 19 (8) (2009) 085010.
- (4) **I-K Lin**, Y-M Liao, Y. Liu, K-S Ou, K-S Chen, and X. Zhang, "Viscoelastic Mechanical Behavior of Soft Microcantilever-Based Force Sensors", *Applied Physics Letters*, 93 (25) (2008) 251907.

Selected for Virtual Journal of Nanoscale Science & Technology in Vol. 19, Issue 2, January 2009. (<http://www.vjnano.org>)

- (3) **I-K Lin**, Y. Zhang, and X. Zhang, "The Deformation of Microcantilever-Based Infrared Detectors during Thermal Cycling", *Journal of Micromechanics and Microengineering*, 18 (7) (2008) 075012.
- (2) Y. Liu, **I-K Lin**, and X. Zhang, "Mechanical Properties of Sputtered Silicon Oxynitride Films by Nanoindentation", *Materials Science and Engineering A*, 489 (1-2) (2008) 294-301.
- (1) S. Huang, H. Tao, **I-K Lin**, and X. Zhang, "Development of Double-Cantilever Infrared Detectors: Fabrication, Curvature Control and Demonstration of Thermal Detection", *Sensors and Actuators A: Physical*, 145-146 (2008) 231-240.

Conference Proceedings (Full Papers)

- (8) **I-K Lin**, P-H Wu, K-S Ou, K-S Chen, and X. Zhang, "The Tunability in Mechanical Properties and Fracture Toughness of Sputtered Silicon Oxynitride Thin Films for MEMS-Based Infrared Detectors", *Microelectromechanical Systems-Materials and Devices III, Materials Research Society Symposium Proceedings*, Boston, MA, USA, Nov. 30 – Dec. 3, 2009, 1222-DD02-20.

- (7) **I-K Lin**, X. Zhang, and Y. Zhang, "Suppression of Inelastic Deformation in Multilayer Microcantilevers with Nanoscale Coating", *Microelectromechanical Systems-Materials and Devices III, Materials Research Society Symposium Proceedings*, Nov. 30 – Dec. 3, 2009, 1222-DD02-19.
- (6) K-S Ou, **I-K Lin**, P-H Wu, and X. Zhang, and K-S Chen, "Mechanical Characterization of Atomic Layer Deposited (ALD) Alumina for Applications in Corrosive Environments", *Microelectromechanical Systems-Materials and Devices III, Materials Research Society Symposium Proceedings*, Nov. 30 – Dec. 3, 2009, 1222-DD02-14.
- (5) **I-K Lin**, K-S Ou, K-S Chen, and X. Zhang, "Cellular Force Measurement in Cardiac Myocytes Using Polymer Micropillar Array with Viscoelastic Characterization", *Proceeding of the 13th International Conference on Miniaturized Systems for Chemistry and Life Sciences (microTAS '09)*, Jeju, Korea, Nov. 1-5, 2009 pp.269-271.
- (4) **I-K Lin**, Y-M Liao, K-S Chen, and X. Zhang, "Viscoelastic Characterization of Soft Micropillars for Cellular Mechanics Study", *Proceeding of the 12th International Conference on Miniaturized Systems for Chemistry and Life Sciences (microTAS '08)*, San Diego, CA, USA, Oct. 12-16, 2008, pp.278-280.
- (3) **I-K Lin**, Y-M Liao, Y. Liu, K-S Chen, X. Zhang, "Elastic and Viscoelastic Characterization of Polydimethylsiloxane (PDMS) for Cell-Mechanics Applications", *Microelectromechanical Systems-Materials and Devices, Materials Research Society Symposium Proceedings*, Nov. 26 – Dec. 28, 2007, 1052-DD03-02.
- (2) Y. Liu, **I-K Lin**, X. Zhang, "Mechanical Properties of Sputtered Silicon Oxynitride Films by Nanoindentation", *Fundamentals of Nanoindentation and Nanotribology IV, Materials Research Society Symposium Proceedings*, Nov. 26 – Dec. 28, 2007, 1049-AA05-17.
- (1) S. Huang, **I-K Lin**, H. Tao, and X. Zhang, "Double-Cantilever Micro Infrared Detector: Fabrication, Post-Process Curvature Modification and Thermal Response Characterization," *Proceeding of the 14th International Conference on Solid-State Sensors, Actuators and Microsystems (Transducers '07)*, Lyon, France, June10-14, 2007, pp.1601-1604.

Conference (Abstract Referred)

- (11) **I-K Lin**, Y. Zhang, and X. Zhang, "Suppression and Modeling of Inelastic Deformation in Multilayer Microcantilevers with Nanoscale Coating," to be presented at *the 16th US National Congress of Theoretical and Applied Mechanics*, State College, PA, USA, June 27 - July 2, 2010.
- (10) P. Du, **I-K Lin**, H. Lu, and X. Zhang, "Extension of the Beam Theory for the Polymer Bio-Transducers with Low Aspect Ratios and Viscoelastic Characteristics", to be presented at *the 16th US National Congress of Theoretical and Applied Mechanics*, State College, PA, USA, June 27 - July 2, 2010.
- (9) A.F. Bayomy, M. Bauer, **I-K Lin**, X Zhang, R Liao, " The effect of Matrix Stiffness on Cardiac Side Population Cell Behavior," to be presented at *Northwest Biomechanics Symposium*, Seattle, WA, USA, May 21 - May 22, 2010.
- (8) B.J. Hansen, G. Lu, *I-K Lin*, N. Kouklin, J. Chen, and X. Zhang, "The Growth and Characterization of Copper (II) Oxide Nanowires with Single Nanowire Electrical, Gas Sensing, and Photoconduction Measurements" , Presented at *the 3rd International Conference on One-Dimensional Nanomaterials*, Atlanta, GA, USA, December 7-9, 2009.
- (7) B.J. Hansen, G. Lu, **I-K Lin**, N. Kouklin, J. Chen, and X. Zhang, "The Growth and Characterization of Copper (II) Oxide Nanowires with Single Nanowire Electrical, Gas Sensing, and Photoconduction Measurements", Presented at *the Materials Research Society Fall Meeting*, Boston, MA, USA, Nov. 30 – Dec. 3, 2009.
- (6) X. Wang, S. Yerci, **I-K Lin**, L. Dal Negro, and X. Zhang, "Mechanical and Optical Properties of Reactively Sputtered Silicon-rich Silicon Nitride Films", Presented at *the Materials Research Society Fall Meeting*, Boston, MA, USA, November 30 - December 3, 2009.
- (5) **I-K Lin**, Y-M Liao, Y. Liu, K-S Ou, K-S Chen, and X. Zhang, "Elastic and Viscoelastic Characterization and Modeling of Polymer Based Structures for Biological Applications", Presented at *the ASME International Mechanical Engineering Congress and Exposition*, Boston, MA, October 31 - November 6, 2008.
- (4) **I-K Lin**, K. Fan, S. Huang, A. Gonzalez, Y. Zhang, and X. Zhang, "Characterization of Gradient Residual Stress Evolution in Bimaterial Microcantilever Structures during

- Thermal Cycling”, Presented at *the ASME International Mechanical Engineering Congress and Exposition*, Boston, MA, October 31 - November 6, 2008.
- (3) **I-K Lin**, H. Lu, and X. Zhang, “Elastic and Viscoelastic Characterization and Modeling of Polymer Based Structures for Biological Applications”, Presented at *the Gordon Research Conference for Thin Film & Small Scale Mechanical Behavior*, Waterville, ME, July 27- August 1, 2008.
 - (2) **I-K Lin** and X. Zhang, “Viscoelastic Characterization of Soft Micropillars as Force Sensor for Biological Applications”, Presented at *the IEEE Solid-State Sensor and Actuator Workshop, Hilton Head Island, SC, USA*, June 1-5, 2008.
 - (1) **I-K Lin**, Y. Zhang, and X. Zhang, “Curvature Control of Microcantilever Based Infrared Detectors Using Thermal Loading Method”, Presented at *the Materials Research Society Fall Meeting*, Boston, MA, USA, November 26-30, 2007.

Publications before PhD Study:

Journal Articles

- (5) T-N Lo, Y-T Chen, C-W Chiu, C-J Liu, H-J Wu, **I-K Lin**, W-D Chang, Y. Hwu, C-C Chiang, J. H. Je, and G. Margaritondo, “E-beam lithography and electrodeposition fabrication of thick nanostructured devices”, *Journal of Physics D: Applied Physics*, 40 (2007) 3172-3176.
- (4) H-M Yeh, K-S Chen, and **I-K Lin**, “Development of 3D Electron Beam Lithography Fabrication Simulator”, *Tamkang Journal of Science and Engineering*, 10 (2007) 167-172.
- (3) K-S Chen, **I-K Lin**, and F-H Ko, “Fabrication of 3D polymer microstructures using electron beam lithography and nanoimprinting technologies”, *Journal of Micromechanics and Microengineering*, 15 (2005) 1894-1903.
- (2) J-K Chen, **I-K Lin**, F-H Ko, C-F Huang, K-S Chen and F-C Chang, “Behavior and Surface Energies of Polybenzoxazines formed by Polymerization with Argon, Oxygen, and Hydrogen Plasmas”, *Journal of Polymer Science Part B: Polymer Physics*, 42 (2004) 4063-4074.

- (1) K-S Chen, T. Y. Chen, J-C Chuang, and **I-K Lin**, "Full-Field Wafer Level Thin Film Stress Measurement by Phase-Stepping Shadow Moiré", *IEEE Transactions on Components and Packaging Technologies*, 27 (2004) 594-601.

Conference Proceedings (Full Papers)

- (12) Y. T. Chen, **I. K. Lin**, T. N. Lo, C. I. Su, C. J. Liu, J. H. Je, G. Margaritondo, and Y. Hwu, "Study of LOR5B resist for the Fabrication of Hard X-ray Zone Plates by E-beam Lithography and ICP", *American Institute of Physics Conference Proceedings*, Daegu, South Korea, May 28 - June 02, 2007, pp.1516-1519.
- (11) T. N. Lo, Y. T. Chen, C. J. Liu, W. D. Chang, T. Y. Lai, H. J. Wu, **I. K. Lin**, C. I. Su, B. Y. Shew, J. H. Je, G. Margaritondo, and Y. Hwu, "Using E-Beam and X-Ray Lithography Techniques to Fabricate Zone Plates for Hard X-ray", *American Institute of Physics Conference Proceedings*, Daegu, South Korea, May 28 - June 02, 2007, pp.1466-1469.
- (10) H-M Yeh, K-S Chen, and **I-K Lin**, "Development of Electron Beam Lithography 3D Fabrication Emulator: A Current Status Report", *Symposium on Nano Device Technology*, Hsinchu, Taiwan, Apr. 28, 2006.
- (9) **I-K Lin**, K-S Chen and F-H Ko, "Surface Tension Powered Self-Assembly of Three-Dimensional Microstructures", *The 21st National Conference on Mechanical Engineering, The Chinese Society of Mechanical Engineers*, Kaohsiung, Taiwan, Sep. 26-27, 2004.
- (8) **I-K Lin**, K-S Chen, and F-H Ko, "Modeling for SU-8 Structures Fabricated by Electron Beam Lithography", *Symposium on Nano Device Technology*, Hsinchu, Taiwan, May 11, 2004.
- (7) **I-K Lin**, K-S Chen and F-H Ko, "Development of 3-D Micro Structures Processing Technologies by Using Electron Beam Lithography and Nanoimprinting Lithography," *The 8th Annular Meeting on Micro/Nano Technology*, Hsinchu, Taiwan, 2004.
- (6) **I-K Lin**, C-C Chung, K-S Chen, T-Y Chen, and F-H Ko, "Use of Phase-Shifting Shadow Moire Method to Measurement the Wafer Warpages", *The 27th Conference on Theoretical and Applied Mechanics*, Tainan, Taiwan, Dec. 12-13, 2003.

- (5) R-F Shu, K-S Chen, and **I-K Lin** "Experimental Studies on Mechanical and Creeping Properties of PMMA", *The 27th Conference on Theoretical and Applied Mechanics*, Tainan, Taiwan, Dec. 12-13, 2003.
- (4) **I-K Lin**, C-C Chung, K-S Chen, T.Y. Chen, and F-H Ko, "Development of a Wafer Warpages and Film Stress Characterization System using Phase-Shifting Shadow Moire Technology", *The 20th National Conference on Mechanical Engineering, The Chinese Society of Mechanical Engineers*, Taipei, Taiwan, Dec. 5-6, 2003.
- (3) K-S Chen, H-M Yeh, **I-K Lin**, and K-B Huang, "Development of a Solid Modeling MEMS Fabrication Emulator for SMart Process," *The 7th Annular Meeting on Micro/Nano Technology*, Taipei, Taiwan, 2003.
- (2) J-K Chen, **I-K Lin**, F-H Ko, and F-C Chang, "Plasma resistance and behavior of polybenzoxazine polymer", *International Microprocesses and Nanotechnology Conference*, Tokyo, Japan, Oct. 29-31, 2003, pp.260-261.
- (1) C-C Ho, K-S Chen and **I-K Lin**, "Electromagnets Calibration Using Pull-In Instability", *The 19th National Conference on Mechanical Engineering, The Chinese Society of Mechanical Engineers*, Taipei, Taiwan, Dec. 6-7, 2002.

Conference (Abstract Referred)

- (2) **I. K. Lin** , T. Y. Yang, C. H. Wang, Y. Hwu, C. D. Chen, Y. T. Chen, C. I. Su, "Evaluation of KMPR Etching Processes for Fabrication of High Resolution Hard X-Ray Zone Plates", Presented at the 9th International Conference on Synchrotron Radiation Instrumentation, Deagu, Korea, May 28 - June 2, 2006.
- (1) K-S Chen, T. Y. Chen, J-C Chuang, and **I-K Lin**, "Full- Field Wafer Level Thin Film Stress Measurement By Phase-Stepping Shadow Morie", Presented at *the 12th International Conference on Experimental Mechanics*, Politecnico di Bari, Italy, Aug. 29 - Sep. 2, 2004.

Awards:

2008 **Best Poster Award**, The 3rd Micro and Nanotechnology Society-wide Forum, ASME International Mechanical Engineering Congress and Exposition, Nov. 5, 2008, Boston, MA, USA.

URL: <http://www.bu.edu/phpbin/news-cms/news/?dept=666&id=51453>

URL:

http://www.asme.org/NewsPublicPolicy/PressReleases/Presents_Five_Awards_Micro.cfm

2006-2007 **Dean's Fellowship**, College of Engineering, Boston University.

Professional Affiliations:

IEEE

American Society of Mechanical Engineers (ASME)

Materials Research Society (MRS)